Theoretical Design of Molecular Nanostructures for Exciton Control

by

Maria A. Castellanos

B.S. Chemistry
Universidad Icesi, 2017

Submitted to the Department of Chemistry
in Partial Fulfillment of the Requirements for the Degree of

DOCTOR OF PHILOSOPHY IN CHEMISTRY

at the

MASSACHUSETTS INSTITUTE OF TECHNOLOGY

February 2024

Authored by: Maria A. Castellanos
Department of Chemistry
November 21, 2023

Certified by: Adam P. Willard
Professor of Chemistry
Thesis Supervisor

Accepted by: Adam P. Willard
Department of Chemistry Graduate Officer
Professor of Chemistry

This doctoral thesis has been examined by a committee of the Department of Chemistry as follows:

Professor Jianshu Cao: ....
Thesis Committee Chair
Professor of Chemistry

Professor Adam P. Willard: ....
Thesis Supervisor
Professor of Chemistry

Professor Keith A. Nelson: ....
Thesis Committee Member
Haslam and Dewey Professor of Chemistry

Theoretical Design of Molecular Nanostructures for Exciton Control

by

Maria A. Castellanos

Submitted to the Department of Chemistry
on November 21, 2023, in Partial Fulfillment of the
Requirements for the Degree of
DOCTOR OF PHILOSOPHY IN CHEMISTRY

ABSTRACT

Organic semiconductors comprised of strongly-coupled chromophores harness control of delocalized excitations, or excitons, via programmed molecular structures. The dynamics of these excitons enable energy and information transfer within molecular networks, positioning chromophore assemblies as ideal candidates for a number of technologies such as solar energy conversion, nanoelectronics, and quantum computing. Despite significant advancements, there exists no universal model that can explain the dependence of exciton photophysics on molecular morphology. This thesis employs mathematical and atomistic models to contribute key physical insights into the interdependencies between chromophore spatial organization and exciton dynamics, shaped by inter-chromophore couplings and interactions with the thermal bath.

In the first part, a Frenkel Exciton-based model is introduced as a strategy for studying exciton evolution between precisely arranged chromophores. In Chapter 2, I develop a novel approach to map unitary quantum computing operations to Hamiltonians describing excitonic circuits in the presence of a model bath. Then, Chapter 3 scales this framework to complex quantum algorithms represented by explicit molecular systems. Finally, Chapter 4 presents an innovative molecular approach for directing exciton flow via geometrical phase in tightly-bound chromophore arrays.

The second part delves into the intricacies of exciton interaction in densely packed molecular systems arranged within DNA scaffolds. Chapter 5 combines molecular dynamics and quantum mechanical calculations, further validated by experimental results, to study the interplay between long-range electrostatic and short-range charge transfer interactions. Chapter 6 then correlates this interplay with geometrical configurations derived from the DNA scaffolding. This thesis culminates in Chapter 7, which introduces a computational pipeline designed to leverage the precise control over excitons afforded by macromolecular frameworks, paving the way for custom-tailored DNA-based excitonic circuits.

Thesis Supervisor: Adam P. Willard
Title: Professor of Chemistry

Acknowledgments

I would like to acknowledge all the sources that have provided funding for the work I present here. The US Department of Energy (DOE), under award number DE-SC0019998, the Amy Lin Shen Summer Fellowship and the Molecular Sciences Software Institute (MolSSI) Software Fellowship. I also want to acknowledge the computational resources of the National Energy Research Scientific Computing Center (NERSC), a U.S. Department of Energy Office of Science User Facility located at Lawrence Berkeley National Laboratory, operated under Contract No. DE-AC02-05CH11231.

I am immensely grateful to my Thesis Supervisor, Prof. Adam Willard, for his invaluable mentorship throughout my PhD journey. Adam gave me the perfect balance of guidance and scientific freedom to explore new research directions. He provided me with great ideas while also supporting the direction I wanted for my work, of course, never letting me lose sight of the bigger picture. Thank you for supporting my scientific development and for imparting not just technical but also interpersonal skills, such as the effective communication of complex research to a wider audience.

I also extend my gratitude to my thesis committee, Prof. Jianshu Cao and Prof. Keith Nelson for their helpful guidance. Prof. Cao's advice was instrumental in developing the model presented in Chapter 4.

I also want to thank the Willard Group for their support over the years. Current and former members Ardavan Farahvash, Henrik Heelweg, Caelan Brooks, Yoon Park, Dina Sharon, Linsey Nowak, Julia Nauman Dylan Suvulu, Amr Dodin, Michiel Niessen, Yizhi Shen and Kyaw Myint with whom I had the pleasure to work with. Thank you for the interesting scientific discussions during subgroup and group meetings. It was really an enriching experience to work in a group with such diversity in perspectives, your questions and suggestions helped me direct my work to do better science. A special thanks to Amr for his mentorship during my initial days in the lab. His patience in discussing the models in the early part of this thesis and his insightful suggestions have been invaluable.

This work was made possible with the help of my experimental collaborators at MIT: Prof. Gabriela Schlau-Cohen's group in the Department of Chemistry, and Prof. Mark Bathe's group in the Department of Biological Engineering. In particular, Stephanie Hart and James Banal were responsible for all the experiments I present in Chapter 5, while also helping me model the theory around their observations. The insights presented in Chapter 6 were only possible with the experimental work of Jeffrey Gorman and Stephanie Hart, and the work of Torsten John carrying out the Molecular Dynamics simulations. I would also like to thank Prof. Bathe for all his guidance and helpful advice, some of which led to the development of the workflow in Chapter 7.

Of course, this thesis could not have been possible without all of the mentors I have had over the years. Starting from my undergraduate advisor, Prof. Carlos Arango. Carlos led me to the path of quantum chemistry, by teaching the first classes I ever took on quantum and statistical mechanics, and also by mentoring me through my undergraduate research and thesis. He gave me invaluable advice on science and life and motivated me to apply for graduate school. Prof. Frank Huo, from the University of Rochester, who gave me the opportunity to work with him on my first-ever exciton-related project. Thank you Frank for all your guidance and mentoring. I would also like to thank other mentors I was fortunate to have during my PhD. Jonathan Moussa, my mentor at the MolSSI, for all of his input on the molecular package developed in the last chapter. Julia Rice and Mario Motta, from my time as an intern at IBM. Thank you for being amazing mentors and teaching me so much during my research internship. I thoroughly enjoyed those two summers working alongside the Quantum Applications team.

I also want to thank all of the friends I have made during my time at MIT. My Chemistry cohort: Ardy, Amogh, Daniel, Jet, Jinyi, James, Alex, Soohyun, Natalie, Cliff, Vyshnavi and Mikaila. You were among the first friends I made here at MIT, and I am grateful for having been able to share my first-year struggles with you. My friends at the Colombian Association: You made me feel at home, even though I was thousands of kilometers away. Mohit: A constant in an ever-changing journey, your unwavering support has been invaluable. I have no doubt you will achieve great things after graduate school. To Dhanashri, for quickly becoming one of my best friends. It was a joy to have been roommates and share my obsession with coffee with you. Dalit, Yosh, Kartik, Sam, Nitish and my roommates Daniela and Alex, whom I feel I have known for years. Thank you for all the brunches, dinners and game nights. Being in the company of such amazing people provided comfort amidst the challenges of my research. Also, to my friends back home: Although we could only see each other once a year, your support was crucial for me during this time.

I also owe a tremendous debt of gratitude to my family. To my parents, Maria del Pilar and Ramiro, for their unwavering trust in my ability to accomplish whatever I set my mind to. I really have no words—or pages left on this thesis—to thank you both for the countless sacrifices you have made for me over the years.

Thank you, Dad, for believing in my potential, sometimes even more than I did. Without your confidence and support, my journey to MIT might never have begun. Thank you, Mom, for sparking my passion for science. I vividly recall the day I returned from school, frustrated with chemistry and redox reactions. Your patient explanation not only resolved my confusion but inadvertently set me on the path to this very PhD. And to my brother, Juan Pablo, for being my best friend and travel companion. I could not have wished for a better sibling and ally than you.

Also to my extended family, my uncles, aunts and cousins. To my grandpa, Gildardo Morales, the proudest *abuelo*, who sadly could not see me graduate.

And last but not least, I want to thank Avan, the brightest highlight of my graduate school experience. Being far from home was challenging, but with your support, I found a new sense of belonging. Thank you for being by my side through this emotional rollercoaster.

Dedication

In loving memory of my *abuelo*, Gildardo Morales, who never stopped believing in me.

Contents

List of Figures

List of Tables

Chapter 1

Introduction

Organic semiconductors promise to be a cost-effective and environmentally friendly alternative to inorganic electronics, due to their flexibility, temperature stability, and the abundance of their foundational materials [4, 58]. Organic electronics, as seen in applications ranging from photovoltaics [125] to transistors (TFTs) and light-emitting devices (OLEDs) [47, 58], have rapidly cemented their importance in modern technology. Intrinsically, the performance of these materials is governed by the absorption and emission of their low-lying excited states. Further advances in the field of organic electronics require a deep understanding of the electronic structure of these low-lying excitations and their photophysical pathways, in order to produce devices with unique and improved properties.

Central to organic semiconductors are photoactive materials such as chromophores or dyes. An extensive π-conjugated system—alternated single and double bonds—allows these molecules to absorb light in the visible spectrum (400–700 nm). The strong absorption in this range is predominantly a result of excitations to low-lying states, which significantly dictates the photophysics of chromophores. Upon photoexcitation, *e.g.,* by a photon, an electron is created in the lowest unoccupied molecular orbital (LUMO) and a "hole" in the highest occupied MO (HOMO). In chromophores with an extended conjugated π-system, such as cyanines [73, 99], squaraines [8], rylenes [100, 132], and acenes [4], the HOMO-LUMO gap is small resulting in Coulombic attraction between the electron and "hole", with the pair forming a quasi-particle—an exciton.

These molecules also exhibit easily tunable HOMO/LUMO levels, making them prime candidates for photovoltaic and optoelectronic applications.

The unique characteristics of organic semiconductors are not solely dependent on their chemical structure, as the properties of these materials can also be modulated using geometric design. An assembly of semiconducting moieties can be precisely arranged so as to control the dynamics of the prepared exciton. These systems, often termed *excitonic circuits*, can be designed to control the size, location, and energy of the exciton spread across the molecular framework [32, 51].

Through millions of years of evolution, nature has mastered the art of leveraging excitons. In the process of photosynthesis, plants capture sunlight in the light-harvesting complexes—associated dyes and proteins—where photons are channeled as excitons into reaction centers, which then catalyze water splitting to produce chemical energy [111, 122, 124]. Plants afford the precise control needed to transport excitons, from capture to chemical energy, by precisely fixing the position and orientation of chromophores via protein scaffolding. This naturally occurring strategy offers a template for designing synthetic systems for various artificial applications, such as signal processing [20], photovoltaics [18, 130], photocatalysis [147], imaging [83, 84] and quantum information [27, 28].

This thesis delves into the intricacies of exciton dynamics within molecular excitonic circuits and the control enabled by precisely positioning chromophores through macromolecular scaffolding, such as proteins, DNA, or metal-organic frameworks [130, 138]. The remainder of this chapter will introduce theories for describing exciton states and the coupling between them, and discuss the influence of a thermal bath on their dynamics.

The first part of this thesis explores the relationship between molecular configuration and coherent exciton dynamics, employing general mathematical models that account for both the system and its thermal environment. Chapter 2 examines the potential and limitations of controlling excitons via circuit geometry, aiming to realize quantum computing operations within these circuits. This chapter proposes a foundational strategy for embedding quantum operations into excitonic circuits, whereas

Chapter 3 extends the approach to more sophisticated quantum algorithms. The latter also examines the effect of a thermal bath on the delicate equilibrium of an exciton delocalized in a molecular circuit, introducing an atomistic framework to assess the role of environmental fluctuations. Chapter 4 advances this discussion by presenting a method for directing the coherent transport of excitons in circuits, essential for the development of effective organic molecular circuits.

Building upon the established principles of exciton transport and delocalization, the second part of the thesis presents DNA nanostructures as a precision tool for dictating circuit geometries. Chapter 5 explores exciton manipulation through an atomistic strategy, combining molecular simulations with the calculation of short and long-range electronic couplings. Subsequently, Chapter 6 delves into the intricate connection between photophysical properties and circuit geometries. Finally, Chapter 7 introduces a high-throughput computational workflow that links DNA scaffolding with circuit geometries and exciton properties, offering a promising method for the design of programmable excitonic circuits.

1.1 Exciton Theory

Frenkel exciton theory.

It is convenient to describe the excited state of an N-molecule system on a reduced basis of single-molecule excitations. If one then assumes that each molecule can only access one ground and one excited state, then the basis can be represented with that of the Frenkel exciton (FE) model [61, 43]. Specifically, the generic Hamiltonian of the Frenkel model is given by,

$$\hat{\mathcal{H}} = \sum_{m=1}^{N} \epsilon_m \left|m\right\rangle \left\langle m\right| + \sum_{m \neq n}^{N} V_{mn} \left|m\right\rangle \left\langle n\right|, \tag{1.1}$$

where $|m\rangle$ is the basis state where molecule m is in the excited state (with all other molecules in the ground state), ϵ_m is the energy of this basis state, and V_{mn} is the electronic coupling between the states $|m\rangle$ and $|b\rangle$.

A Frenkel excitation therefore implies the electron and the hole are localized in the same molecule, resulting in an exciton with a small radius. An exciton delocalized in a chromophore dimer as described by the Frenkel model is illustrated in Fig. 1-1. In this representation, the electronic coupling V_{mn} is defined as the overlap between a pair of FE states,

$$V_{mn} = \langle m|\hat{H}|n\rangle. \tag{1.2}$$

This simple and computationally efficient model has been widely used in the study of excited multi-chromophoric systems [14, 134, 139]. Although the Frenkel model omits the influences of higher-order excitations, many-body effects, nuclear relaxation, and the specific details of molecular electronic structure, it has been found to be remarkably accurate for reproducing the results of experimental and higher level theory when appropriately parametrized for organic conjugated molecules. Therefore, the Frenkel model is employed as an initial approach to excitonic circuits for Part I of this thesis. In Chapter 2 and 3, the FE model is used to describe excitonic circuits composed of coupled chromophores, mapping quantum computing operations. Chapter 4 will delve further into the directional flux of a Frenkel exciton between coupled sites.

Charge transfer excitons.

While the Frenkel exciton provides an accurate description in most excitonic circuits, in closely packed (< 4Å) chromophore aggregates, spatial overlap between MOs allows for the transfer of an electron (hole) between neighboring molecules. In this regime, the Kasha exciton model breaks down, as it operates under the premise that electron overlap between chromophore molecules is small [77, 87, 88]. As a result, such a system can no longer be described by the Hamiltonian in Eq. 1.1. The most general Hamiltonian expression that can explain the state of a single exciton in both the strongly-bounded (*Frenkel*) and weakly-bonded (*Wainner-Mott*) limits can be written

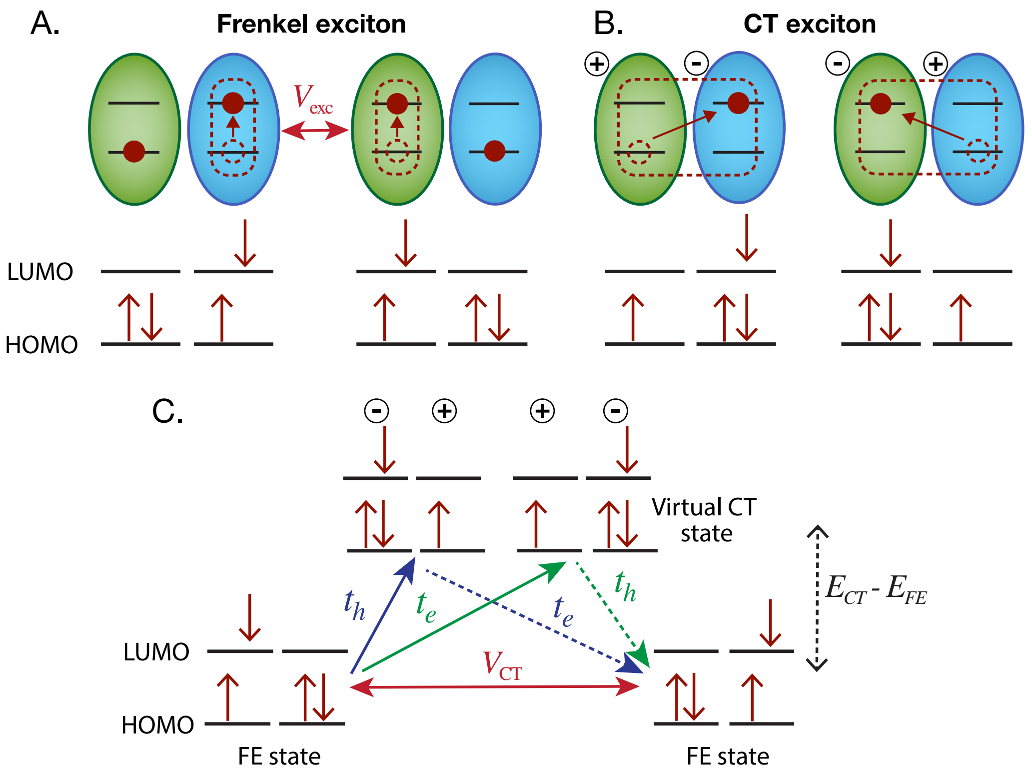

Figure 1-1: Schematic illustration of an exciton delocalized in a chromophore dimer. (A) The neutral Frenkel states resulting from a local excitation, and (B) the charge transfer states that result from the electron/hole transfer between neighboring chromophores. (C) Illustration of the charge transfer-mediated exciton coupling introduced in the text, V_{CT} (Adapted from Ref. [77]).

as [9, 79],

$$\begin{aligned}\hat{H}_{el} = &\sum_{mn}(V_{mn} - U(0)\delta_{mn})c_m^\dagger c_n d_m^\dagger d_n \\ &+ \sum_n [t_e c_n^\dagger c_{n+1} + t_h d_n^\dagger d_{n+1} + h.c.] \\ &- \sum_{n,s\neq 0} U_{\text{CT}}(s) c_n^\dagger c_n d_{n+s}^\dagger d_{n+s}, \end{aligned} \tag{1.3}$$

where $c_n^\dagger(c_n)$ creates (annihilates) an electron in the LUMO of chromophore n, $d_n^\dagger(d_n)$ creates (annihilates) a hole in the HOMO and $h.c.$ is the hermitian conjugate. The first term of this equation accounts for the Frenkel exciton contribution, with V_{mn} the Coulombic coupling between chromophore n and m, as defined in Eq. 1.2, and $U(0)$ is the local exciton binding energy. The last two terms in Eq. 1.3 contain the

CT contribution: The second term accounts for the nearest-neighbor (NN) transfer of an electron (hole), mediated by the electron (hole) transfer integral, t_e (t_h). The last term represents the interaction between anion-cation pairs, or an electron and hole separated by s NNs with a Coulomb binding energy $U_{\text{CT}}(s)$. In organic chromophores, low dielectric constants allow charge transfer only between NN molecules, so for $s = 1$ $U_{\text{CT}}(1)$ becomes,

$$U_{\text{CT}} = e^2/(4\pi\varepsilon_0\varepsilon_R r). \tag{1.4}$$

Here, r is the separation between the molecules, while ϵ_0 and ϵ_R are the dielectric constants of vacuum and water, respectively. The electron and hole integrals are defined as,

$$\begin{aligned} t_e &= \langle L^{(1)}|h|L^{(2)}\rangle \\ t_h &= -\langle H^{(1)}|h|H^{(2)}\rangle, \end{aligned} \tag{1.5}$$

where $L^{(1)}$ and $H^{(1)}$ are the LUMO and HOMO of molecule 1, respectively, and h is the 1-electron Hamiltonian.

A similar expression to Eq. 1.2 can be derived for the short-range CT coupling by considering the energy-transfer process described in Fig. 1-1C. This two-step process requires the transfer of a hole(electron) and electron(hole) pair, through a virtual CT state with energy $E_{CT} - E_{FE}$. The coupling can therefore be written as [77, 79],

$$V_{\text{CT}} \approx -2\frac{t_e t_h}{(E_{\text{CT}} - E_{\text{FE}})}, \tag{1.6}$$

where $E_{\text{CT}} - E_{\text{FE}}$ is the energy gap between the CT state and the neutral Frenkel exciton. This energy gap can also be described in terms of the local and CT binding energies, by considering the energy of an unbound CT pair, $E_{\text{CT}}^{\text{unb}} \equiv I_P - E_A + P$, where I_P, E_A and P are the ionization potential, electron affinity and polarization energy, respectively. The energy difference between the unbound CT pair and the

FE/CT energies is the corresponding binding energy,

$$\begin{aligned} E_{\mathrm{CT}} &= E_{\mathrm{CT}}^{\mathrm{unb}} - U_{\mathrm{CT}}, \\ E_{\mathrm{FE}} &= E_{\mathrm{CT}}^{\mathrm{unb}} - U(0). \end{aligned} \tag{1.7}$$

Therefore, $E_{\mathrm{CT}} - E_{\mathrm{FE}} = U(0) - U_{\mathrm{CT}}$. This expression is convenient as the FE/CT energy gap is difficult to obtain computationally and experimentally. In contrast, the local binding energy is known to have little impact in the overall coupling V_{CT}, and can usually be approximated as a constant [152].

In most organic systems, the energy gap $E_{\mathrm{CT}} - E_{\mathrm{FE}}$ is larger than the interaction terms in Eq. 1.3, V_{mn} and t_e/t_h. As a result, the Frenkel and CT exciton states can be solved separately,

$$\hat{H}_{el} = \hat{H}_{\mathrm{FE}} + \hat{H}_{\mathrm{CT}} + \hat{H}_{\mathrm{FE+CT}} \tag{1.8}$$

with $\hat{H}_{\mathrm{FE}}$ given by Eq. 1.1, and

$$\hat{H}_{\mathrm{CT}} = \sum_n [t_e c_n^\dagger c_{n+1} + t_h d_n^\dagger d_{n+1} + h.c.] + \sum_n U_{\mathrm{CT}} c_n^\dagger c_n d_{n+1}^\dagger d_{n+1}. \tag{1.9}$$

The last term $\hat{H}_{\mathrm{FE+CT}}$ is included to account for the interaction between FE and CT states, which becomes significant with decreasing energy gap between these states. Strong interaction between the Frenkel and charge transfer excitons has been observed in chromophores with large π-conjugated systems, such as perylenes [78, 79, 132, 153]. In these systems, the excitation of the Frenkel state will be rapidly followed by nuclear relaxation and CT, a phenomenon referred to as excimer formation.

I will employ the expanded exciton model above to study the photophysical properties of closely-packed chromophore dimers in Chapters 5-7.

1.2 Exciton Dynamics in a Thermal Environment

In describing the evolution of a system of interactive chromophores with a realistic framework we must account for both the effect of intermolecular interactions, described by the coupling V_{mn}, and the interactions of each dye and its local thermal environment or *bath.* Phonon modes in the bath couple with the chromophore's electronic transitions and affect electron transfer between molecular units. These modes can arise, for example, from the dye's chemical structure, *i.e.,* normal vibrational modes, or from collective motions of the solvent.[114]

A simple approach for describing the effect of these thermal fluctuations is by separating the contributions of the bath from the system Hamiltonian,

$$\hat{\mathcal{H}} = \hat{\mathcal{H}}_S + \hat{\mathcal{H}}_B + \hat{\mathcal{H}}_{S-B} \tag{1.10}$$

Where $\hat{\mathcal{H}}_S$ is the system Hamiltonian, $\hat{\mathcal{H}}_B$ describes the thermal bath and $\hat{\mathcal{H}}_{S-B}$ describes the system-bath coupling.

For simplicity, we can assume that the bath is approximated as a collection of N (*i.e.*, one for each dye molecule) independent harmonic oscillators,

$$\hat{\mathcal{H}}_B = \sum_m^N \sum_a \frac{\hbar}{2} \left(\mathbf{P}^2_{m,a} + \omega^2_{m,a} \mathbf{Q}^2_{m,a} \right), \tag{1.11}$$

where the first summation is taken over the dye molecules, the second summation is taken over oscillator frequencies, $\omega_{m,a}$, and $\mathbf{Q}_{m,a}$ and $\mathbf{P}_{m,a}$ denote the position and momentum of the oscillator state. In this framework, we assume that each dye interacts with its own bath.

The influence of the bath in the electronic transition is typically manifested as a difference in the wavelength of light absorbed vs emitted – often referred to as a *Stokes shift.* Interaction with a given bath mode of frequency ω_m, a leads to a shift in the nuclear coordinates of the ground and excited states, which results in the release of vibrational energy upon electronic excitation. The reorganization energy, denoted as λ, quantifies this nuclear relaxation process and is a good measure of the system-bath interaction.

Intermolecular interactions will drive the transport of neutral excitons and charged particles in the presence of thermal fluctuations. The nature of this excitonic transport will depend on the relative strength of the coupling V_{mn} within the circuit, compared to the strength of intramolecular interactions of each chromophore with its surrounding bath [32]. For instance, in molecular circuits with large nearest-neighbor separation V_{mn} is often negligible with respect to the intramolecular coupling, measured by λ. Exciton transport in these systems is driven by incoherent or Förster energy transfer, where particles are seen as "hopping" between chromophore sites [129]. When intermolecular coupling increases with respect to intramolecular coupling, exciton and charge transport are mediated by coherent dynamics. Here, the excitation is considered as being delocalized across the array of chromophores interacting with each other. Both coherent and incoherent transfer are of paramount importance in biological systems, enabling the transfer of the exciton within the LHCs and to the reaction center. In the limit of very small or large coupling strength with respect to the bath, theories such as Förster and Redfield are often employed, respectively.

Light-harvesting complexes have evolved to achieve reduced reorganization energies of less or about 100 cm^{-1} [32, 81]. Therefore, electron transport between closely-packed chromophores in this environment will be dominated by coherent dynamics. For the first part of this work, Chapters 2-4, I will undertake the problem of exciton transfer and dynamics within the coherent regime, assuming Frenkel excitons that couple weakly to the thermal bath. The system dynamics are described using a reduced density matrix (RDM) approach, that enables the treatment of both system and bath modes quantum mechanically. Chapter 2 approximates the effect of the environment analytically through a minimal dephasing/dissipation model, while Chapters 3 and 4 treat the interaction with phonon modes explicitly via the Redfield approximation.

It is important to acknowledge that, between the strong- and weakly-coupled bath regime, we also find an intermediate regime where bath relaxation is on the same order of magnitude as the electron transfer. In this regime, the Redfield approximation is no longer valid, and alternative methods are often used instead. These methods include those based on the path-integral approach [55], mixed quantum-classical approaches [119], or extensions of the Redfield model, such as the polaron transformation [52, 136]. To describe the breadth of inter- and intra-molecular interactions in organic semiconductors a more precise description of the bath modes is adopted in Chapter 3, aided by a classical description of the bath via room-temperature molecular dynamics (MD) simulations paired with electronic structure calculations of the excited state. This MD and quantum mechanical combined approach is also adopted in subsequent chapters to describe the Coulombic and charge-transfer interactions in chromophore aggregates.

Part I

Control of Exciton Coherent Dynamics: A Frenkel Exciton Model

Chapter 2

Molecular Excitons for Quantum Computing Platforms

2.1 Introduction

The elementary component of a quantum computer—a qubit—is a two-state quantum system. A qubit can be constructed from many different physical systems, including a pair of coupled organic dye molecules sharing a single exciton. Using this kind of qubit it is therefore possible, at least in principle, to develop quantum computing elements that operate via the excited state dynamics of specifically designed *excitonic circuits* comprised of multiple dye molecules in precise geometric arrangements. In this chapter, I introduce a general strategy for designing excitonic circuits for quantum computation. I apply this strategy to identify fundamental bounds on the computational complexity that these circuits can support and identify the physical requirements for performing universal quantum logic gate operations on one- and two-qubit systems. This study therefore sets the groundwork for enabling the development of programmable dye-based quantum computing elements.

As introduced in Chapter 1, the evolution of excitons within a circuit is determined by the intermolecular electronic coupling network and the electronic properties of the dyes. The electronic coupling between dye molecules is programmed by their intermolecular spacing and orientation [33]. Supermolecular support structures can be used to fix the positions and orientation of the dye molecules, which in turn can enable the dynamical control of the shared exciton required to implement state transformations for quantum computation.

Quantum computing offers several key advantages over traditional classical computing and is poised to make a transformative impact on certain areas of the information sciences, such as cryptography and molecular simulation[45, 121]. However, despite enormous potential for broad technological impact, quantum computing presents unique implementation challenges that have thus far limited it to only a few physical systems [48]. This includes optical cavities [117, 57], trapped ions [35, 3, 62], molecular spins [65, 63], superconductors [150], quantum dots [96, 101] and solid state color centers [1, 31]. From the standpoint of quantum computing, each of these qubit systems has its own strengths and limitations. Practical application of any specific system will require exploiting its strengths while mitigating its limitations. Characterizing the strengths and limitations of new potential qubit systems, such as those made from excitonic circuits, is an important step in the development of quantum information technologies.

A limitation that affects nearly all qubit systems is the requirement for low operating temperatures. This requirement is intrinsic to the physics of some systems, such as superconducting and trapped atom qubits. Low temperature is also used to reduce the effects of environmental noise, which can destroy the delicate phase information required for quantum computation. Unfortunately, achieving and maintaining the low temperatures that are required for these systems is both expensive and impractical. Qubit systems with the ability to maintain and share their phase information in noisy thermal environments could significantly improve the scalability of quantum computing technologies. [115, 53]

The dye molecules that comprise excitonic circuits are highly sensitive to environmental noise and exhibit coherence times that are generally much shorter than existing qubit systems. On the other hand, the dye molecules can be strongly coupled so as to enable rapid transfer and evolution of phase information. Viable quantum computing in excitonic circuits will require balancing short coherence times with the ability to produce strong intermolecular electronic couplings. Theoretical models, such as those presented here, play an important role in developing an understanding of this balance, its potential implication, as well as its physical limitations.

The focus of this chapter is to explore the opportunities and limitations in engineering quantum dynamics in excitonic molecular systems. We show here and in Ref.[27], that these dynamics can be programmed and exploited to realize a broad range of quantum operations, including, in particular, a universal set of quantum logic gates [116, 90]. Promisingly, coherent dynamics in excitonic molecular systems are seen to survive moderate levels of environmental noise, suggesting they may be candidates for a new class of quantum materials with information processing applications.

I present a general strategy for programming the dynamics of excitons in the design of excitonic circuits. Importantly, this programming enables the implementation of unitary transformations, such as those that form the basis for quantum information processing. To accomplish this implementation we can map qubit states onto the electronic excitation states of coupled dye molecules. For example, the basis states of a two-qubit system, *i.e.*, $\{|00\rangle, |01\rangle, |10\rangle, |11\rangle\}$, can be mapped onto a basis of localized single molecule excitations in an excitonic circuit made of four molecules. By representing qubit states as electronic excitations, rather than rotational or vibrational excitations, our approach differs from those that have been proposed previously.

An excitonic representation of a qubit system naturally supports quantum properties such as superposition, *i.e.*, through excitonic delocalization, and can encode coherence and entanglement in multi-qubit systems. It is important to note that the mapping presented here, *i.e.*, whereby each state of a system of qubits is represented by the state of a single exciton in a system of multiple dye molecules, encodes entanglement inefficiently, leading to significant system size scaling problems. However, this scaling problem arises due to the difficulty of representing multi-particle entanglement using a single particle and is therefore a consequence of the limited mapping we propose. As such, more sophisticated mappings that allow multiple excitons can significantly reduce (or altogether eliminate) this issue. However, while a multi-exciton mapping solves the scaling problem, it introduces physical effects, such as exciton-exciton interactions, that significantly complicate theoretical formulation. These complications represent significant future challenges that must be overcome to enable quantum computing through exciton circuits. The work we present here demonstrates how the geometric arrangements of excitonic dyes can be used to encode a quantum transformation, a key first step towards enabling quantum logic operations in excitonic systems.

In the following section, I present the details of this strategy and its application to the set of universal quantum logic gates. Then, we simulate the performance of these gates under varying environmental conditions.

2.2 Exciton Circuit Model

In this chapter, I employ the Frenkel exciton model introduced in Section 1.1 to describe excitonic circuits of coupled molecular dyes. We assume the configurations of dye molecules in these circuits are defined by their center of mass positions and orientations. For the purpose of illustration, we begin with the assumption that the coupling between dye molecules in Eq. 1.1 can be represented by the point dipole approximation,

$$V_{ij} = \frac{1}{4\pi\varepsilon_0}\frac{\vec{\mu}_i.\vec{\mu}_j - 3\left(\vec{\mu}_i.\mathbf{\hat{r}_{ij}}\right)\left(\vec{\mu}_j.\mathbf{\hat{r}_{ij}}\right)}{r_{ij}^3}, \tag{2.1}$$

where $\vec{\mu}_i$ is the transition dipole moment of excitation $|i\rangle$, $\vec{r}_{ij} = \vec{r}_i - \vec{r}_j$ is the displacement vector between the dyes, $\mathbf{\hat{r}_{ij}} = \vec{r}_{ij}/r_{ij}$ is the corresponding displacement unit vector and ε_0 is the vacuum permitivity. Alternatively, V_{ij} can be expressed as a function of molecular orientational coordinates as,

$$V_{ij} = \frac{1}{4\pi\varepsilon_0}\frac{|\mu_i|\,|\mu_j|\cos\theta_{ij} - 3\left(|\mu_i|\cos\varphi_i\right)\left(|\mu_j|\cos\varphi_j\right)}{r_{ij}^3}, \tag{2.2}$$

where θ_{ij} is the twist angle between the dipole moments of the pair of dyes, and φ_i denotes the angle between μ_i and the vector $\hat{r}_{ij}$, as illustrated in Fig. 2-1. In later chapters, we will increase the complexity of the definition of molecular coupling for more accurate approximations.

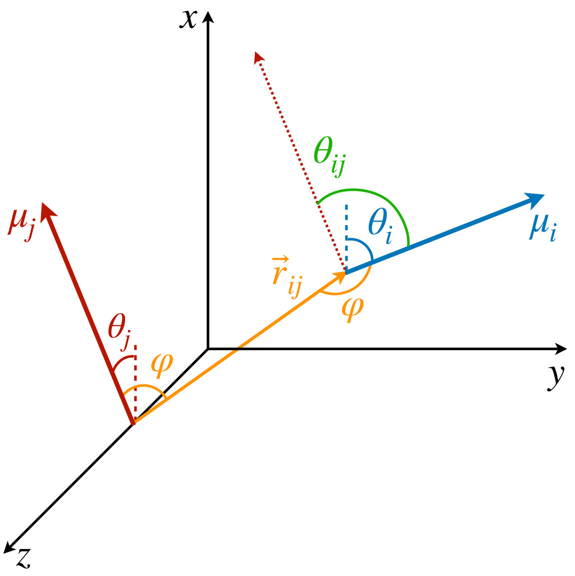

Figure 2-1: Coordinates defining the relative arrangement of dye molecule pairs
.

Despite its simplicity, the Frenkel exciton model encodes all of the information on the system dynamics we need for the purposes of this chapter. As we will see in the following sections, the form of the Frenkel Hamiltonian allows us to easily map unitary qubit operations onto excitonic circuit geometries. As has been shown in previous studies [134, 98], the details of the molecular structure of the dyes, such as the disorder of the molecular system, can be encoded in the elements of the Hamiltonian. In the next chapter, we will show that the parameters of the Frenkel Hamiltonian can be determined from classical all-atom molecular dynamics together with semiempirical electronic structure calculations [28, 54, 134, 98].

2.3 Mapping Quantum Operations into Excitonic Circuits

Engineering exciton dynamics

Molecular excitonic systems with tunable geometry present a unique opportunity to design systems that realize specific quantum transformations. This approach is illustrated in Fig. 2-2 for schematic quantum circuits. In particular, closed system quantum dynamics generate a family of unitary transformations, $\{\hat{U}(t) \equiv e^{-\frac{i}{\hbar}\hat{\mathcal{H}}t}\}$, from the system Hamiltonian, $\hat{\mathcal{H}}$. A system Hamiltonian, $\hat{\mathcal{H}}$, can be represented by a target unitary transformation, $\hat{U}_{\text{target}}$, through the relationship,

$$\hat{\mathcal{H}}_\tau \equiv \frac{i}{\tau}\hbar \ln \hat{U}_{\text{target}} \tag{2.3}$$

where τ gives the transformation time at which $\hat{U}_{\text{target}}$ is realized. The family of Hamiltonians, $\{\hat{\mathcal{H}}_\tau\}$, are scalar multiples that differ only in the transformation time.

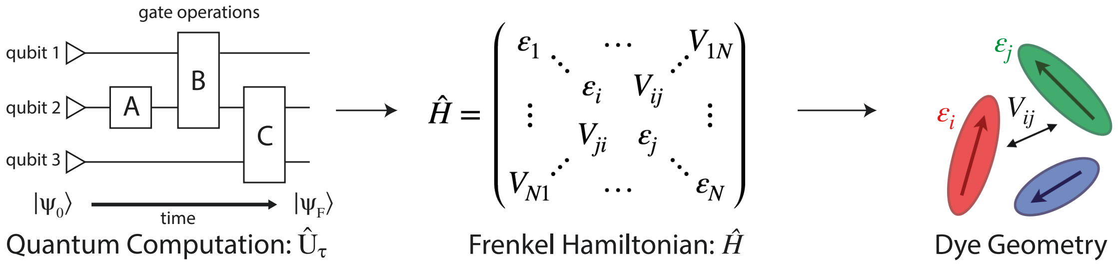

Figure 2-2: Encoding quantum operations into the dynamics of a physical system. A series of unitary operations, such as gates in a quantum circuit, can be equivalently represented as a Hamiltonian matrix. A physical system of interacting molecules is implied when this matrix is assumed to be a Frenkel Hamiltonian. If this physical system can be constructed, then its excited state dynamics will encode the result of the quantum computation.

Systems comprised of molecular dyes are promising for these applications as their Hamiltonians can be tuned by modifying the spectral properties and geometry of the constituent dyes. Equations 1.1- 2.3 taken together prescribe a method for designing excitonic circuits that implement a given unitary transformation. Specifically, Eq. 2.3 and 1.1 define a set of energetic constraints on the coupling and site energies of the dyes while Eq. 2.1 translates these to geometric constraints on the dye assembly. A physical system implementing a unitary transformation, $\hat{U}_{\text{target}}$, must therefore satisfy these geometric constraints.

Mapping the universal quantum gates.

We now illustrate the use of this approach by considering the implementation of a universal set of quantum gates in a dye system. These simple transformations are widely studied as the building blocks of all quantum algorithms. We will show that the one-qubit NOT, Hadamard, and $\pi/8$ transformation, and the entangling two-qubit CNOT transformation (shown in Table 2.1) can be implemented in excitonic dye systems. Moreover, we find that excitonic circuits have far more flexibility than required to realize these transformations, allowing us to design around practical limitations (*e.g.* limited dye libraries), optimize performance in the presence of noisy environments and even design systems that are easier to prepare and measure with a given experimental set up.

Each state $|i\rangle$ can be identified in the site basis by the dye molecule where the excitation is localized. Each of these dyes is then associated with a state of the qubit register, mapping the register state to the exciton location. We will then denote each dye by the qubit state from which it is mapped. For a one qubit gate, the qubit states $|0\rangle$ and $|1\rangle$ are mapped to the states $|A\rangle$ and $|B\rangle$ of a two dye system (with molecules A and B), respectively, where $|A\rangle$ corresponds to the state where only dye A is excited and $|B\rangle$ corresponds to the state where only dye B is excited. Likewise, for a two qubit gate the qubit states $|00\rangle, |01\rangle, |10\rangle$ and $|11\rangle$ map to the states $|A\rangle, |B\rangle, |C\rangle$ and $|D\rangle$ of a four dye system. Note that, within this approach, mapping n qubit states will require the preparation of 2^n dye molecules, thus providing strong practical limitations on the complexity of quantum computation that can be reasonably represented with an excitonic circuit. For example, the state of a 10-qubit operation requires the use of 1024 dye molecules. Despite this practical limitation, however, the platform that we propose provides an important initial step towards establishing the feasibility of more sophisticated potential approaches. For example, it would be possible to significantly reduce the number of required dye molecules by expanding the framework to include multiple excitations. Because the preparation and spectroscopic analysis of singly-excited systems are more straightforward than those for systems with multiple excitations, the model described in Sec. 1.1 is more appropriate for an initial study for excitonic quantum circuits.

The simplest of these transformations is the $\pi/8$ phase gate. This gate increases the relative phase between states $|0\rangle$ and $|1\rangle$ giving the operation $\hat{U}_{\pi/8}$ and corresponding Hamiltonian in Table 2.1. This Hamiltonian leads to two intuitive constraints on

Table 2.1: The unitary transformations corresponding to the universal quantum logic gates and the corresponding system Hamiltonians as mapped from Eq. 2.3.

Gate	Unitary operator	Hamiltonian
NOT	$\hat{U}_{\text{NOT}} = \begin{pmatrix} 0 & 1 \\ 1 & 0 \end{pmatrix}$	$\hat{\mathcal{H}}_{\text{NOT}} = \frac{\pi\hbar}{2\tau}\begin{pmatrix} -1 & 1 \\ 1 & -1 \end{pmatrix}$
Hadamard	$\hat{U}_{\text{Had}} = \frac{1}{\sqrt{2}}\begin{pmatrix} 1 & 1 \\ 1 & -1 \end{pmatrix}$	$\hat{\mathcal{H}}_{\text{Had}} = \frac{\pi\hbar}{2\sqrt{2}\tau}\begin{pmatrix} 1-\sqrt{2} & 1 \\ 1 & -1-\sqrt{2} \end{pmatrix}$
$\pi/8$	$\hat{U}_{\pi/8} = \begin{pmatrix} 1 & 0 \\ 0 & e^{i\pi/4} \end{pmatrix}$	$\hat{\mathcal{H}}_{\pi/8} = \frac{\pi\hbar}{4\tau}\begin{pmatrix} -1 & 0 \\ 0 & 0 \end{pmatrix}$
CNOT	$\hat{U}_{\text{CNOT}} = \begin{pmatrix} 1 & 0 & 0 & 0 \\ 0 & 1 & 0 & 0 \\ 0 & 0 & 0 & 1 \\ 0 & 0 & 1 & 0 \end{pmatrix}$	$\hat{\mathcal{H}}_{\text{CNOT}} = \frac{\pi\hbar}{2\tau}\begin{pmatrix} 0 & 0 & 0 & 0 \\ 0 & 0 & 0 & 0 \\ 0 & 0 & -1 & 1 \\ 0 & 0 & 1 & -1 \end{pmatrix}$

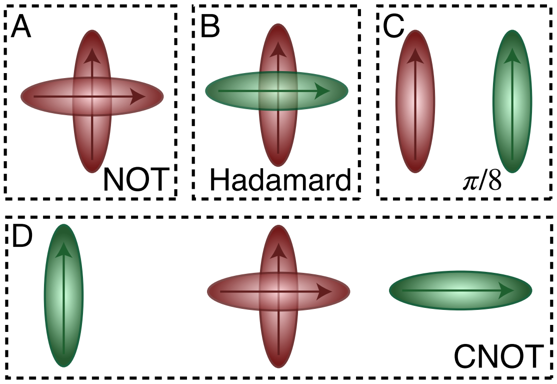

Figure 2-3: A schematic of the dye circuits representing the four universal quantum gates transformations.

the dye assembly—one on the coupling and the other one on the relative excitation energy of the dyes. First, since this gate does not induce transitions between qubit states, the dyes must be uncoupled, *i.e.* $V_{01} = 0$. Second, to allow the two states to acquire relative phase, the dyes must be non-degenerate with $\Delta\epsilon_{01} = \epsilon_0 - \epsilon_1 \neq 0$. These constraints are satisfied by any uncoupled dye heterodimer allowing for any pair of non-degenerate dyes and a broad range of possible geometric configurations, as illustrated in Fig. 2-3C. Moreover, the transformation time is given by $\tau = \pi/(4\Delta\epsilon_{01})$.

We now consider the single-qubit NOT gate, represented by the unitary operation $\hat{U}_{\text{NOT}}$, in Table 2.1. This transformation swaps qubit states $|0\rangle$ and $|1\rangle$ without modifying their relative phase. To ensure excitation transfer the two dyes must have non-zero coupling (*i.e.* $V_{01} \neq 0$). In addition, they must also be degenerate to ensure that the excitation fully transfers between the states. Thus, any coupled pair of degenerate dyes, *e.g.*, a homodimer, reproduces a quantum NOT gate Fig. (2-3A). Physically, this exploits the oscillatory energy transfer in a homodimer to coherently swap qubit states, where the NOT operation is realized at half the Rabi frequency, $\tau = \pi/(2V_{01})$, when population inversion is maximized.

In a similar way, we can identify a molecular system that represents the action of a Hadamard gate on an input qubit state. This gate is represented by the operator, $\hat{U}_{\text{Had}}$ (Table 2.1). The Hadamard gate transforms an initial state into a superposition of the qubit states $|0\rangle$ and $|1\rangle$. The system described by $\hat{\mathcal{H}}_{\text{Had}}$ is illustrated in Fig. 2-3C. This system corresponds to a heterodimer coupled by $V_{01} = \pi/(2\sqrt{2})\tau$, where the relative transition energies of the dyes are given by $\Delta\epsilon_{01} = \pi/(\sqrt{2}\tau)$. We see that $\hat{\mathcal{H}}_{\text{Had}}$ impose an additional constrain on the system as the ratio of the energy difference, $\Delta\epsilon_{01}$, and the coupling between the dyes, V_{01}, must be equal to a constant factor: $\Delta\epsilon_{01}/V_{01} = 2$. Consequently, the coupling between the dyes in the heterodimer will be completely specified after we choose a value for $\Delta\epsilon_{01}$, and only a reduced set of dye spatial distributions will evolve with a Hamiltonian $\hat{\mathcal{H}}_{\text{Had}}$ for such a system.

The CNOT gate is an operator that acts over two qubits: one *control* qubit and one *target* qubit. If the *control* qubit is set to zero, then the operator does not act over the *target* qubit, but if the *control* qubit is set to 1, then the CNOT operator acts over the *target* as a NOT gate. The CNOT gate is represented by the 4×4 evolution operator, $\hat{U}_{\text{CNOT}}$ (Table 2.1). The control operation is represented in the upper left quarter of $\hat{U}_{\text{CNOT}}$, a 2×2 identity matrix, while the NOT operation is represented in the lower right quarter of $\hat{U}_{\text{CNOT}}$. The Hamiltonian that corresponds to this operator is given by $\hat{\mathcal{H}}_{\text{CNOT}}$. Correspondingly, a CNOT gate can be realized by a coupled homodimer representing the NOT operation, and two identical uncoupled dyes corresponding to the identity operation, as illustrated in Fig. 2-3D.

It is important to note that the circuits we propose effectively hard code the action of specific quantum unitary operations. Programmability of these circuits is achieved in their geometric design, thus limiting the flexibility of this platform as a universal quantum computer. For instance, a computation that requires the sequential action of two quantum logic gates on two qubits is represented by a different excitonic circuit than that of either of the individual gates operations. Our study provides a framework for simulating quantum physics and also for designing hard-coded quantum circuits performing pre-determined operations.

Exploiting additional degrees of freedom for selective excitation and measurement.

In the previous section, we found that unitary transformations impose remarkably lenient constraints, allowing for a broad range of possible excitonic circuits. This flexibility can be exploited to construct systems that are easier to experimentally initialize and measure. For two-dimensional operations, such as the one-qubit gates studied earlier, selective initialization and measurement of the two sites can be implemented through a polarization addressing scheme. In its most straightforward realization, this addressing approach can be achieved by selecting a configuration where the two dyes have orthogonal transitional dipole moments. Such a configuration is still able to support coupling between the two dyes through the second term of Eq. 2.1. Any desired superposition of sites can then be excited or probed by selecting the appropriate polarization of the excitation or measurement pulse. Real valued superpositions of the two dyes are then addressed by linear polarizations and complex-valued superpositions by elliptical polarizations.

Four-dimensional operations, such as the two-qubit CNOT gate, require a slightly generalized strategy since four possible states $\{|00\rangle,|01\rangle,|10\rangle,|11\rangle\}$ must be selectively initialized and measured. From $\hat{\mathcal{H}}_{\mathrm{CNOT}}$, we know different transition energies are associated with different states of the control qubit (i.e. first qubit). As a result, frequency ω_0 addresses the set $\{|00\rangle, |01\rangle\}$, and frequency ω_1 the set $\{|10\rangle, |11\rangle\}$. This allows the control qubit state to be selectively excited and probed by selecting the frequency of the excitation and probe pulses. Each of these pairs can then be oriented orthogonally to each other, with $|00\rangle$ orthogonal to $|01\rangle$ and $|10\rangle$ orthogonal to $|11\rangle$ (Fig. 2-3D). This arrangement then allows for a polarization addressing of the target qubit state, analogous to the two-dimensional approach.

These addressing strategies are of course not unique. However, they demonstrate how the excess degrees of freedom can be exploited to satisfy additional constraints imposed by experimental limitations (e.g. orthogonality for polarization addressing). Moreover, these constraints can be softened to satisfy other technical constraints. For example, polarization-addressed dyes can be placed in non-orthogonal configurations. While this reduces the specificity of the addressing procedure, it can increase the coupling between the dyes, mitigating the effect of environmental noise. In the next section, we explore how dye configurations can be tuned to optimize this type of trade-off.

In the Appendix A we present an analysis of the fundamental bounds on the complexity of operations that can be represented by a circuit of multiple coupled molecules.

2.4 Effect of a Phonon Bath in Mapped Operations

Open System Dynamics of a Two-level System

Thus far, we have restricted our attention to closed system dynamics where the state of the quantum system can be represented as a linear combination of the form $\psi = a_0 |0\rangle + a_1 |1\rangle$. In this setting, the system is isolated from the surroundings and retains all of its phase information as it evolves in time. However, when a system evolves in contact with a bath, environmental noise and the formation of uncontrolled system-bath entanglement lead to the gradual loss of phase information of the system. In the presence of this incomplete phase information, the state of the quantum system can no longer be represented by a wavefunction. Instead, the system state must be represented by a density matrix ρ [15]. In this matrix representation, the diagonal components, ρ_{ii}, give the population of state $|i\rangle$, playing an equivalent role to the probability amplitudes $|a_i|^2$. The complex-valued off-diagonal components, ρ_{ij}, are known as coherences and describe the phase information between states $|i\rangle$ and $|j\rangle$.

In the following sections, we will consider the evolution of the one-qubit gates in the presence of a noisy environment. This will allow us to examine the limitations and requirements of excitonic quantum information processing and illustrate the optimization of these quantum circuits. By taking advantage of the normalization condition, $|\alpha|^2 + |\beta|^2 = 1$, the density matrix of a two-level qubit can be conveniently represented by the density matrix

$$\rho(t) = \frac{1}{\sqrt{2}} \begin{pmatrix} 1 + \sigma_z(t) & \sigma_x(t) - i\sigma_y(t) \\ \sigma_x(t) + i\sigma_y(t) & 1 - \sigma_z(t) \end{pmatrix}, \tag{2.4}$$

where σ_x, σ_y and σ_z are real valued components of a 3D vector $\vec{\sigma}$ known as the Bloch vector. The properties of the density matrix constrain this vector to the sphere $|\vec{\sigma}| \leq 1$, which is referred to as the Bloch sphere.

In this compact representation, the evolution of a closed system reduces to solving the set of differential equations for the Bloch vector $\vec{\sigma}$, known as the Liouville-von Neumann equations. For a general Hamiltonian of the form $H = \epsilon_0 |0\rangle \langle 0| + \epsilon_1 |1\rangle \langle 1| + V_{01} |0\rangle \langle 1| + V_{01}^* |1\rangle \langle 0|$, these equations of motion are

$$\dot{\sigma}_x = \frac{i}{\hbar} \left(\Delta\epsilon_{01}\sigma_y + 2\mathcal{I}\left[V_{01}\right]\sigma_z \right), \tag{2.5a}$$

$$\dot{\sigma}_y = \frac{-i}{\hbar} \left(\Delta\epsilon_{01}\sigma_x + 2\mathcal{R}\left[V_{01}\right]\sigma_z \right), \tag{2.5b}$$

$$\dot{\sigma}_z = \frac{2i}{\hbar} \left(\mathcal{I}\left[V_{01}\right]\sigma_x + \mathcal{R}\left[V_{01}\right]\sigma_y \right), \tag{2.5c}$$

where $\mathcal{R}\left[V_{01}\right]$ and $\mathcal{I}\left[V_{01}\right]$ are the real and imaginary parts of the coupling V_{01} between the dye molecules, respectively. This yields a unitary evolution that is equivalent to the time-dependent Schrödinger equation.

In an open system, interaction with a noisy environment substantially modifies the system dynamics. Generally, these dynamics can be quite complicated, potentially showing substantial non-Markovian character that depends intricately on the structure and statistics of the environment. In this study, we aim to consider a simple model for the influence of the bath that relies minimally on the details of the local environment. As such, we will restrict our attention to simple phenomenological Markovian master equations of the Lindblad type [15]. In this model two major effects are included for a system of dye molecules coupled to a phonon bath. The *dephasing*, with rate

γ, describes random fluctuations in the energy levels of the dye molecules due to environmental noise. This leads to the loss of coherent phase information, manifesting in a decay in the off-diagonal components of ρ, or coherences. In addition, *dissipation*, with rate Γ describes the loss of excitation energy to the phonon bath as the system relaxes to the lower energy eigenstate. Including these dephasing and dissipation effects in Eq. 2.5, we arrive at an expression for the Bloch equations in an open system:

$$\dot{\sigma}_x = \frac{i}{\hbar}\left(\Delta\epsilon_{01}\sigma_y + 2\mathcal{I}\left[V_{01}\right]\sigma_z\right) - \frac{1}{2}\left(\Gamma + 2\gamma\right)\sigma_x, \tag{2.6a}$$

$$\dot{\sigma}_y = \frac{-i}{\hbar}\left(\Delta\epsilon_{01}\sigma_x + 2\mathcal{R}\left[V_{01}\right]\sigma_z\right) - \frac{1}{2}\left(\Gamma + 2\gamma\right)\sigma_y, \tag{2.6b}$$

$$\dot{\sigma}_z = \frac{2i}{\hbar}\left(\mathcal{I}\left[V_{01}\right]\sigma_x + \mathcal{R}\left[V_{01}\right]\sigma_y\right) + \Gamma\left(\frac{1}{2} - \sigma_z\right). \tag{2.6c}$$

The quantity $T_2 = 2/(\Gamma + 2\gamma)$ is often referred to as the total dephasing time while $T_1 = \Gamma^{-1}$ is called the dissipation or relaxation time. As in the case of the Frenkel exciton model described in Sec. 2.2, this simple model is used with the acknowledgment that more sophisticated approaches to these dynamics may be required to treat specific systems in future work.

In the following section, we will use Eq. 2.6 to model the dynamics of the NOT and Hadamard gates in order to illustrate the effects of environmental noise on the desired unitary transformation. For simplicity, we will restrict our attention to dyes with linear (as opposed to circular) transition dipole moments. This leads to a real valued coupling between the dyes $V_{01} = \mathcal{R}\left[V_{01}\right]$.

Employing a toy model to measure gate performance in an environment. The dynamics of the NOT and Hadamard quantum gates under the effect of phonon bath can be derived by solving the system of equations in Eq. 2.6, using the appropriate Hamiltonian in Table 2.1. The relative populations of the states of the two-level qubit system in the site basis, as well as the coherences at a a given time, t, can be extracted from the density matrix in Eq. 2.4. As an example, we examine the population dynamics of the NOT gate. Figure 2-4A shows the population dynamics of the state $|1\rangle$ under the effect of different dephasing rates. In the isolated case, the required state inversion of the input qubit (taking the qubit from $|0\rangle$ to $|1\rangle$ and from $|1\rangle$ to $|0\rangle$), is implemented by Rabi oscillations with a period 2τ. This first maximum corresponds to the time it takes the system to perform a single gate operation, before returning again to its initial state, at $t = 2\tau$. The oscillatory nature of the dynamics indicates that for a given configuration the NOT gate transformation is in fact realized at many times, specifically at any $\tau_n = n\tau$, where n is any odd integer. The oscillations in Fig. 2-4A are seen to decrease rapidly with increasing dephasing rate γ, since the coherence is mostly lost when the dephasing time, $1/\gamma$, is $\sim 1/3$ of τ.

The performance of a quantum gate can be quantified according to the schematic in Fig. 2-4B. In a closed system, a perfect NOT gate would interconvert 100% of the initial qubit between $|0\rangle$ and $|1\rangle$. However, dephasing (here shown for $\gamma \sim \tau$) reduces the amplitude of the Rabi oscillations, decreasing the amount of the excitation transferred to the desired state. At longer times, dephasing fully damps the oscillations leaving an equal (incoherent) mixture of $|0\rangle$ and $|1\rangle$ states. We then want to measure the state of the system at the minimum time it requires to perform the desired operation, τ, and the efficiency must be determined at $t = \tau$ (dotted red line in Fig. 2-4B).

Following this idea, we define a fidelity measure for a two-state excitonic circuit that quantifies the probability of measuring the correct outcome after the transformation is applied. This quantity includes the deviation of the state of the open system from that of the closed quantum system at time $t = \tau$ and the ability to perform the polarization addressing scheme proposed earlier. Describing the state of the system at a given time by the density matrix, ρ, in Eq. 2.4, the fidelity of the circuit can be defined by

$$\mathrm{Fid} = |\mathrm{Tr}\{\rho_{\mathrm{open}}(\tau)\rho_{\mathrm{closed}}(\tau)\}| \times \sin^2\theta_{ij}, \tag{2.7}$$

where ρ_{open} and ρ_{closed} are the density matrices describing the open and closed quantum systems, respectively. The trace expression in Eq. 2.7 quantifies the deviation of the open systems dynamics from the ideal closed system case. In general, the absolute value of this trace takes a value between 0 and 1. Most notably, if $\rho_{\mathrm{closed}} = \rho_{\mathrm{open}}$, as is the case for a system well isolated from environmental noise, the result is that

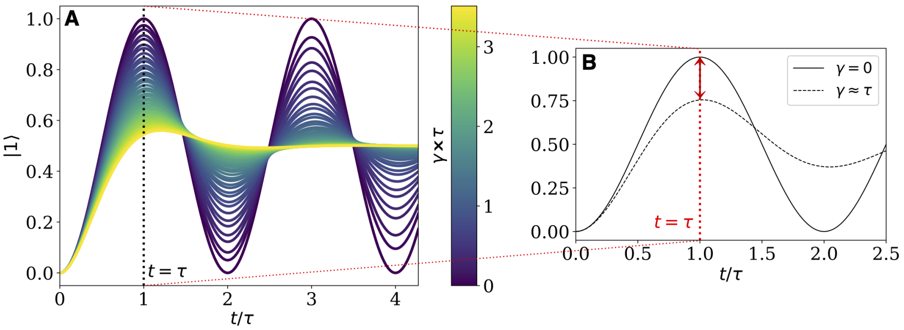

Figure 2-4: Effect of the bath interaction in the dynamics of the excitonic system simulating the NOT gate. (A) Population dynamics of the $|1\rangle$ state for different dephasing ratios, $\gamma \times \tau$. The x axis corresponds to time as a fraction of the time it takes to complete the first transformation. (B) Schematic of the definition used for quantum fidelity. The fidelity measures how much the excitonic open system dynamics differ from those of the closed system at $t = \tau$ (red dotted line).

of a pure state density matrix $\mathrm{Tr}\{\rho^2_{\mathrm{closed}}\} = 1$ [15]. The last term, $\sin^2\theta_{ij}$, describes the ability of the polarization addressing scheme to distinguish between a pair of dyes when the system is measured. This gives a vanishing fidelity for parallel and anti-parallel dyes (i.e. $\theta_{ij} = 0, \pi$) since the two dyes cannot be distinguished by a polarized pulse in these configurations.

Equipped with this measure of circuit performance, we now consider the required parameter regime for a reliable implementation of two-dimensional unitary transformations. To illustrate the effect of dissipation and dephasing on the fidelity of a NOT gate circuit, we use as an example a pair of nearly-orthogonal Cy3 dyes scaffolded in adjacent nucleotide bases [93]: $r_{ij}/\mu \approx 0.27$Å/D, $\theta_{ij} = 4\pi/9$ and $\varphi = \pi/2$. The effect is shown in Fig. 2-5A.

As expected from the dynamics shown in Fig. 2-4A, the Fidelity of the gate exponentially decays with increasing dephasing and dissipation rates before approaching a 50-50 incoherent mixture of the two states. This yields a fidelity of 0.5 indicating that the correct answer is obtained with the same probability as randomly selecting the output. This corresponds to a circuit that has entirely failed to mimic any unitary transformation. Similarly to the NOT gate, the performance of the Hadamard gate is determined by the computation time scale τ relative to the bath-induced relaxation time. It can be shown that the same behavior in Fig. 2-5 can be observed in a

Hadamard circuit.

When $(\Gamma + \gamma)\tau > 1$, the system has lost its coherence before the gate operation is completed for the first time. Consequently, an excitonic NOT and Hadamard gate will perform well if the computation time, τ, is less than both the dephasing and dissipation times, this is, below the limit $(\Gamma + \gamma)\tau < 1$ (red dashed line in Fig. 2-5A).

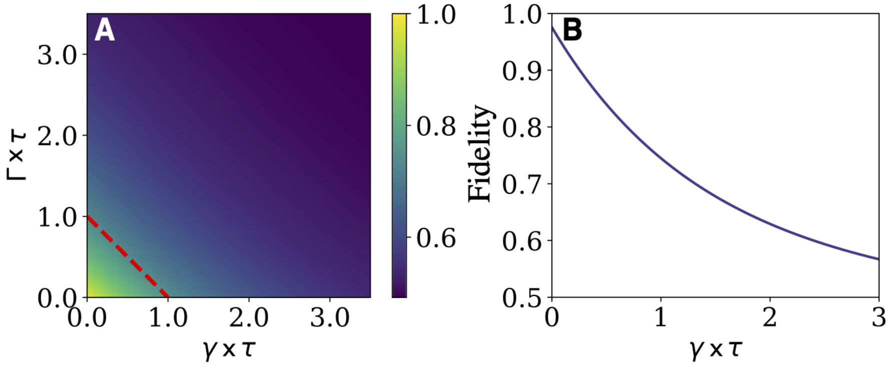

Figure 2-5: Fidelity of the NOT gate under environmental noise. (A) Fidelity as a function of dephasing and dissipation effects as ratios of the computation time, τ. Above $\Gamma + \gamma = 1/\tau$, the system will lose dynamics faster than the time it takes the first gate transformation to be completed (red dashed line). (B) Fidelity as a function of the dephasing as $\gamma \times \tau$.

Using these observations, it is possible to establish specific bounds on the potential dye systems that can be employed to map a one-qubit unitary transformation. Because these transformations can only be reliably realized if they are completed before bath-induced relaxation, $(\Gamma + \gamma) < 1/\tau$ (red dotted line in Fig. 2-5) imposes an upper boundary on the allowable computation time. Furthermore, the transformation time, τ, depends on the strength of the coupling (e.g. $\tau = \pi/(2V_{01})$ for the NOT gate). If the dyes can be placed no closer than some distance $r_{\min}$, and the orientation of the dyes is set to maximize the coupling from Eq. 2.1 (*i.e.*, $\theta_{ij} = \pi/2$ and $\varphi = 0$), the coupling is bounded by the expression $|V_{01}| \leq |\mu_A||\mu_B|/4\pi^2\epsilon_0 r_{\min}^3$. Using these considerations, we propose the following criteria promising excitonic circuits:

$$\left|\frac{(\Gamma + \gamma)}{\mu_{\mathrm{A}}\mu_{\mathrm{B}}}\right| < \frac{1}{\pi^2 \varepsilon_0 r_{\min}^3}, \tag{2.8}$$

where the choice of $r_{\min}$ depends on the choice of supermolecular support structure for the dye pairs. For example, for a system of dyes embedded in DNA, the individual dyes cannot be placed closer than a DNA base-pair, so we have $r_{\min} \approx 3.4\text{Å}$. For dye pairs in a polypeptide chain, $r_{\min}$ is determined by the peptide size, which is typically 1.32Å. [13].

Optimizing circuit geometry.

We now consider optimizing the geometry of excitonic circuits to maximize their Fidelity. Due to the flexibility of the constraints imposed by the unitary transformations, many configurations can reproduce the same gate. However, these will generally differ in their computation time and therefore, their sensitivity to environmental noise. For the NOT gate, this time scale is entirely determined by the coupling between the dyes. For simplicity, we will restrict our attention to homodimers with identical dyes since this is the most likely method of achieving degenerate excited states.

In this case, $\mu_A = \mu_B$ and the coupling V_{01} and, consequently, the fidelity will be a function of only the spatial arrangement of the molecular system. We describe the exciton geometry via three parameters: the twist angle, θ_{ij}, the center-to-center intermolecular distance, r_{ij}, and the angle between the dyes and the distance vector, φ, which we assume to be identical for each dye. In realistic systems, the bath contribution is expected to be dominated by the dephasing contribution. As such, we have restricted our attention to purely dephasing baths (*i.e.* $\Gamma = 0$) with a fixed slow dephasing rate $\gamma \times \tau_{\mathrm{f}} = 0.8$. The parameter τ_{f} is calculated from the electronic coupling between a pair of nearly-orthogonal Cy3 dyes at base-pair distance, as in the previous section. This dephasing rate was selected to more clearly show the geometry dependence of the fidelity and is likely to be significantly higher in realistic systems.

We first consider a pair of dyes comprising a NOT gate which are displaced perpendicular to their dipole moments (i.e. $\varphi = \pi/2$), which sets the second term in Eq. 2.1 to zero. Fig. 2-6A shows the dependence of the fidelity of the NOT gate on the spatial terms, r_{ij} and θ_{ij}. Note that the intermolecular distance is presented as a ratio of the transition dipole moment magnitude, μ, in Å/D units, with $\mu = 12\text{D}$ corresponding to a Cy3 homodimer.

Some interesting patterns in the behavior of the fidelity should be highlighted in

Fig. 2-6A. We first note two regions where the fidelity is zero for all intermolecular distances: when $\theta_{ij} = \pi/2$ and $0, \pi$. In the first case, the dyes are orthogonal to each other, leading to vanishing coupling for all r_{ij}. The dye geometry is therefore incapable of satisfying the coupling constraints imposed by the NOT gate transformation. The second case corresponds to a dimer of parallel or antiparallel dyes. In this case, the dyes can not be distinguished by the polarization addressing scheme. As a result, Eq. 2.7 results in a fidelity of zero when $\theta_{ij} = 0, \pi$, for all values of r_{ij}. Overall, the dependence of the fidelity on the interchromophore angle, θ_{ij}, demonstrates a trade-off between the $\cos\theta_{ij}$ and $\sin^2\theta_{ij}$ terms, with a maximum fidelity at a critical point close to $\theta_{ij} = \pi/2$, as evident in Fig. 2-6A.

The effect of the interchromophore distance, r_{ij}, on the fidelity is contained in the term $1/r_{ij}^3$ in Eq. 2.1. As a result, we see that the coupling and the fidelity monotonically decrease with increasing distance between the dyes. In this case, the optimal geometry simply minimizes distance subject to experimental constraints.

A more complete picture of geometry arrangement emerges when φ is allowed to change. Fig. 2-6B presents the behavior of the fidelity when θ_{ij} and φ are varied at a fixed ratio of $0.21e \times r_{ij}/\mu = 1.29$ and the same bath conditions as panel A. In this case, the coupling contains contributions from the second term in Eq. 2.1, allowing for $V_{01} \neq 0$ when $\theta_{ij} = \pi/2$. As a result, the maximum fidelity can now be reached with orthogonal dyes as this circumvents the trade-off between coupling and measurement specificity inherent to the $\varphi = \pi/2$ case treated above. Similarly to Fig. 2-6A, a sharp line can be seen with rapidly decreasing fidelity where the dyes are uncoupled. Since the coupling depends on both angles, this is no longer a straight line and instead appears as the curved line in Fig. 2-6B given by $\mu_A \cdot \mu_B = 3(\mu_A \cdot \hat{r}_{ij})(\mu_B \cdot \hat{r}_{ij})$.

In this chapter, we have proposed a general strategy for mapping specific unitary operations onto excitonic circuits. Although this strategy is limited in complexity small quantum systems, these systems exhibit a manifold of possible excitonic circuits that are able to generate them. This excess degrees of freedom can be exploited to facilitate experimental initialization and measurement and to mitigate the effect of environmental noise. In the next chapter, I will explore unitary operations of increased

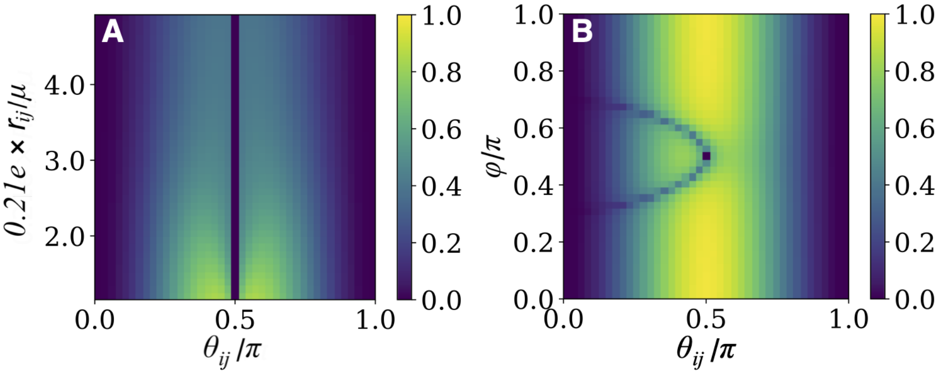

Figure 2-6: Fidelity of the NOT quantum gate for different spatial distributions of the dye-pair coordinate system.(A) Fidelity as a function of the dimensionless ratio of the inter-chromophore distance and transition dipole magnitude, $0.21e \times r_{ij}/\mu$, and angle, θ_{ij}, when both dyes are orthogonal to the z axis, and (B) as a function of θ_{ij} and φ, the angle between both dyes and the distance vector, $\mathbf{\hat{r}_{ij}}$.

complexity, using a simple 2-qubit quantum algorithm as an example. Moreover, I will introduce an atomistic model for the bath, that will replace the *toy model* employed in the present chapter.

Chapter 3

Modeling Thermodynamic Bath Effects in Exciton-Mapped Quantum Algorithms

3.1 Introduction

One potential application of excitonic circuitry is quantum computing. Excitons carry information about quantum phase, coherence, and entanglement that can be systematically manipulated within appropriately designed systems [76, 17, 75, 38, 138]. These quantum dynamical properties can be tuned to encode specific quantum transformations, or sequences of transformations. However, as seen in the previous chapter, optimization of a circuit for mapping unitary operations is challenging due to ambiguity in design strategy, as there are generally numerous different circuit geometries capable of performing a given computation. In this Chapter, I will compare two different strategies for designing excitonic circuits that carry out a simple 2-qubit algorithm. We find that the strategy of hard-coding the entire algorithm into a single circuit has the potential to yield significantly higher fidelity than a modular strategy, for which the algorithm is implemented as a sequence of universal quantum gate operations. This finding thus exposes significant practical barriers to the use of excitonic circuits for more complicated quantum algorithms, *e.g.*, requiring more than two qubits or many steps.

This Chapter will extend the mapping of unitary quantum gates to the design of a simple multi-step 2-qubit quantum algorithm—the 2-qubit Deutsch-Jozsa algorithm—where there are multiple approaches to circuit design. Our results highlight that computational fidelity can depend significantly on the chosen design strategy.

In the next section, I will review the Deutsch-Jozsa algorithm. Then, in Sec. 3.3, I describe how this algorithm can be implemented with excitonic circuits using two different design strategies—serial and combined. In Sec. 3.4 I evaluate the fidelity of these hypothetical circuits under the influence of a harmonic bath. Finally, in Sec. 3.5 I propose a specific atomistic realization of these circuits and evaluate the circuit performance with a more realistic bath model.

3.2 The Deutsch-Jozsa Algorithm

The Deutsch-Jozsa (D-J) algorithm is one of the simplest algorithms for which a quantum computer outperforms a classical one [44]. The algorithm distinguishes the identity of a black-box 'oracle gate' that transforms an input binary array of n bits, *e.g.*, $(0,1,1,0,\cdots,1)$ to a single binary output value, *i.e.*, 0 or 1. The two possible identities of this oracle gate are 'constant', in which the output is always the same (*i.e.*, always 1 or always 0, regardless of the input), and 'balanced', in which the output is 0 for half of the input states and 1 for the other half. To unambiguously determine the identity of an unknown oracle gate requires multiple queries with classical computation (at least $2^{n-1}+1$), but only requires a single query with quantum computation [36]. This algorithm has been implemented in several physical systems, such as nuclear spins [34], ion traps [70], and superconductors [46] as a way to demonstrate their feasibility as potential quantum computing platforms.

Figure 3-1A depicts the quantum circuit diagram for identifying a $n = 1$ oracle gate, f. The quantum algorithm, which requires two qubits, involves performing Hadamard operations carried out on one or both qubits after and before evaluating the oracle gate. Specifically, the first set of Hadamard operations transform the input state, $|\Psi\rangle_i = |0\rangle|1\rangle$ into a superposition state, *i.e.*, $|\Psi\rangle_1 = |+\rangle|-\rangle$, where $|\pm\rangle = (|0\rangle \pm |1\rangle)/\sqrt{2}$. The action of the oracle gate is to perform a *phase kick-back* operation on the second qubit, $U_f : |x\rangle|y\rangle \rightarrow |x\rangle|y \oplus f(x)\rangle = (-1)^{f(x)}|x\rangle|y\rangle$. When $N = 2$, $f(x)$ can take 1 of 4 possible values: $f(x) = 0$ or $f(x) = 1$, when constant, and $f(x) = x$ or $f(x) = \mathrm{NOT}x$, when balanced. After the third step, the final state of the qubit register will then be $|\Psi\rangle_F = \pm|0\rangle|-\rangle$ or $|\Psi\rangle_F = \pm|1\rangle|-\rangle$ if the oracle gate is constant or balanced, respectively. A single measurement over the ancilla qubit (*i.e.* qubit 1) at the conclusion of the algorithm therefore reveals the identity of the “black box" oracle function.

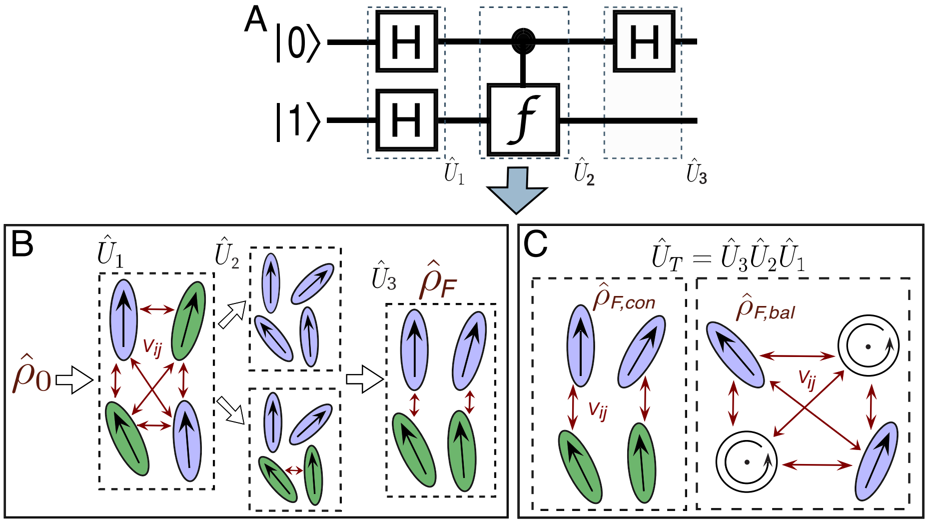

Figure 3-1: Encoding the Deutsch-Jozsa algorithm into the evolution of excitonic circuits. (A) Quantum circuit diagram representing the Deutsch-Jozsa algorithm. (B) Schematic representation of the 2-qubit excitonic circuit geometry for the serial strategy. This circuit transforms an input exciton state, ρ_0, into an output state, ρ_{F}, via three steps. Dye molecules are represented by ovals and the molecular species is indicated by shading. Non-zero coupling is indicated by red arrows. The top and bottom branches in the middle step correspond to the constant and balanced cases, respectively. (C) Schematic excitonic circuit geometry for the combined strategy for the constant (left) and balanced (right) algorithms. The balanced algorithm includes dye molecules (circles) that are excited via circularly polarized photons.

3.3 Implementing the Deutsch-Jozsa Algorithm with Excitonic Circuits

In this section we describe two general strategies for representing a simple quantum algorithm as an excitonic circuit of precisely arranged dye molecules. The first is a *serial* strategy, where each quantum gate operation is carried out sequentially. The second is a *combined* strategy, where the entire algorithm is carried out by a single circuit.

Mapping the D-J algorithm onto the Frenkel Hamiltonian.

We propose excitonic circuits for the D-J algorithm following the procedure described in Chapter 2 and Ref. [27]. Following Eq. 2.3, our approach to excitonic circuit design for an n-qubit quantum computation maps the $N \times N$ unitary operator for the computation, where $N = 2^n$, to the Frenkel Hamiltonian of a system of N dye molecules, $\hat{\mathcal{H}}_{\text{comp}}$. There are many possible strategies for designing an excitonic circuit for the multi-step D-J algorithm. For instance, the algorithm can be equivalently represented by either a sequence of three 2-qubit unitary operations (*i.e.*, $\hat{U}_1$, then $\hat{U}_2$, then $\hat{U}_3$), one for each step in the circuit diagram of Fig. 3-1A, or a single unitary operation that combines all three steps (*i.e.*, $\hat{U}_{\text{prod}} = \hat{U}_3\hat{U}_2\hat{U}_1$). These two limiting strategies, as illustrated in Figs. 3-1B and C, yield either four distinct circuits in the serial case (one for each of the first and third steps and one for each of the balanced and constant oracle gates) or two distinct circuits in the combined case (one for the balanced case and one for the constant case). The unitary operators and corresponding system Frenkel Hamiltonians for the serial and combined strategies of excitonic circuit design are contained in Table 1, as derived from Eq. 2.3.

A serial implementation of the D-J algorithm requires a coordinated series of exciton evolutions and transfers between different circuits. First, a specific exciton state is initialized on a system described by $\hat{\mathcal{H}}_1$, for instance through laser excitation. The exciton is then evolved for time τ_1 followed by a transfer of the resulting exciton state to a system described by $\hat{\mathcal{H}}_2$. The exciton is then evolved for time τ_2 and transferred to the system described by $\hat{\mathcal{H}}_3$. The exciton is then allowed to evolve

Table 3.1: The unitary transformations corresponding to the universal quantum logic gates and the corresponding system Hamiltonians as mapped. All Hamiltonian couplings are presented relative to the difference in excitation energy between a pair of dyes, $\Delta\varepsilon_{\alpha\beta} = \varepsilon_\alpha - \varepsilon_\beta$

Operation	Unitary operator	Hamiltonian
First step	$\hat{U}_1 = \frac{1}{2}\begin{pmatrix} 1 & 1 & 1 & 1 \\ 1 & -1 & 1 & -1 \\ 1 & 1 & -1 & -1 \\ 1 & -1 & -1 & 1 \end{pmatrix}$	$\hat{\mathcal{H}}_1 = \frac{\pi\hbar}{4\tau_1}\begin{pmatrix} \varepsilon_\alpha & \Delta\epsilon_{\alpha\beta}/2 & \Delta\epsilon_{\alpha\beta}/2 & \Delta\epsilon_{\alpha\beta}/2 \\ \Delta\epsilon_{\alpha\beta}/2 & \varepsilon_\beta & \Delta\epsilon_{\alpha\beta}/2 & -\Delta\epsilon_{\alpha\beta}/2 \\ \Delta\epsilon_{\alpha\beta}/2 & \Delta\epsilon_{\alpha\beta}/2 & \varepsilon_\beta & -\Delta\epsilon_{\alpha\beta}/2 \\ \Delta\epsilon_{\alpha\beta}/2 & -\Delta\epsilon_{\alpha\beta}/2 & -\Delta\epsilon_{\alpha\beta}/2 & \varepsilon_\alpha \end{pmatrix}$
Oracle	$\hat{U}_2^{\text{con}} = \begin{pmatrix} 1 & 0 & 0 & 0 \\ 0 & 1 & 0 & 0 \\ 0 & 0 & 1 & 0 \\ 0 & 0 & 0 & 1 \end{pmatrix}$	$\hat{\mathcal{H}}_2^{\text{con}} = \begin{pmatrix} \varepsilon_\alpha & 0 & 0 & 0 \\ 0 & \varepsilon_\alpha & 0 & 0 \\ 0 & 0 & \varepsilon_\alpha & 0 \\ 0 & 0 & 0 & \varepsilon_\alpha \end{pmatrix}$
	$\hat{U}_2^{\text{bal}} = \begin{pmatrix} 1 & 0 & 0 & 0 \\ 0 & 1 & 0 & 0 \\ 0 & 0 & 0 & 1 \\ 0 & 0 & 1 & 0 \end{pmatrix}$	$\hat{\mathcal{H}}_2^{\text{bal}} = \frac{\pi\hbar}{2\tau_2^b}\begin{pmatrix} \varepsilon_\alpha & 0 & 0 & 0 \\ 0 & \varepsilon_\alpha & 0 & 0 \\ 0 & 0 & \varepsilon_\beta & \Delta\varepsilon_{\alpha\beta} \\ 0 & 0 & \Delta\varepsilon_{\alpha\beta} & \varepsilon_\beta \end{pmatrix}$
Third step	$\hat{U}_3 = \frac{1}{\sqrt{2}}\begin{pmatrix} 1 & 0 & 1 & 0 \\ 0 & 1 & 0 & 1 \\ 1 & 0 & -1 & 0 \\ 0 & 1 & 0 & -1 \end{pmatrix}$	$\hat{\mathcal{H}}_3 = \frac{\pi\hbar}{4\tau_3}\begin{pmatrix} \varepsilon_\alpha & 0 & \Delta\varepsilon_{\alpha\beta}/2 & 0 \\ 0 & \varepsilon_\alpha & 0 & \Delta\varepsilon_{\alpha\beta}/2 \\ \Delta\varepsilon_{\alpha\beta}/2 & 0 & \varepsilon_\beta & 0 \\ 0 & \Delta\varepsilon_{\alpha\beta}/2 & 0 & \varepsilon_\beta \end{pmatrix}$
Combined, constant	$\hat{U}_{\text{prod}}^{\text{con}} = \frac{1}{\sqrt{2}}\begin{pmatrix} 1 & 1 & 0 & 0 \\ 1 & -1 & 0 & 0 \\ 0 & 0 & 1 & 1 \\ 0 & 0 & 1 & -1 \end{pmatrix}$	$\hat{\mathcal{H}}_{\text{prod}}^{\text{con}} = \frac{\pi\hbar}{4\tau_{con}}\begin{pmatrix} \varepsilon_\alpha & \Delta\varepsilon_{\alpha\beta}/2 & 0 & 0 \\ \Delta\varepsilon_{\alpha\beta}/2 & \varepsilon_\beta & 0 & 0 \\ 0 & 0 & \varepsilon_\alpha & \Delta\varepsilon_{\alpha\beta}/2 \\ 0 & 0 & \Delta\varepsilon_{\alpha\beta}/2 & \varepsilon_\beta \end{pmatrix}$
Combined, balanced	$\hat{U}_{\text{prod}}^{\text{bal}} = \frac{1}{\sqrt{2}}\begin{pmatrix} 1 & 0 & 0 & 1 \\ 1 & 0 & 0 & -1 \\ 0 & 1 & 1 & 0 \\ 0 & -1 & 1 & 0 \end{pmatrix}$	$\hat{\mathcal{H}}_{\text{prod}}^{\text{bal}} = \frac{\pi\hbar}{8\tau_{bal}}\begin{pmatrix} \varepsilon_\alpha & \frac{\Delta\varepsilon_{\alpha\beta}}{4}(2+\sqrt{2}i) & \frac{\Delta\varepsilon_{\alpha\beta}}{2}(1-\sqrt{2}) & \frac{\Delta\varepsilon_{\alpha\beta}}{4}(2-\sqrt{2}i) \\ \frac{\Delta\varepsilon_{\alpha\beta}}{4}(2-\sqrt{2}i) & \varepsilon_\beta & \frac{\Delta\varepsilon_{\alpha\beta}}{4}(2+\sqrt{2}i) & -\frac{\Delta\varepsilon_{\alpha\beta}}{2}(1+\sqrt{2}) \\ \frac{\Delta\varepsilon_{\alpha\beta}}{2}(1-\sqrt{2}) & \frac{\Delta\varepsilon_{\alpha\beta}}{4}(2-\sqrt{2}i) & \varepsilon_\alpha & \frac{\Delta\varepsilon_{\alpha\beta}}{4}(2+\sqrt{2}i) \\ \frac{\Delta\varepsilon_{\alpha\beta}}{4}(2+\sqrt{2}i) & -\frac{\Delta\varepsilon_{\alpha\beta}}{2}(1+\sqrt{2}) & \frac{\Delta\varepsilon_{\alpha\beta}}{4}(2-\sqrt{2}i) & \varepsilon_\beta \end{pmatrix}$

for time τ_3 on system 3 before it is read out, for instance through photon emission. Admittedly, achieving and coordinating these steps would require a heroic feat that we lack current technology to achieve. Nonetheless, for the sake of analysis, we assume here that initialization, exciton transfer, and detection all occur without error and with 100% fidelity.

On the other hand, the combined strategy utilizes a single excitonic circuit to execute the action of the combined unitary operators $\hat{U}^{\text{con}}_{\text{prod}} = \hat{U}_3 \hat{U}_2^{\text{con}} \hat{U}_1$ and $\hat{U}^{\text{bal}}_{\text{prod}} = \hat{U}_3 \hat{U}_2^{\text{bal}} \hat{U}_1$, thereby eliminating the need to transfer exciton states between multiple separate circuits. The excitonic circuit implied by $\hat{\mathcal{H}}^{\text{con}}_{\text{prod}}$ is an uncoupled pair of coupled heterodimers. Notably, this circuit is effectively identical to that of the circuit for $\hat{\mathcal{H}}_3$. This similarity implies that the specific operation of the constant oracle operator is essentially trivial and simply drops out of the combined unitary operator, leading to a significant simplification of the resulting excitonic circuit.

The excitonic circuit is implied by two pairs of homodimers, with all dyes coupled to each other. Notably, the system features imaginary-valued couplings. Imaginary coupling can occur between two dyes if each one is electronically excited using a different polarization of light. For example, if one dye is initialized using linearly polarized light with unequal x-y amplitudes and the other dye is excited with circularly polarized light. I will delve deeper into the idea of imaginary coupling in the following chapter.

3.4 Simulating the Performance of Idealized Excitonic Circuits in Model Environments

The Hamiltonians in Table 1 represent idealized systems that in the absence of an environment (*i.e.*, a closed quantum system) will perform the given computation in time τ with unit fidelity. However, any practical application will include the influence of a noisy environment. In this case, system-bath interactions lead to dephasing and dissipation that can alter the output and thus degrade fidelity.

In this section we simulate the influence of a model environment on the fidelity of idealized D-J excitonic circuits. We compare overall fidelity loss between idealized serial and combined circuits. We assume that serial circuits lose no fidelity between steps. Because fidelity losses due to dissipation are expected to be negligible on the timescales of interest, we only consider the effect of dephasing in the system dynamics. We also assume that the input state of the wavefunction can be precisely prepared and the output state can be precisely detected at time τ. With these assumptions, we can evaluate fundamental differences in fidelity between circuits designed with the serial and combined strategies. We describe the state of the excitonic wavefunction in terms of a reduced density matrix and simulate the evolution of that wavefunction using a Redfield master equation under the secular approximation.

The Redfield equations are defined in terms of time correlation functions of the system-bath coupling, which are given by,

$$\hat{\mathcal{H}}_{S-B} = \sum_{m}^{N} \mathbf{G}_m \sum_{a} c_{m,a} \mathbf{Q}_{m,a}, \tag{3.1}$$

where $\mathbf{G}_m$ represents the electronic state of the mth dye molecule and the coefficients $c_{m,a}$ describe the distribution of the system-bath coupling across the different bath modes. Specifically, we define $\mathbf{G}_m$ using a Linbladian operator with diagonal elements,

$$\mathbf{G}_m = \sqrt{\frac{\gamma_m}{2}} \left| m \right\rangle \left\langle m \right|, \tag{3.2}$$

where γ_m is the dephasing rate of the mth dye. The phonon modes coordinates enter the Redfield equation through time-correlation functions of the form,

$$\begin{aligned} \chi_m(t) = \sum_a c_{m,a}^2 \langle \mathbf{Q}_{m,a}(t) \mathbf{Q}_{m,a}(0) \rangle \\ = \frac{\hbar}{\pi} \int_0^\infty d\omega J(\omega) \left[\coth\left(\beta\hbar\omega/2\right) \cos\omega t - i \sin\omega t\right], \end{aligned} \tag{3.3}$$

where $\chi_m(t)$ is calculated for each local bath m, $\beta = 1/k_B T$ and $J(\omega)$ is the spectral density. For this section, $J(\omega)$ is taken to be a Ohmic spectral density with a Lorentzian cutoff,[19]

$$J(\omega) = 2\lambda\Omega_c \frac{\omega}{\omega + \Omega_c^2}, \tag{3.4}$$

where λ is the reorganization energy of the bath and Ω_c the cutoff frequency.

We choose bath parameters to model a condensed phase chromophoric system at 300K. From Ref. [81], we set $\lambda = 100$ cm$^{-1} \approx 0.012$ eV and Ω_c to be proportional to λ by $2\lambda/(\beta\Omega_c^2) = 1.2$ [113]. The dephasing time, $t_D = 1/\gamma$, was chosen to be $(3/4)\tau$ for all dyes in a given circuit, where τ is the transformation time for the mapped operation. We parameterize the dye molecules in our circuit based on Cy3-oxypropyl and Cy5-oxypropyl molecules. Specifically, we always assume that dye A is a Cy3 species with excitation energy $\varepsilon_\alpha = 3.24$ eV. In circuits that require two dye species (*i.e.*, A and B), we assume the B dye species is Cy5 with $\varepsilon_\beta = 2.85$ eV. These values reflect the first excited state energies as computed from time-dependent density functional theory (TDDFT) with a 6-31G+(d) basis set and WB97XD DFT functional.

The resulting dynamics for the four studied systems, namely, the serial and combined excitonic circuits, both for the constant and balanced versions of the algorithm, are shown in Fig. 3-2. The influence of system-bath interactions on the fidelity of a given computation is encoded in the structure and evolution of the reduced density matrix, $\hat{\rho}$. This influence can be illustrated by tracking a single element of $\hat{\rho}$ in both a closed and open system. In Fig. 3-2A, we plot the exciton population on dye **C** throughout the sequence of transformations described for the serial D-J algorithm in its constant version, namely $\hat{\mathcal{H}}_1$, $\hat{\mathcal{H}}_2^{\text{con}}$ and $\hat{\mathcal{H}}_3$, while Fig. 3-2B depicts the dynamics for the balanced version. We focus on this dye molecule because its final population indicates the identity of the oracle gate. Moreover, these populations are presented as segmented plots, in order to illustrate how the populations are transferred sequentially through the algorithm, at each transformation time. The full population dynamics for the individual circuits can be found in Fig. B-1 in the Appendix B.

Phase loss in the open system (solid lines in Fig. 3-2) results in a decrease in fidelity that grows with time. In the serial system, shown in Figs. 3-2A and B, phase loss accumulates with each subsequent step. It can be seen that dephasing is most

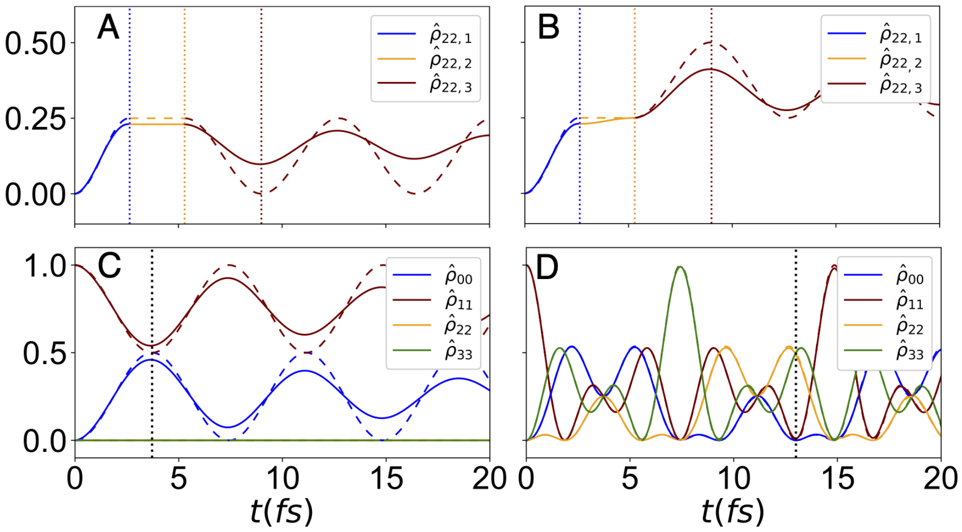

Figure 3-2: Time-evolution of the populations of the D-J algorithm with a model environment. The population for the Cy3 (C) dye as the wavefunction evolves through the first, second and last step, for (A) the constant and (B) balanced version. The segmented dynamics illustrate the transference of populations to subsequent steps, when the transformation time is reached (vertical dotted lines). The populations for all four dyes for the single-step in the combined approach, for (C) the constant and (D) the balanced version. Here, τ is indicated with a black dotted line. The populations for the closed system are shown in dashed lines on each plot. For the combined constant version, note that $\hat{\rho}_{22}$ and $\hat{\rho}_{33}$ are both constant in zero.

significant in the final step of the algorithm in both serial systems. Indeed, the details of the system Hamiltonian set the dephasing rates for each different excitonic circuit.

In contrast, the combined systems, shown in Figs. 3-2C and D, require only a single step. In the constant system (Fig. 3-2C) the system maintains high fidelity despite being prone to dephasing due to the short computation time, $\tau_{\text{con}} \approx 4\text{fs}$. Notably, the balanced system requires a much longer computation time ($\tau_{\text{bal}} \approx 13\text{fs}$) yet features negligible fidelity loss. This observation implies that some circuits retain fidelity much better than others and that design efforts may require a trade-off between circuit complexity and fidelity retention.

In order to quantify how much of the information contained in the final quantum state is lost due to fluctuations in the bath, we use a modified form of the fidelity defined in Eq. 2.7,

$$F(t) = Tr\sqrt{\hat{\rho}^{(\text{op})}(t)^{1/2}\hat{\rho}^{(\text{cl})}(t)\hat{\rho}^{(\text{op})}(t)^{1/2}}, \tag{3.5}$$

which measures the similarity between the closed system density matrix at time t, $\hat{\rho}^{(cl)}(t)$, and that of the open system under pre-defined environmental conditions, $\hat{\rho}^{(op)}(t)$. To account for uncertainty in the measurement associated with any possible experimental set-up to be used to read the final state, we assume $\hat{\rho}^{(op)}$ cannot possibly be measured exactly at t and, thus, we randomly choose a time t_m from the range $t_m \in \{t - \Delta t, t + \Delta t\}$, where Δt is the uncertainty in the measurement (here chosen to be $\Delta t = 0.2$fs), and average over the total number of observations, M:

$$\bar{F}(t_m) = \frac{1}{M} \sum_{m}^{M} Tr \sqrt{\hat{\rho}^{(\mathrm{op})}(t_m)^{1/2} \hat{\rho}^{(\mathrm{cl})}(t_m) \hat{\rho}^{(\mathrm{op})}(t_m)^{1/2}}. \tag{3.6}$$

We use this equation to compute the fidelity of the open D-J excitonic circuits. Under a serial approach, the fidelity decreases as $\bar{F}(\tau_1) = 0.93 \rightarrow \bar{F}(\tau_2^{\mathrm{c}}) = 0.74 \rightarrow \bar{F}(\tau_3) = 0.65$ (with τ_2^{c} set to 2fs), and $\bar{F}(\tau_1) = 0.93 \rightarrow \bar{F}(\tau_2^{\mathrm{b}}) = 0.79 \rightarrow \bar{F}(\tau_3) = 0.69$, from the first to the third step of the algorithm, for the constant and balanced D-J, respectively. That is, the fidelity decreases consistently with each step, such that there is significant uncertainty in the identity of the oracle function upon measurement on the state $\hat{\rho}_3(\tau)$. On the other hand, the calculated fidelities for the combined approach are significantly higher, $\bar{F}(\tau_{\mathrm{con}}) = 0.96$ and $\bar{F}(\tau_{\mathrm{bal}}) = 0.97$. Notably, the lower fidelities of the serial circuits do not include the effects of fidelity loss in the transfer of excitons from one circuit to the next. We thus speculate that the combined strategy for excitonic circuit design yields calculations with much higher fidelity than a serial strategy.

The difference in fidelity between the two strategies can be observed more clearly by comparing $\bar{\mathrm{F}}$ as a function of time for the combined and serial approach, as shown in Fig. 3-3. These results highlight that fidelity loss rates differ between steps in the serial circuits and that certain steps can dominate overall fidelity loss. For both cases considered here, the second step (associated with the action of the oracle gates) is the most significant source of fidelity loss. These results also highlight that fidelity loss rates are significantly lower for the combined strategy than for the serial strategy. These differences reflect the benefit of lowering the total computational time, thereby reducing system-bath interactions, but also reveal that some circuits are fundamentally better at retaining exciton phase information than others.

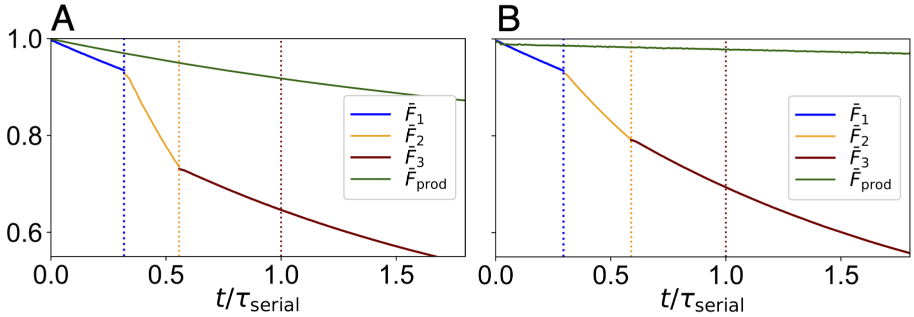

Figure 3-3: Fidelity of the serial and combined approaches as a function of time, for (A) the constant and (B) balanced circuits, respectively. Transformation times τ_1, $\tau_1 + \tau_2$ and $\tau_1 + \tau_2 + \tau_3 = \tau_{\mathrm{serial}}$ are indicated by blue, orange and red dotted lines, respectively. In both panels, the time axis is scaled to the total computational time of the serial approach. For the constant case $\tau_{\mathrm{serial}} = 8.4\mathrm{fs}$ and $\tau_{\mathrm{prod}} = 3.7\mathrm{fs}$. For the balanced case $\tau_{\mathrm{serial}} = 9.0\mathrm{fs}$ and $\tau_{\mathrm{prod}} = 13.0\mathrm{fs}$.

3.5 Designing Explicit Molecular Representations of Excitonic Circuits

The systems implied by the idealized Hamiltonians of Table 1 are hypothetical in that they ignore the potential for steric clashes and geometric frustration that may arise in a physical multi-dye system. Thus, in this section we construct D-J excitonic circuits by arranging four explicit dye molecules in space and we evaluate the performance of the resulting circuits.

We design an excitonic circuit constructed from all-atom representations of Cy3 and Cy5 dyes. Cyanine dyes are often used in synthetic dye-based systems due to their photostability, high fluorescence efficiency, low Stokes shift, commercial availability, and compatibility with common experimental set-ups [93, 99].

We narrow our focus to the constant version of the D-J algorithm, noting that qualitative differences in fidelity between the combined and serial approaches are expected to hold in general. This choice provides simplicity in both the form of the Hamiltonian for the constant oracle operator, a scaled identity operator, and the fact that $\hat{H}^{\mathrm{con}}_{\mathrm{prod}}$ and $\hat{H}_3$ are isomorphic and can thus be carried out on identical circuits.

Our approach is to first identify a geometric arrangement of dye molecules whose interactions approximate a target Frenkel Hamiltonian. We then apply soft constraints to these dye molecules and simulate their dynamics in explicit solvent, using electronic structure calculations to compute bath parameters. With these parameters and the approximate Hamiltonian, we simulate the evolution of the reduced density matrix and analyze the associated computational Fidelity.

Genetic algorithm for the design of excitonic circuits.

In this subsection we describe the development of a genetic algorithm for positioning atomistic representations of dye molecules to yield specific target electronic coupling values. As determined by the Hamiltonians in Table 1 and illustrated in Fig. 3-1, the circuits we aim to create contain two species of dye molecules differing in their excitation energies. The specific dyes that are chosen will set the value of ϵ_1 and ϵ_2 and therefore determine the magnitude of coupling that is required to enable the computation (*i.e.*, off-diagonal elements in $\hat{\mathcal{H}}$). Coupling is a sensitive function of intermolecular separation and orientation so there are, in principle, numerous arrangements of a dye pair that will yield the same coupling value. However, identifying the positioning of a multi-dye system that simultaneously satisfy multiple couplings can be a difficult task.

We undertake this task by performing a search of dye positioning that is biased to favor configurations with a specific set of intermolecular coupling values. For any specific configuration, we compute each value of the intermolecular electronic coupling in an atomistic basis via the point monopole approximation, which has been demonstrated to accurately represent couplings between closely spaced organic dye molecules [30, 54]. Specifically, we define the coupling between molecules i and j as,

$$V_{ij} \approx \sum_{m,n} \frac{q_m^{(i)} q_m^{(j)}}{|\mathbf{r}_m^{(i)} - \mathbf{r}_n^{(j)}|}, \tag{3.7}$$

where $q_m^{(i)}$ is the transition charge density associated with atom m on molecule i in its first excited state, and $\mathbf{r}_m^{(i)}$ denotes the position of that atom. We compute the values of $q_m^{(i)}$ by performing a TDDFT calculation on the molecule in its ground state configuration and localizing the transition density via RESP fitting.

Identifying configurations of a 4-dye system that exhibit the coupling values in a given $\hat{\mathcal{H}}$ requires simultaneously satisfying up to six coupling values. We search for these configurations via a genetic algorithm (GA) as follows: For a given set of dyes (*e.g.,* two pairs of Cy3 and Cy5 dyes) the position of one of the molecules is fixed (*e.g.,* dye A), while the positions of the remaining dyes (*e.g.,* dyes B, C and D) are varied. The GA is designed to find the optimal arrangement of the 3 mobile dyes coordinates such that the system's coupling resembles that of the desired Hamiltonian. Specifically, given the system is initialized such that the center of mass of all 4 molecules is located at the origin, the coordinates of dyes B, C and D are modified by a series of translation-rotation operations of the form,

$$(x_f, y_f, z_f) = R_x(\theta_x)R_y(\theta_y)R_z(\theta_z)\left[(x_0, y_0, z_0) + (d_x, d_y, d_z)\right], \tag{3.8}$$

where the initial configuration of the dye, $\{x_0, y_0, z_0\}$ is first translated by the displacement vector, (d_x, d_y, d_z) and then rotated around its three axis by angles $(\theta_x, \theta_y, \theta_z)$. A chromosome is therefore defined by the displacement and rotation variables for each of the non-fixed dyes (*e.g*, 18 genes in total for the 4-dye system). For each resulting spatial configuration, the intermolecular coupling is calculated between each pair of dyes with Eq. 3.7, and the Hamiltonian of the trial system is constructed. The fitness of each chromosome is determined by comparing the resulting trial Hamiltonian, $\hat{\mathcal{H}}_{i,\text{test}}$, with the desired one, $\hat{\mathcal{H}}_i$ (from Table 3.1),

$$\Gamma_{\text{fit}} = 1 - \left[\frac{1}{2}\text{Tr}\left\{\sqrt{(\hat{\mathcal{H}}_{i,\text{test}}(\tau) - \hat{\mathcal{H}}_i(\tau))^\dagger(\hat{\mathcal{H}}_{i,\text{test}}(\tau) - \hat{\mathcal{H}}_i(\tau))}\right\}\right]. \tag{3.9}$$

We carry out the GA until the fitness function in Eq. 3.9 has been maximized.

For the $\hat{\mathcal{H}}_1$ circuit, the genes comprise the possible rotation and translation operations of Eq. 3.8, keeping one of the Cy3 dyes fixed and imposing a steric constraint that the atoms of any pair of dye molecules be separated by more than 2Å. The GA was run until convergence over a configuration space that includes all dye displacements within a sphere in which $V_{ij} \neq 0$ and all dye rotation angles ranging from $-\pi/2$ to $\pi/2$. Due to the steric constraint and the need for large coupling values

($V \approx 0.1 - 0.2$eV), there is no guarantee of finding a nearly exact solution with this approach. Fig. 3-4B depicts the geometry calculated with this method, which has a fitness of $\Gamma = 75\%$, and a calculated fidelity of $\bar{F} = 82.3\%$.

Finding an optimal geometry for $\hat{\mathcal{H}}_3$ following this recipe is a simple problem, since only a single coupling must be satisfied. Here, only the Cy3-Cy5 pairs will be coupled, and the coupling between the two possible pairs is exactly the same. In fact, due to this simplicity, the circuit can be optimized without the use of the GA. Fig. 3-4A shows the resulting geometric configuration for $\hat{\mathcal{H}}_3$, calculated using the described method. This geometry yields a value of $\Gamma = 99.5\%$.

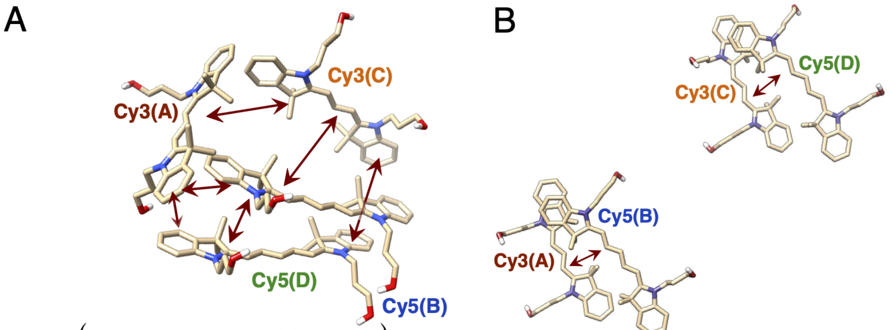

$$\hat{\mathcal{H}}_1 = \frac{\pi\hbar}{4\tau_1}\begin{pmatrix} \varepsilon_{Cy3} & \Delta\varepsilon/4.8 & \Delta\varepsilon/5.5 & \Delta\varepsilon/2.1 \\ \Delta\varepsilon/4.8 & \varepsilon_{Cy5} & \Delta\varepsilon/1.9 & -\Delta\varepsilon/3.6 \\ \Delta\varepsilon/5.5 & \Delta\varepsilon/1.9 & \varepsilon_{Cy5} & -\Delta\varepsilon/7.2 \\ \Delta\varepsilon/2.1 & -\Delta\varepsilon/3.6 & -\Delta\varepsilon/7.2 & \varepsilon_{Cy3} \end{pmatrix}$$

$$\hat{\mathcal{H}}_3 = \frac{\pi\hbar}{4\tau_3}\begin{pmatrix} \varepsilon_{Cy3} & 0 & \Delta\varepsilon/2.2 & 0 \\ 0 & \varepsilon_{Cy3} & 0 & \Delta\varepsilon/2.2 \\ \Delta\varepsilon/2.2 & 0 & \varepsilon_{Cy5} & 0 \\ 0 & \Delta\varepsilon/2.2 & 0 & \varepsilon_{Cy5} \end{pmatrix}$$

Figure 3-4: Schematic of the dye circuits representing the DJ algorithm and corresponding Hamiltonians. (A) For the excitonic circuit found to evolve similarly to $\hat{\mathcal{H}}_1$, and whose spatial distribution was determined using GA, and (B) for the circuit evolving as $\hat{\mathcal{H}}_3$ (and $\hat{\mathcal{H}}_{con}$).

Simulation methodology.

In this subsection, we outline the process for characterizing the system-bath interaction on an explicit dye system. Once the optimal geometry for a specific transformation Hamiltonian is identified, a series of classical and *ab-initio* calculations can be carried out to describe the effect of the bath fluctuations on the system dynamics. This effect can be fully described in terms of the excitation energy autocorrelation function. In the present model only the first excited state is accessible, and therefore the autocorrelation function is calculated for the energy gap from the ground to excited state, ε_{01}. To compute the correlation function, we first use classical MD to generate ground state equilibrium dynamics of the dye system immersed in bulk liquid water at 300K. We then compute the excited state energy, ϵ_{01} for each dye separately at each step of the MD simulation [120, 118, 42, 143]. Finally, we calculate the correlation function,

$$C(t) = \frac{1}{N_t - i} \sum_{k=1}^{N_t - i} \left(\varepsilon_{01}(t'_k) - \langle \varepsilon_{01} \rangle\right) \left(\varepsilon_{01}(t'_{k+i}) - \langle \varepsilon_{01} \rangle\right), \tag{3.10}$$

where t'_i denotes the ith discrete MD timestep, N_t is the total number of steps in the trajectory, $t = \delta t \times i$, and $\delta t = 4\text{fs}$ is the timestep increment in the MD simulations.

We assume each molecule is interacting with its own local bath. Under the Kubo stochastic lineshape theory, the dephasing function, characterizing the exponential decay on the system's phase, can be calculated from the energy gap correlation function [103],

$$D(t) = \exp\left[-\frac{1}{\hbar^2}\int_0^t d\tau (t-\tau) C(t)\right]. \tag{3.11}$$

The dephasing time can likewise be calculated from integration over the dephasing function, $D(t)$,

$$t_D = \frac{2}{\sqrt{\pi}} \int_0^\infty D(t) dt. \tag{3.12}$$

Therefore, following a similar argument as in Sec. 3.4, Equations 3.11 and 3.12 can be used to describe the system operator, $\mathbf{G_m}$, for each one of the four dyes in the circuit, with $\gamma_D = 1/t_D$. Similarly, the energy gap correlation function, $C(t)$, can also be used to derived the frequency-dependent bath contribution to the interaction $\hat{\mathcal{H}}_{S-B}$, contained in the spectral density, $J(\omega)$. We use the following definition,

$$J(\omega) = \frac{2}{\pi\hbar} \tanh\left(\frac{\beta\hbar\omega}{2}\right) \int_0^\infty C(t) \cos(\omega t) dt, \tag{3.13}$$

where a factor $\beta = 1/k_B T$ is added to make sure the spectral density is temperature-independent.

The variation in the energy gap, $\varepsilon_{01}(t_i)$, was estimated along multiple trajectories. In total two sets of simulations were carried out, one for the first step of the D-J algorithm and one for the third step. Each trajectory was generated through a MD simulation on each system, composed of two Cy3-oxypropyl and two Cy5-oxypropyl dyes. The Generalized Amber Force Field (GAFF)[149] was employed to describe the cyanine molecules, and their respective atomic point charges were generated with a restrained electrostatic potential (RESP) fit, using the Q-Chem software [133]. The four cyanine molecules were solvated in a TIP3P water box and Cl^- ions were explicitly added to neutralize the partial positive charge of the dyes. To mimic the scaffolding of the cyanine molecules to a supramolecular structure, constraining the relative positions of the dyes, each molecule was subjected to a small harmonic restrain over the OH end-groups. If connected to a DNA platform, the cyanine dyes would form a bond through this group and, hence, the mechanical constrain on the molecule is concentrated there. Ground-state MD simulations were performed using the Amber18 program [24], with the harmonic constrain on the OH group present throughout the entire simulation.

The energy gap from the ground to first excited state was calculated for each individual cyanine molecule, every 4fs along each MD trajectory. Quantum Chemical calculations were performed using TDDFT with the B3LYP/6-31G level of theory, as included in the PySCF package [141]. The use of more sophisticated basis sets and DFT functionals will result in more accurate absolute values for the excited state energies, but the magnitude of the fluctuations will be virtually the same. A comparison of energy fluctuations calculated with different basis sets and DFT functionals is presented in Fig. S2. The same time-step was employed for every dye in both of the studied circuits, but the length of the QM calculations varied depending on convergence of the correlation function in Eq. 3.10. Here, convergence was said to be reached when C(t) did not seem to visibly change with increasing sampling, and the dephasing function, $D(t)$, showed a purely decaying behaviour for the time-range of interest. The last data points for some calculated autocorrelation functions were not considered within the time range of interest, as C(t) will not be statistically significant for the last few lag points, given the small number of MD trajectories employed. Convergence of the autocorrelation, $C(t)$, was observed to vary significantly between dyes within the same system, supporting the initial assumption that local baths on each dye are fairly independent from each other. Further details on the MD and QM simulations are included in the Appendix B.

Simulating the performance of explicit molecular excitonic circuits.

Using the GA methodology, we generate system Hamiltonians, $\hat{\mathcal{H}}_1$ and $\hat{\mathcal{H}}_3$. We define the system-bath interaction, $\hat{\mathcal{H}}_{\mathrm{S-B}}$, for each dye separately, following Eq. 3.1. The energy gap fluctuations resulting from the interaction of each dye molecule with its local bath, in the systems defined by $\hat{\mathcal{H}}_1$ and $\hat{\mathcal{H}}_3$ are plotted in Figs. 3-5A and B, respectively. In general, the nuclear modes coupling to the electronic transitions of the dye can correspond to either intramolecular vibrations (*i.e.,* arising from the chemical structure of the dye), local intermolecular modes (*i.e.,* from interaction to the other dyes in the system) or from collective motions from the water solvent [114]. These modes affect the system differently depending on the spatial arrangement and chemical nature of the excitonic circuit, and this difference will be reflected in the fluctuation patterns of ε_{01}. The influence of these fluctuations on exciton dynamics can be more conveniently illustrated in terms of the correlation function, $C(t)$, of Eq. 3.10. These correlation functions are plotted in Figs. 3-5C and D.

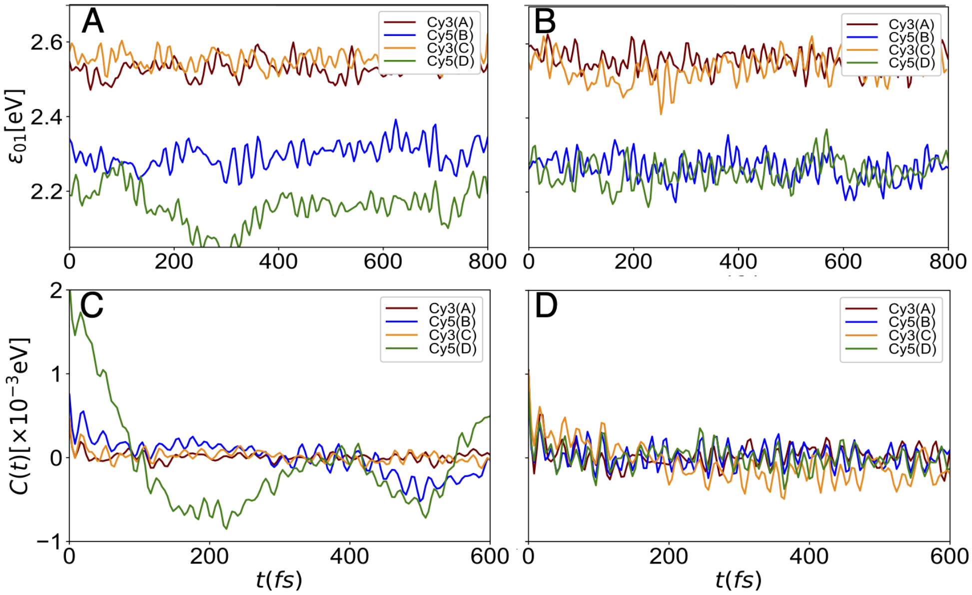

Figure 3-5: Energy gap fluctuations estimated for each one of the four dyes in the circuit corresponding to (A) the first step of the D-J algorithm, $\hat{\mathcal{H}}_1$, and (B) for the third step, $\hat{\mathcal{H}}_3$. Corresponding autocorrelation function for the circuits: (C) $\hat{\mathcal{H}}_1$, and (D) $\hat{\mathcal{H}}_3$.

We find that the short-time behavior of $C(t)$ is fairly similar for all dyes in circuits $\hat{\mathcal{H}}_1$ and $\hat{\mathcal{H}}_3$, with a rapid decay on time scales of about 8 fs. This fast component of the oscillations has a period of $\sim$ 16 fs, for all four dyes in both circuits, but the amplitude of the oscillations and its slow frequency components differ across different dyes and between the circuits. The short-time component in $C(t)$ most likely arises from intramolecular vibrational modes (probably involving the C=C bond), which are expected to be comparable for all dyes, as Cy3 and Cy5 are structurally very similar. However, we can expect the slower frequency components and the long-time decay of the correlation function to differ between dyes, depending on the local environment induced by the intermolecular interactions within each circuit, which are dictated by its spatial arrangement.

We observe that the correlation function for $\hat{\mathcal{H}}_3$ does not seem to vary widely between different dyes, while striking discrepancies are evident between the dyes in $\hat{\mathcal{H}}_1$. This disparity between $\hat{\mathcal{H}}_1$ and $\hat{\mathcal{H}}_3$ arises due to their different spatial dye arrangements. Each cyanine dye in $\hat{\mathcal{H}}_3$ (Fig. 3-4B) interacts with only one other molecule, with each Cy3-Cy5 pair sharing identical interactions. Therefore, the local environment is similar for all dyes, leading to a similar pattern of fluctuations. On the other hand, the geometrical arrangement for $\hat{\mathcal{H}}_1$ is quite different (Fig. 3-4A), since each dye interacts closely with the other dyes in the circuit. Differences in intermolecular interactions manifest as differences in $C(t)$. The most notable difference is the magnitude of $C(t)$ for the Cy5(D) dye, which is more than twice that of the other dyes in the circuit (see insert in Fig. 3-5C), and the presence of large long-time oscillations in the same dye. We quantify the differences in $C(t)$ by fitting each to the following functional form [118],

$$C'(t) = \sum_{i=1}^{N_{exp}=2} a_i e^{-t/\tau_{c,i}} + \sum_{i=1}^{N_{damp}=6} \tilde{a}_i \cos{(\tilde{\omega}_i t)} e^{-t/\tilde{\tau}_{c,i}}, \tag{3.14}$$

This functional form is capable of describing the fast exponential decay (in the first term) and the damped oscillations (in the second term) observed in MD simulations. The value of the correlation at $t = 0$, $C'(0) = \sum_{i=1}^{N_{exp}=2} a_i + \sum_{i=1}^{N_{damp}=6} \tilde{a}_i$, is a direct measure of the magnitude of the average fluctuations, and indicates that Cy5(D) couples more strongly to the bath, compared to the other dyes. Finally, the noticeable long-time oscillations observed in this dye are contained within the first two terms of the damped component of $C'(t)$, $N_{damp} = 1, 2$, but due to the complex environment of these dyes, it is hard to assign these slow oscillations to a particular component of the molecule's normal modes. A complete analysis of the fitted form of $C'(t)$, including the fitted parameters for each dye, is included in the Appendix B.3.

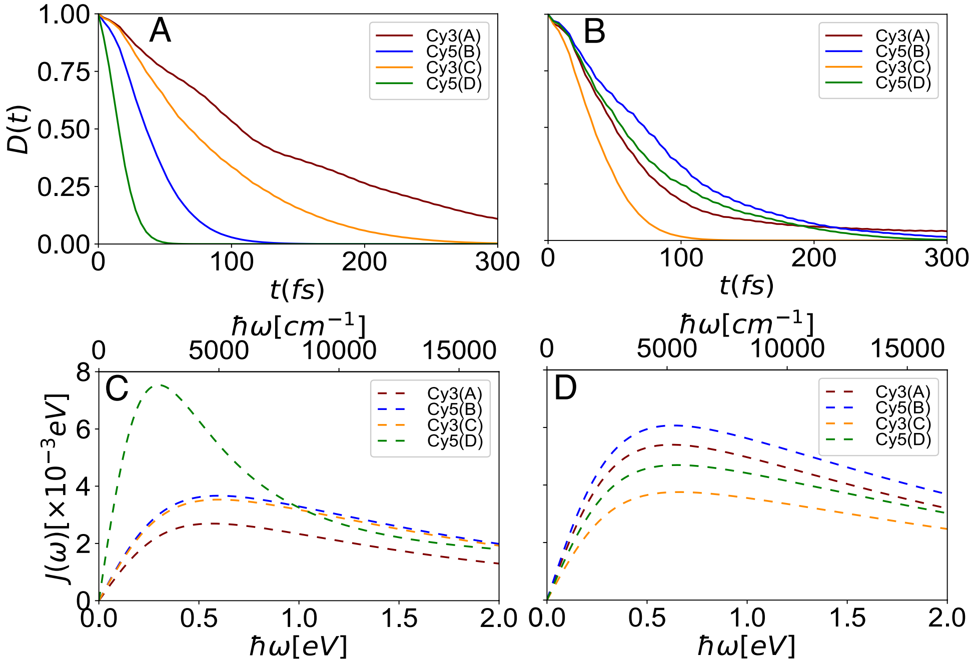

Figure 3-6: Numerical dephasing function for each dye in the circuit corresponding to (A) the first step of the D-J algorithm, $\hat{\mathcal{H}}_1$, and (B) for the third step, $\hat{\mathcal{H}}_3$. Spectral density fitted as in Eq. 3.15, for the dyes in circuits: (C) $\hat{\mathcal{H}}_1$, and (D) $\hat{\mathcal{H}}_3$.

We calculate the dephasing function by performing a numerical integration over the time component of C(t), as defined in Eq. 3.11. The dephasing function for each dye, in the circuits described by $\hat{\mathcal{H}}_1$ and $\hat{\mathcal{H}}_3$, is presented in Fig. 3-6A and B, respectively. This function describes the rate at which the phase of each dye decays as a result of its coupling with the bath. It can be shown that the rate of decay of $D(t)$ is directly proportional to $C(0)$, and inversely proportional to the correlation time, $\tau_{c,i}$. Physically, both quantities are related to the strength of the system-bath coupling and, thus, we expect the dyes exposed to stronger influence of the nuclear modes to dephase faster.

The dephasing times for the dye molecules in $\hat{\mathcal{H}}_3$ are $\tau_{D,A} = 82.1$fs, $\tau_{D,B} = 97.4$fs, $\tau_{D,C} = 43.0$fs and $\tau_{D,D} = 82.8$fs. These values, with an average of $\tau_D = 76.3$fs, are consistent with those reported for cyanine dyes in other studies [93]. We observe that only the Cy3(C) dye seems to deviate from the the other dye molecules possibly due to subtle differences in geometric arrangement or perhaps indicating the need for increased sampling. The dephasing times for the dye molecules in $\hat{\mathcal{H}}_1$ are much less homogeneous, with $\tau_{D,A} = 173.6$fs, $\tau_{D,B} = 45.9$fs, $\tau_{D,C} = 95.9$fs and $\tau_{D,D} = 18.9$fs. We note that the Cy3(A) appears to be remarkably protected from the effect of the thermal bath. The close proximity between the two Cy5(B and D) dyes appears to lead to faster dephasing for these two dyes. However, the value of τ_D for Cy5(D) is strikingly small, meaning there is an increased coupling to the bath that cannot be simply explained in terms of inter-atomic distances. A comparative analysis of the torsion angles of the geometries in $\hat{\mathcal{H}}_1$ (Appendix B, Fig. B-3) reveals a conformational change on the Cy5(B) dye, involving one of the heterodimer rings that may be responsible for the unexpectedly short dephasing time.

We compute the spectral density, $J(\omega)$, from Eq. 3.13. The power spectrum resulting from the numerical integration over the correlation function of each site gives rise to an intricate and noisy spectrum as plotted and discussed in Appendix B.3 and Fig. B-4. We thus capture the essential features in the low-frequency regime by fitting the noisy calculated $J(\omega)$ to the following functional form,

$$J(\omega) = \frac{2}{\pi\hbar} \tanh\left(\frac{\beta\hbar\omega}{2}\right) \left[\frac{a_1\tau_{c,1}}{\tau_{c,1}^2\omega^2 + 1} + \frac{a_2\tau_{c,2}}{\tau_{c,2}^2\omega^2 + 1}\right] \tag{3.15}$$

which is derived by assuming that $C(t)$ exhibits a double exponential decay (*i.e.,* $\tilde{a}_i = 0$ in 3.14). This fit spectral density is plotted in Figs. 3-6C and D, and the fitting parameters are presented in Table B.5 in the Appendix B. We observe the same tendency in $J(\omega)$ as in the dephasing function, $D(t)$, *i.e.*, the molecules more strongly coupled to the thermal fluctuations exhibit faster dephasing rate and larger peak amplitudes in the short-frequency range of the spectra.

The dephasing rate, $\gamma_m = 1/t_{D,m}$, and spectral density, $J_i(\omega)$, for every dye in each system provide a complete description of the system-bath component of the total Hamiltonian for that molecule (Eq. 3.1 to 3.3). We employ this description to realize the D-J algorithm with a realistic bath, by applying the same methodology used for the model bath in Sec. 3.4. Here, we solved the Redfield equations with $J(\omega)$ described by Eq. 3.15, and using the parameters calculated in this section, *i.e.*, t_D, $a_{1,2}$ and $\tau_{c;1,2}$. The resulting time-dependent dynamics are shown in Fig. 3-7, for the constant combined and serial versions of the algorithm. For the serial case, we maximize fidelity by eliminating the trivial action of $\hat{\mathcal{H}}_2$ (just the identity operator).

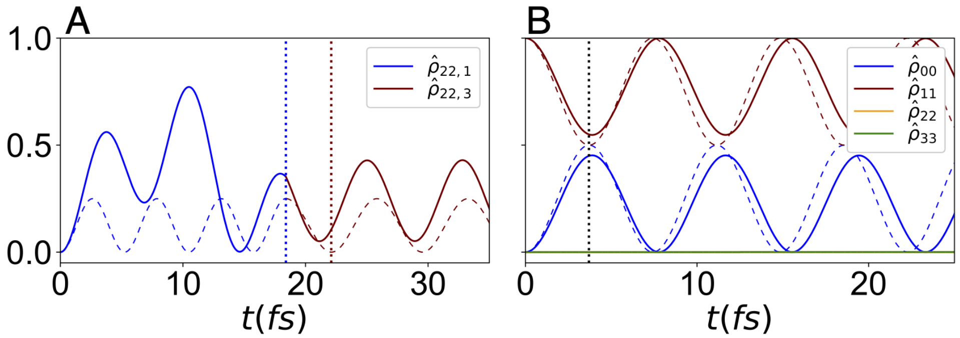

Figure 3-7: Time-evolution of the populations in the constant version of the D-J algorithm with the calculated bath. (A) The population for the *Cy3(C)* dye as the wavefunction evolves through the first and last step. The transformation time, τ, for each step is marked with blue and red dotted lines, respectively. (B) The populations for all four dyes for the single-step in the combined approach. Here, a single τ is indicated with a black dotted line. The populations for the closed system corresponding to the exact Hamiltonian evolution are shown in dashed lines, in both serial and combined approaches.

The fidelity of the cyanine-mapped algorithm is then calculated using Eq. 3.5. We find the simulated geometries encode the constant D-J algorithm with final fidelities of $\bar{F}(\tau_{\text{con}}) = 0.994$ and $\bar{F}(\tau_3) = 0.819$, for the combined and serial circuits, respectively. We note these values are better than those obtained with a model bath, which is expected, as these fictitious systems lose their phase about 20 times faster than the realistically simulated circuits.

We note that in both simulated Hamiltonians, $\hat{\mathcal{H}}_1'$ and $\hat{\mathcal{H}}_3'$, the oscillatory behavior is non-periodic, which results in increased stability against environment fluctuations, at least within the timescale of interest. This suggests that circuit fidelity depends almost entirely on the choice of circuit geometry, and not on its coupling with the harmonic bath. More conclusive results require a more accurate treatment of the intermolecular coupling, as Eq. 3.7 does not consider the effect of the thermal motion over the charge distribution of the individual dyes. While the limited study we present here cannot necessarily be generalized, we can safely state that design strategies that limit overall evaluation time and circuit-to-circuit exciton transfer will feature improved fidelity. To this end, the combined strategy is preferred, especially for simple computations with relatively few qubits.

In this chapter, we have mapped multi-step quantum operations into excitonic circuits by using the 2-qubit Deutsch-Jozsa algorithm as an example. We show this implementation can be approached with two general strategies: one by mapping the individual steps in the algorithm, involving the precise control of the initial state of each operation in the sequence (*i.e.,* a serial approach), and a second one were the entire algorithm is mapped into a single excitonic circuit realizing the transformation (*i.e.,* a combined approach). We have implemented these two strategies on a cyanine-based excitonic circuit, first by studying a model environment for the system-bath interaction, and second by explicitly simulating the thermal fluctuations with QM/MM simulations. While the atomistic model for the bath was able to describe the system-bath interaction for the excitonic circuit encoding the *constant* D-J algorithm, the operator representing the *balanced* algorithm indicates its implementation may be more challenging. In the next chapter, we will study an excitonic molecular system that exhibits the complex-value coupling seen in the Hamiltonian $\hat{\mathcal{H}}^{\text{bal}}_{\text{prod}}$.

Chapter 4

Complex-Valued Couplings for Coherent Control in Devices

4.1 Introduction

The location of an exciton can be controlled by the careful placement of an excitonic circuit molecular components. Controlling the direction in which an exciton flows within a circuit is more challenging, with the most reliable current design strategy being to utilize energetic gradients for funneling the flow of excitons. This strategy is effective but also necessitates performance loss in applications that rely on the efficient conversion or transfer of exciton energy [95]. The ability to control exciton position and flow without energy loss has the potential to improve the efficiency of existing excitonic technologies or to enable the development of new applications for excitonic circuitry.

In this chapter, we propose the use of complex-valued intermolecular electronic coupling as a novel method for controlling exciton directionality, for instance, in cyclic and branched excitonic circuits. Using simplified site-based models, I will illustrate the ability of complex-valued couplings (CVCs) to direct excitons one way or the other at bifurcating junctions. To connect with more realistic physical systems, I present a molecular motif capable of yielding CVCs and suggest a strategy for observing their effects in a laboratory setting.

For systems of many dye molecules, the structure of the intermolecular coupling network dictates the tendency of excitons to migrate or delocalize across the system. While delocalization can be modulated through variations in coupling strength, the directionality of migration is less easily controlled [28]. In principle, directional control over excitons can be achieved through the introduction of geometric phase into the coupling network. However, the viability of this strategy is not immediately clear since standard theories of intermolecular coupling (*e.g.*, Förster theory) do not allow for the appearance of phase. Here, we describe a model for a chromophore dimer system where a geometrical phase in the intermolecular coupling can be optically induced via circularly polarized light. First, we briefly review the topic of geometrical phase in quantum systems.

Geometric phase in quantum systems.

Geometrical phase is typically induced in quantum mechanical systems via electromagnetic potentials. In a phenomenon known as the Aharonov–Bohm (AB) effect [2], a quantum particle can experience a phase shift while circulating in the presence of a magnetic field. This approach to phase control has been studied in the context of quantum computing operations and information storage on multi-spin systems [137, 112], semiconductor quantum rings [16, 68], and in light-harvesting models for increasing the efficiency of electron transfer [22, 52, 156].

The AB effect can influence the phase of charge carriers driven across coupled molecules in ring configurations when subjected to an external magnetic field [52].

In such a system, a phase appears in the electronic coupling, $V_{mn} = |V|e^{i\theta_{mn}}$, with real V and ϕ_{mn}. In these closed-loop molecular circuits, phase can be manipulated to maximize energy transfer and minimize dissipation to the environment [22].

In principle, an analogous effect can be achieved for excitonic systems through the excitation of ring-like symmetric dyes with circularly polarized light. The phase of the resulting exciton dresses the intermolecular interactions, leading to the appearance of complex-valued components in the intermolecular electronic coupling.

4.2 A Dimer Model for Generating Complex-Valued Couplings

To explore this possibility, we consider an idealized minimal system capable of generating CVCs. As illustrated in Fig. 4-1, the system consists of two dye molecules, one that supports a circularly polarized exciton state and one that supports a linearly polarized exciton state. The coupling between these two exciton states includes a complex-valued geometric phase, as we describe below. This phase can be manipulated via chemical or geometric design to achieve control over exciton dynamics.

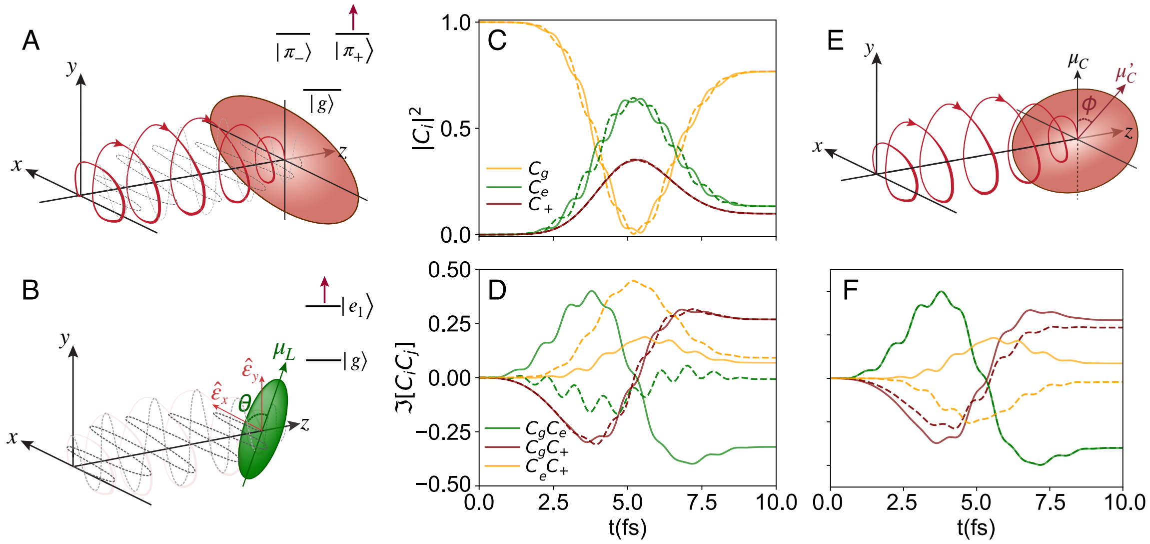

Figure 4-1: Complex-valued couplings can be induced in chromophore dimers. (A) A circularly polarized pulse propagating in the z axis acts on a molecule with $D_{N\mathrm{h}}$ symmetry (*circular* molecule), populating one of two delocalized excitations. Here the pulse is depicted as RCP and creates an exciton localized in the $|\pi_+\rangle$ state. (B) Schematic representation of the pulse acting on a molecule, which populates the first excited state. Unlike the *circular* molecule, the x and y components of the linear molecule's dipole moment, μ_L, are not symmetric and will interact with the corresponding components of the circular pulse (ε_x and ε_y, respectively) separately, according to the dipole angle with respect to the x axis, θ. (C) Time evolution of populations and (D) coherences of an exciton shared between a porphyrin and Cy3 molecules, after a RHS circularly polarized pulse is applied, as described in the text. Solid lines correspond to a choice of $\theta = 0$ and dashed lines to $\theta = \pi/2$. (E) A circularly polarized pulse acting on the $D_{N\mathrm{h}}$ symmetric molecule when the molecular plane is not orthogonal to the axis of propagation. The deviation is quantified by the angle ϕ. (F) Time evolution of the coherences for the dimer wavefunction when $\theta = 0$ and $\phi = 0$ and $\pi/3$ (solid and dashed lines, respectively).

We describe this system using the Frenkel exciton model, with a Hamiltonian given by 1.1, and the coupling defined as the overlap between the FE states (Eq. 1.2). In typical multichromophoric systems, this coupling is well approximated by Förster theory, which defines the coupling as the Coulomb interaction between the transition dipoles of chromophores n and m. The standard formulation of Förster theory appears to restrict the coupling V_{nm} to be real-valued. However, if one defines the coupling as the interaction between transition densities, rather than dipoles, then this apparent restriction is removed. A chromophore with a complex-valued transition density, *i.e.*, an exciton state with complex phase, can yield values of V_{nm} that are also complex-valued.

Molecules with high orbital symmetry naturally yield exciton states with complex character. For example, the lowest unoccupied molecular orbitals (LUMO) of a molecule with $D_{N\mathrm{h}}$ symmetry is a degenerate pair of $\pi_{\pm m}$ states, with $m = \pm 1$. The $D_{N\mathrm{h}}$ symmetry point group implies a regular n-sided prism or bipyramid. At this level of symmetry, the x and y components of the transition dipole moment (TDM) vector at the molecular plane have the same magnitude. As a result, one can set an arbitrary frame of reference to describe the dipole interactions of these molecules.For the remainder of this chapter, we will refer to a chromophore within this symmetry group as *circular*, and one with lower symmetry (*i.e.,* with a directional TDM component) as a *linear* dye.

The $\pi_{\pm m}$ states are eigenstates of the angular momentum operator, $\hat{l}_z$, with eigenvalues $\pm\hbar$, respectively, and can be described as linear combinations of real states π_x and π_y,

$$|\pi_\pm\rangle = \frac{1}{\sqrt{2}}\left(|\pi_x\rangle \pm i|\pi_y\rangle\right). \tag{4.1}$$

Similarly, the π_{mx}, π_{my} states with $m > 1$ can be written as linear combinations of the angular momentum $\pi_{\pm m}$ states. A linear pulse resonant with the HOMO-LUMO gap will create one of two real-valued excitations,

$$\begin{aligned}|\pi_x\rangle &= \frac{1}{\sqrt{2}}\left(|\pi_+\rangle + |\pi_-\rangle\right) \\ |\pi_y\rangle &= -\frac{1}{\sqrt{2}}\left(|\pi_+\rangle - |\pi_-\rangle\right),\end{aligned} \tag{4.2}$$

Notably, it is possible to selectively access the complex states $|\pi_\pm\rangle$ by using circularly polarized light, as demonstrated in previous studies with Porphyrin rings [11, 10, 86]. A circularly polarized laser pulse propagating in a direction perpendicular to the plane of the conjugated ring induces an electronic ring current in Mg-Porphyrin ($D_{4\mathrm{h}}$ symmetry). The resulting excitation carries a phase due to the induced magnetic field. This effect is illustrated in Fig. 4-1A, where a generalized $D_{N\mathrm{h}}$ molecule is depicted as a circle.

To evaluate the coupling between molecules with circularly (high symmetry) and linearly (low symmetry) polarized excitons (*i.e.*, via Eq. 1.2) we express each exciton state in a common Cartesian basis. In general, the wavefunction of an exciton generated via circularly polarized light can be described using Jones calculus [37],

$$|\psi_C\rangle = \frac{1}{\sqrt{2}}\left(|\psi_x\rangle \pm i|\psi_y\rangle\right). \tag{4.3}$$

For the molecule with $D_{N\mathrm{h}}$ symmetry, represented in Fig. 4-1A, $\psi_{x(y)}$ correspond to the $\pi_{x(y)}$ states defined in Eq. 4.2, and the phase of the light wave is omitted for simplicity. In contrast, the first excitation of a molecule with lower symmetry, such as depicted in Fig. 4-1B, is a real, non-degenerate state that can be accessed through a pulse resonant with the molecule's transition energy. The wavefunction of an excitation induced by a linearly polarized pulse propagating in the z direction can be separated in its x and y components,

$$|\psi_L\rangle = \cos\theta|\psi_x\rangle + \sin\theta|\psi_y\rangle, \tag{4.4}$$

where $|\psi_{x(y)}\rangle$ is the wavefunction resulting from the interaction of the system with the

$x(y)$ component of the light, weighted by the angle θ of the transition dipole moment of the molecule, μ_L, with respect to the x axis (Fig. 4-1).

With the exciton states defined in Eqs. 4.3 and 4.4, according to the Frenkel model, the coupling between a circularly and linearly polarized molecule is given by,

$$V_{LC} = \cos\theta V_x \pm i \sin\theta V_y, \tag{4.5}$$

where $V_{x(y)} = \langle \psi_g^C \psi_{e,x(y)}^L | \hat{H} | \psi_{e,x(y)}^C \psi_g^L \rangle$ is the $x(y)$ component of the coupling between the low- and high-symmetry molecules. Note here that the phase will only appear in the interaction when the circularly-polarized molecule is coupled to a low-symmetry molecule, otherwise, the frame of reference for the corresponding dipoles is indistinguishable.

Optical excitation of a CVC dimer system.

To demonstrate that circularly polarized light can, in fact, induce a delocalized excitation in a system of one *linear* and one $D_{N\mathrm{h}}$ *circular* dye, we employ a Frenkel exciton model describing the electronic state of the coupled system. In this model, a pair of coupled *linear* and *circular* dyes has a total of four electronic states: An initial state where both dyes are in the ground state, $|g\rangle \equiv |gg\rangle$, one where the exciton is located in the *linear* molecule and the *circular* molecule is in the ground state, $|e\rangle \equiv |eg\rangle$, and when the exciton is located in the $\pi_\pm$ MO of the *circular* molecule, $|+\rangle \equiv |g+\rangle$ and $|-\rangle \equiv |g-\rangle$. Following the model described in Ref. [11], we write the wavefunction for the 4-state exciton system,

$$\begin{aligned} |\Psi(t)\rangle = & C_g(t)|g\rangle e^{-iE_g t/\hbar} \\ & + C_e(t)|e\rangle e^{-iE_e t/\hbar} \\ & + C_+(t)|+\rangle e^{-iE_+ t/\hbar} \\ & + C_-(t)|-\rangle e^{-iE_- t/\hbar}, \end{aligned} \tag{4.6}$$

where $C_i(t)$ and E_i are the wavevector coefficients and transition energies for the exciton state $|i\rangle$, with $i = g, e, +$ and $-$.

We evaluate the effect on the wavefunction above after the system is perturbed by a circularly polarized laser field $\varepsilon_{\pm}(t)$, by describing its evolution via the time-dependent Schrödinger equation under the dipole approximation,

$$i\hbar|\dot{\Psi}(t)\rangle = (H_{el} - \hat{\mu}\cdot\varepsilon_{\pm}(t))\,|\Psi(t)\rangle, \tag{4.7}$$

where $\hat{\mu}$ is the dipole moment operator, defined as the summation of the product of charge q_j and position r_j for all charged particles j, $\hat{\mu} = \sum_j q_j r_j$. The right/left circularly polarized pulse (RCP/LCP) is described in terms of its cartesian components,

$$\varepsilon_{\pm}(t) = \varepsilon_0 s(t)[\cos(\omega t + \eta)\hat{e}_x \pm \sin(\omega t + \eta)\hat{e}_y], \tag{4.8}$$

with field amplitude ε_0, carrier frequency ω, phase η, shape function $s(t)$ and unit vectors e_x and e_y along the x- and y-axes.

We derive an expression for the coefficients $C_i(t)$ after an RCP pulse with frequency resonant to the *circular* dye, ω_C, is applied by combining Eq. 4.7 with the time-independent Schrödinger equation, $H_{el}|\Psi_i\rangle = E_i|\Psi_i\rangle$. A complete derivation is presented in the Appendix C.1. Using the Rotating wave approximation (RWA) to simplify the expression we find that for a RCP pulse,

$$\begin{aligned}\dot{\mathbf{C}}(t) = {} & \frac{i}{\hbar}\varepsilon_0 s(t)\times \\ & \begin{pmatrix} |\mu_L|\cos(\theta-\omega_C t)C_e(t)e^{-i\omega_L t} + \mu_C C_+(t) \\ |\mu_L|\cos(\theta-\omega_C t)C_g(t)e^{i\omega_L t} \\ \mu_C C_g(t) \\ 0 \end{pmatrix}.\end{aligned} \tag{4.9}$$

From this ODE system, we note that the dipole angle, θ, adds a phase to the circularly polarized field acting on the linear exciton with coefficient evolving as $C_e(t)$. On the other hand, the effect of the pulse in the *circular* dye depends exclusively on the magnitude of the corresponding dipole, meaning that the choice of a coordinate system is irrelevant for this dye owing to its high molecular symmetry. When the same pulse interacts with the asymmetric *linear* dye, the equal-magnitude x and y components of the field interact with the components of the dipole vector separately, weighted by the relative angle of the dipole, as described by Eq. 4.4.

The ODE system in Eq. 4.9 does not have an analytical solution, therefore we provide a numerical solution for the system of equations using the molecular and pulse parameters from Ref. [11]: $\varepsilon_0 = 2.20 \times 10^9$ Vm^{-1} and $s(t) = \sin^2\left(\frac{\pi t}{t_p}\right)$, with $t_p = 9.67$fs the duration of the pulse. The *circular* molecule is chosen to be Mg-Porphyrin, with $\mu_C = -1.84\ ea_0$ and $\hbar\omega = 2.21$ eV, and the *linear* molecule to be Cy3 ($\mu_L = 5.04\ ea_0$ and $\hbar\omega = 2.27$ eV). The Resulting populations, $|C_i|^2$, and coherences $\mathcal{I}[C_i C_j]$ between the four states are shown in Fig. 4-1C and D, for $\theta = 0$ (solid) and $\pi/2$ (dashed). Here, $\mathcal{I}[C_i C_j]$ refers to the imaginary component of $C_i C_j$. As described, the phase will almost exclusively affect the formation of the linear exciton state, $|e\rangle$, with the effect more readily observed in the exciton coherences (Fig. 4-1D). Note that the *linear* exciton populates more than the *circular* due to differences in the dipole strength.

In the derivation above we have assumed that the z axis of light propagation is aligned to be exactly orthogonal with the xy plane of the *circular* molecule. In a real experimental setting, however, maintaining precise placement of the dye and pulse to achieve this configuration can be challenging. Additionally, the alignment of the molecule in relation to the light might vary over time. To address this issue, we can derive a system of equations describing the wavefunction evolution of the dimer system as a function of the angle ϕ. This angle represents the alignment of the axis of light propagation with the *circular* molecule's xy plane, as depicted in Fig. 4-1E. Adopting an approach akin to the one used for the dipole angle θ, we arrive at the following system of equations. A complete derivation can be found in Appendix C.2,

$$\dot{C}(t) = \frac{i}{\hbar}\varepsilon_0 s(t) \begin{pmatrix} |\mu_L| \cos(\theta - \omega_C t) C_e(t) e^{-i\omega_L t} + \mu_C e^{i\phi} C_+(t) \\ |\mu_L| \cos(\theta - \omega_C t) C_g(t) e^{i\omega_L t} \\ \mu_C e^{-i\phi} C_g(t) \\ 0 \end{pmatrix}. \tag{4.10}$$

Interestingly, the coefficients $\dot{\mathbf{C}(t)}$ match those derived for the aligned dimer system in

Eq.4.9. Here, the alignment angle ϕ functions merely as a global phase in the evolution of the $|\pm\rangle$ wavefunction, $C_+(t)$. Since the ODE system lacks an analytical solution, we numerically solve it using the same pulse parameters as before. Coherences $\mathcal{I}[C_iC_j]$ for $\phi = \pi/3$ are depicted in Fig.4-1F using dashed lines, compared to those for a perfectly aligned system with $phi = 0$ and $\theta = 0$. Populations $|C_i|^2$ for an arbitrary alignment given by ϕ will be identical to those of the $phi = 0$ dimer. These findings show that in a linear-circular excitonic circuit, only the relative geometry of the linear molecule–defined by angle θ–has an effect on the populations, and not the placement of the *circular* dye.

4.3 Results

Two-dye Model System

Having defined the general mathematical model for the interaction between a circularly polarized exciton and a linearly polarized exciton, we now describe the evolution of an exciton within such a dimer pair. A Hamiltonian matrix for the dimer system can be defined using Eq. 1.1, with $N = 2$,

$$\hat{H}_{\text{dimer}} = \begin{pmatrix} E_L & V_{LC} \\ V_{CL} & E_C \end{pmatrix} \tag{4.11}$$

where E_L and E_C are the energies for the linearly and circularly excited molecules, respectively, and $V_{CL} = V_{LC}^*$. As before, we choose $E_C = \hbar\omega_C$ to be the excitation energy of Mg-Porphyrin and $E_L = \hbar\omega_L$ that of a Cy3 dye. Arbitrary values for the real components of the coupling are set to be proportional to the energy difference between the two Frenkel exciton states, $V_x = \Delta E_{LC}/2$ and $V_y = 3\Delta E_{LC}/4$, with $\Delta E_{LC} = E_L - E_C$. The dimer system is depicted in Fig. 4-2A.

The dimer described by Eq. 4.11 can be evolved using the Liouville equation,

$$\dot{\rho} = -\frac{i}{\hbar}\left[\hat{H}_s, \rho(t)\right] \tag{4.12}$$

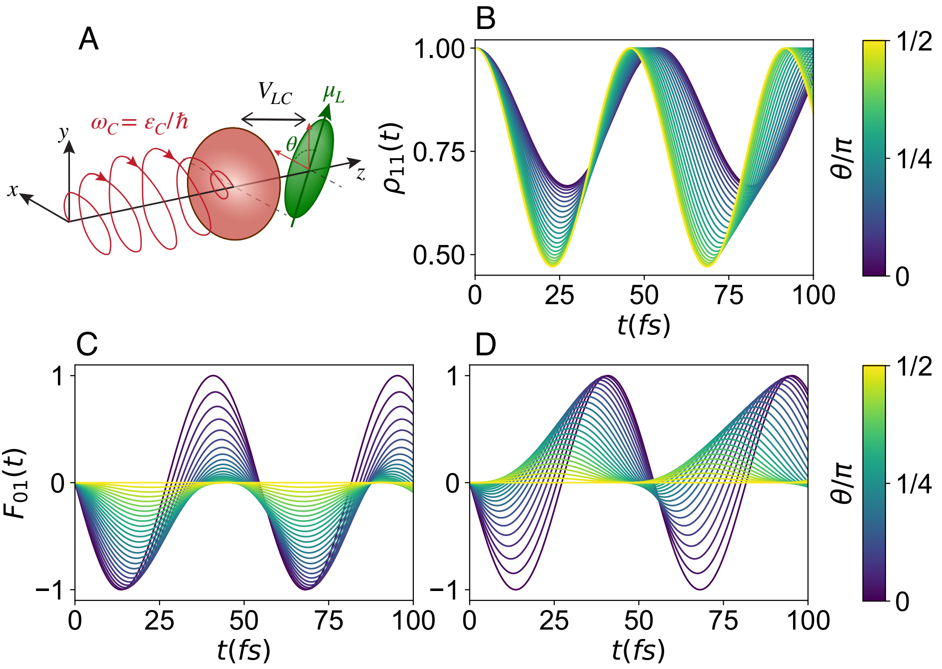

Figure 4-2: Two-dye model system with complex-valued coupling. (A) Representation of a dimer with imaginary excitonic coupling. An aromatic ring with $D_{N\mathrm{h}}$ symmetry is excited via a circularly polarized pulse resonant with the first excitation $\omega_C = E_L/\hbar$, and a resonant linearly polarized pulse is applied to the other molecule with $\omega_L = E_L/\hbar$. (B) Exciton populations for the dimer for changing phase angle θ and normalized excitonic flux, $\overline{F}_{01}$, as described in the text, for a (C) RCP and (D) LCP incident pulse.

where ρ is the density matrix describing the evolution of the closed system. The expression above leads to a system of ODEs for the matrix elements of the density matrix, which can be solved to obtain the population dynamics of the exciton, i.e., the diagonal elements ρ_{ii}. Starting from an initial state when the exciton is localized in the circularly-polarized molecule, $i = 1$, we derive the populations $\rho_{11}(t)$ with varying phase angle, θ (Fig. 4-2B).

The populations ρ_{ii} provide information about the location of the exciton at a given time, t, but do not provide insight into the process of coherent exciton transfer between the dyes. For instance, if we treat the coupling as a global phase $V_{LC} = |V|e^{i\theta}$, which is the case when $V_x = V_y$, the populations are predicted to be independent of the phase angle. When the initial state of the system is localized on one of the molecules, this factor will merely act as an overall phase in the evolution of the site-basis probability amplitudes, $C_i(t)$. On the other hand, the imaginary part of the off-diagonal elements of the density matrix, $\mathcal{I}[\rho_{ij}]$, contains information about the quantum coherence and therefore the direction of the exciton flux.

To define the directionality of flow in exciton population, we adopt the definition of exciton flux between two molecules m and n from Refs. [151, 154] ,

$$F_{mn} = 2V_{mn}\mathcal{I}[\rho_{mn}]. \tag{4.13}$$

In this expression, the sign of the flux, F_{mn}, specifies the direction of the coherent exciton transfer, *i.e.*, $F_{mn} = -F_{nm}$. The normalized exciton flux, $\overline{F}_{mn}$, is calculated for the dimer as a function of θ for both RCP and LCP light (Fig. 4-2B and C, respectively). Note that excluding the two limiting cases where $\theta = 0, \pi$, we see that in general $F_{mn}^{(\mathrm{RCP})}(t) \neq -F_{mn}^{(\mathrm{LCP})}(t)$, meaning that inverting the polarization of the pulse will not simply shift the direction of the exciton flux, but will also affect the magnitude of flux at a given time.

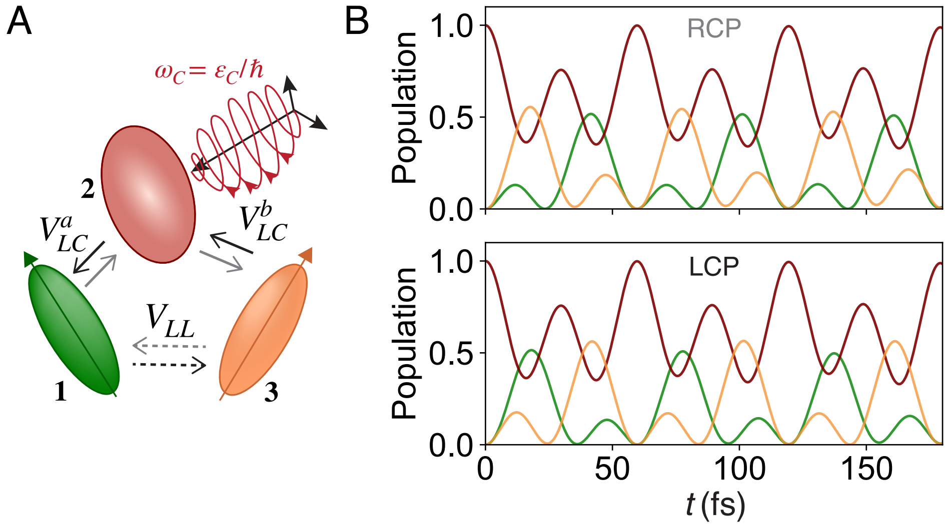

Figure 4-3: Three-dye model system with complex-valued coupling. (A) The 3-dye system described in Eq. 4.14. One dye with $D_{N\mathrm{h}}$ symmetry is excited with circularly polarized light (red circle) and is coupled to two low-symmetry dyes (a and b). (B) For two linear dyes with different relative orientations with respect to the circular dye, $\theta_a \neq \theta_b$, inverting the direction of the light will change the order at which an exciton initially localized at **1** populates the other two sites.

Three-dye cycle.

We now extend the framework introduced for circular-linear interactions into larger Hamiltonians. One system of interest that has been studied in the context of the AB effect is a cycle made up of three sites all coupled to each other. A magnetic-induced phase in the interaction between these sites was demonstrated to invert the order at which the charge carrier populates neighboring states [52, 22]. An analogous effect can be achieved for an exciton in a model three-molecule system, as illustrated in Fig. 4-3A. The following Hamiltonian describes a 3-dye system containing one $D_{N\mathrm{h}}$ molecule excited through circularly polarized light, interacting with two asymmetric molecules,

$$\hat{H}_{\mathrm{3cycle}} = \begin{pmatrix} E_L^a & V_{LC}^a & V_{LL} \\ V_{CL}^a & E_C & V_{LC}^b \\ V_{LL} & V_{CL}^b & E_L^b \end{pmatrix}. \tag{4.14}$$

In $\hat{H}_{\mathrm{3cycle}}$, the linear-circular coupling, V_{LC}, carries a phase while the linear-linear interaction V_{LL} does not.

The Hamiltonian $\hat{H}_{\mathrm{3cycle}}$ can be evolved as a closed system with Eq. 4.12 by solving the corresponding equations of motion. Starting from an excitation induced on the circular molecule, the ordering of the sites the exciton occupies changes with respect to the exciton direction, indicating the exciton flux may be switching from clockwise to counter-clockwise when using an RCP or LCP pulse, respectively (Fig. 4-3B upper and lower boxes). In this model, we set the energies of the circularly polarized excitation to be the porphyrin excitation energy and the linearly polarized molecules both to Cy3. The phase angle is different for each Cy3 molecule, which would be the case if, for example, they are arranged at different angles with respect to the pulse. It is worth noting that if the molecules are parallel to each other, *i.e.*, $\theta_a = \theta_b$, no local phase is introduced into the system, as the population initialized at E_L will equally populate either one of the linear sites.

We calculate the normalized flux using Eq. 4.13 for the clockwise path: F_{23}, F_{31} and F_{12}. For the 3-dye cycle the condition $F_{mn} = -F_{nm}$ still holds for any given site, but the total flux coming in and out of the site is not necessarily equivalent. For example, for site 1 (E_L^a), the net flux that circulates in the clockwise direction is given by $F_1 = F_{12} - F_{31} \neq 0$. However because the construct is a closed ring and is isolated from the environment, the sum of net flux for all three sites must be equal to zero for the system to maintain detailed balance. Because there is nothing that forces the exciton to flow consistently in a given direction (*e.g.,* an electron trap) a fraction of the population will flow in the opposite direction.

The direction of exciton flow cannot easily be estimated from the dynamics plotted in Figs. 4-3. We quantify the overall direction of population flow by adding the total flux in a given direction: $F_{\text{right}} = F_{23} + F_{31} + F_{12}$ and $F_{\text{left}} = -F_{\text{right}}$. We found that when an RCP pulse is used $F_{\text{right}} = 1.65 - 17.2i$ and an LCP pulse leads to $F_{\text{right}} = -2.04 - 17.3i$ eV. Clearly, switching the polarization of light inverts the global direction of the exciton flow, although the inversion is not complete given the difference in the electronic coupling between the sites (arising from a difference in phase, θ).

Branched circuit.

In addition to driving circular flow in ring-like excitonic circuits, complex-valued coupling can enable excitons to be directed along specific paths in branched excitonic circuits. To demonstrate this capability, we designed a model of branched circuits with two paths of linear dye molecules originating from a central high-symmetry dye molecule excitable with circularly polarized light. This circuit is illustrated in Fig. 4-4A. A Hamiltonian describing this system is given by,

$$\hat{H}_{\text{branched}} = \begin{pmatrix} E_C & V_{CL,a} & V_{CL,b} & 0 & 0 \\ V_{LC,a} & E_{L,a} & 0 & V_{LL} & 0 \\ V_{LC,b} & 0 & E_{L,b} & 0 & V_{LL} \\ 0 & V_{LL} & 0 & E_{L,a} & 0 \\ 0 & 0 & V_{LL} & 0 & E_{L,b} \end{pmatrix}. \tag{4.15}$$

As with the previous examples, the energies of the circular and linear molecules are taken as those for Mg-Porphyrin and Cy3, respectively, and all the linear molecules have identical energies (*i.e.,* $E_{L,a} = E_{L,b} = E_{Cy3}$ and $E_C = E_{MgPh}$. The coupling between the circular and linearly excited sites is defined with Eq. 1.2, and the phase θ is different for every path (illustrated with green and orange in Fig. 4-4A, respectively).

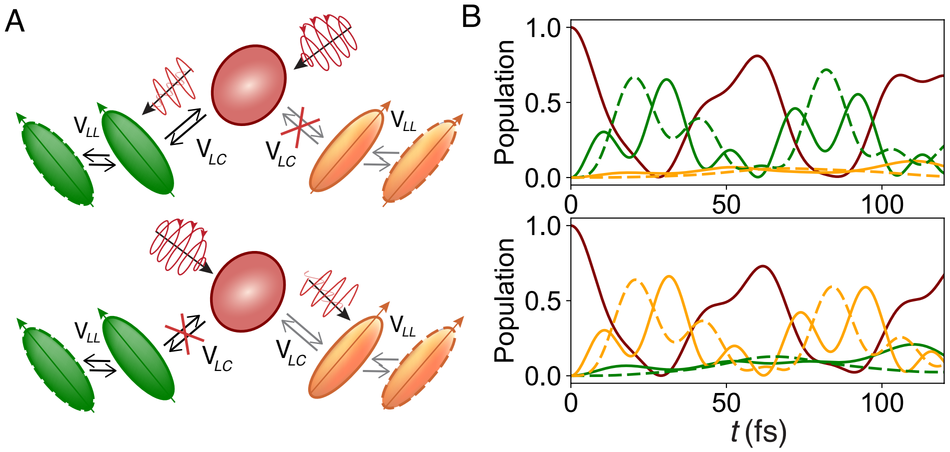

Figure 4-4: Branched excitonic circuit with complex-valued coupling. (A) System described by the Hamiltonian Eq. 4.15, consisting of two separate linear circuits connected to the same central $D_{N\mathrm{h}}$ molecule. The cases when the phase is set to $\theta = 0$ and $\pi/2$ are illustrated, resulting in the green and orange paths being blocked, respectively. (B) The populations for both cases are calculated, evidencing that the population flux is almost completely stopped by careful manipulation of θ. The top and bottom plots correspond to the diagrams on the left.

For simplicity, the linear-to-linear coupling V_{LL} is set to half the energy difference ΔE_{LC}.

Starting from an exciton fully localized on the central molecule via a circularly-polarized pulse (red circle in Fig. 4-4A), the amount of population flowing into each of the two connected molecules will depend on their relative angle with respect to the incident light. When the connected dyes (green and orange solid lines) are placed orthogonally with respect to each other (for example, by setting $V_x^a = V_y^b$), the exciton flux is completely blocked when the incident light is directed parallel to one set of dyes (no flux), and orthogonal to the other (full flux). In the example shown in Fig. 4-4A, when the light is parallel to the green path and orthogonal to the orange one, the first path is blocked (top diagram). When the light is parallel to the orange dyes, this path is blocked instead (bottom diagram). Note that a full delocalization across the circular and all the linear dyes in the activated path (both solid and dashed lines) is achieved by aligning the linear dyes parallel to each other.

We calculated the exciton populations for the described model, setting $V_{LC,a}^x = V_{LC,b}^y = 5\Delta\epsilon_{LC}/4$ and $V_{LC,a}^y = V_{LC,b}^x = \Delta\epsilon_{LC}/4$. Switching the relative phase, $\theta =$

$\theta_a = \theta_b$, between 0 and $\pi/2$ will almost completely block the flux to the orange and green paths, respectively. This same idea can be generalized for complex constructs connecting more than two paths with similar results. We note that in this particular circuit architecture, the direction of the circularly polarized light has no effect on the exciton flux when θ is fixed. As was previously observed in Ref. [52], the AB effect will not manifest in open cycles, and therefore, switching between RCP and LCP light will not change the exciton flux in Fig. 4-4. In fact, one can argue that circularly polarized light is not strictly necessary in this particular construct. A similar phase control could be achieved with a linear pulse on a circuit of dyes with precisely aligned dipole moment vectors. Indeed, the control of the phase is an artifact of the alignment between the molecules and does not necessarily arise for the complex phase in the coupling.

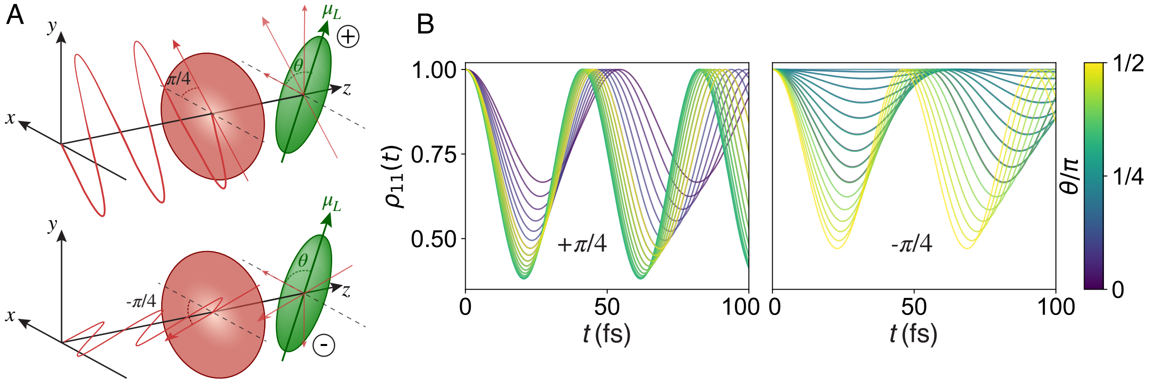

Figure 4-5: Geometrical phase induced with real-valued coupling. (A) A linear pulse directed at an angle of exactly 45 ith respect to a molecule. The resulting wavefunction will have x and y components of the same magnitude. When coupled to a second molecule, the magnitude of the coupling will depend on the alignment with the second molecule, which can constructively or destructively interfere with the first. (B) The evolution of a simplified system of the model described, when the x and y components are constructive and destructively interfering (left and right, respectively), as a function of the alignment angle θ.

To highlight the unique effects that arise from systems with CVCs, we consider a system that exhibits a real-valued excitonic coupling, but with a similar component separation to that in Eq. 4.5. In particular, when a linear pulse is directed at a ±45°angle with respect to the x axis, the Jones vector takes the form, $|\psi_{\pm\pi/4}\rangle =$

$\frac{1}{\sqrt{2}}\left(|\psi_x\rangle \pm |\psi_y\rangle\right)$. Such a pulse applied to the same system of symmetric and asymmetric dyes will lead to an expression for the coupling with the same form as that for the V_{LC} coupling,

$$V_{L(\pm\pi/4)} = \cos\theta V_x \pm \sin\theta V_y. \tag{4.16}$$

A representation of this dimer system is shown in Fig. 4-5A. The interaction with a second molecule will amplify or decrease the components of the coupling, such that two molecules that are fully aligned will exhibit the strongest coupling (Fig. 4-5B left panel), and orthogonally-placed molecules will have the least coupling strength (Fig. 4-5B right). Therefore, it is possible to implement the same effect as in Fig. 4-4, just by taking advantage of the molecular alignment. Specifically, a symmetric molecule excited with a linear pulse at exactly 45°will give the same effect observed in Fig. 4-4 with a phase-dependent coupling. However, because there is no phase introduced into the system, the AB effect and the control of exciton coherences are not present. Therefore, the control over excitonic flux as presented in Fig. 4-3 would not be possible. Note that we specifically use a $|\psi_{\pm\pi/4}\rangle$ pulse applied to a symmetric molecule to obtain a coupling equation comparable to that of Eq. 4.3, but the dipole-dipole interference can be applied to any pair of dyes excited with a classical field.

In this chapter, I have described a method to introduce a phase dependency on the electronic coupling between interacting chromophores. We have demonstrated that RCP and LCP light can be used to control the sign of the phase, while the magnitude of the phase can be adjusted by changing the angle of the incident light with respect to the linear molecule, either through modifying the laser parameters or the geometrical orientation of the molecules. The effect presented here could have important implications for the development of efficient organic semiconductor materials, providing a strategy for directional excitonic flux in the coherent EET regime. To provide a simple and tractable model for the imaginary coupling we assumed the environment only couples weakly to the system, but we anticipate our model can be easily expanded to include the effect of strong system-bath interactions.

Part II

Exciton Circuits in DNA Nanostructures: An Atomistic Model

Chapter 5

Quantifying Molecular Coupling in Dimers Scaffolded in DNA

5.1 Introduction

The previous chapters 2-4 explored the intricacies of exciton evolution via chromophore coupling and introduced the ability to control exciton delocalization and transport through molecular arrangement. Molecular coupling was found to arise from the alignment between transition dipole moments associated with individual chromophores. This long-range interaction, commonly referred to as Coulombic or excitonic coupling, manifests between exciton units localized within individual molecules.

Early theories of molecular excitons, as proposed by Davydov [43] and Kasha [87, 88, 107], suggest that photophysical behaviors of chromophore aggregates stem largely from electrostatic interactions between adjacent molecules. In this framework, transition dipole vectors that are either aligned head-to-tail or side-by-side result in the formation of J-aggregates and H-aggregates, respectively. The former leads to positive excitonic coupling, while the latter results in negative coupling.

Yet, in tightly packed aggregates, dyes may exhibit configurations favorable to $\pi-\pi$ stacking. Such arrangements prompt spatial overlap between the MOs of neighboring chromophores, inducing *short-range* effects like charge-transfer (CT) coupling. These charge transfer interactions entail the spatial separation of the electron and hole forming the exciton across different chromophore units.

In π-stacked aggregates, notably within light-harvesting complexes (LHCs), both long- and short-range interactions can be observed simultaneously. In LHCs, relative chromophore orientation and, therefore, the balance between the two effects is controlled via precise molecular placement within protein scaffolds [130]. Understanding the dynamics between these interactions is crucial for elucidating key photophysical phenomena, such as symmetry-breaking charge separation (SB-CS), which propels the conversion of photon-induced excitons into chemical energy[124]. Furthermore, modulation of excitonic and CT contributions has also been studied in the context of singlet fission, excimer, and charge-transfer state formation using covalently bonded chromophores [5, 6, 39, 89, 127, 132, 155].

Covalent chromophore aggregates, however, face significant constraints due to synthetic limitations [78, 77]. Enter DNA nanotechnology. Current advancements in this field have unlocked the potential to develop distinctive architectures and functionalities [29, 80, 146] Pairing this with the ability to scaffold dye aggregates in DNA with precise positions and orientations [17, 50, 64], posits DNA as an attractive platform for designing programmable and functional excitonic materials. Notably, while DNA materials have traditionally been employed as a framework to control exciton transfer and evolution, as dictated by Coulombic and Forster-type coupling [21, 66, 72, 74], short-range CT coupling had not yet been demonstrated in DNA-scaffolded constructs before our recent study [71].

In this chapter, I introduce DNA scaffolding as a strategy for fine-tuning inter-chromophore coupling. I present an analysis of exciton evolution, focusing on the contrast between long- and short-range interactions within Squaraine dimers scaffolded in double-stranded DNA. Our theoretical insights are paired with experimental observations, as reported by our collaborators for the same chromophore systems. In the next section, I describe our computational strategy, employing a combination of molecular dynamics (MD) and quantum mechanical simulations to accurately calculate the excitonic and CT coupling, while also incorporating the statistics of the DNA-scaffolded aggregates. Finally, I employ our methodology to explain the CT and exciton interplay as reported in spectroscopical measurements.

5.2 Theroretical Model

In the previous chapters we represented excitons in a localized Frenkel exciton basis, where the electron and the hole are both located in the same molecule. In this chapter, I evaluate the effects of close-packing in chromophore dimers scaffolded in DNA. To this end, we shall employ a Hamiltonian model expanded to include the effect of charge transfer states, as introduced earlier in Section 1.1.

We calculate the contribution of the long- and short-range coupling to the total chromophore-chromophore interaction,

$$V_{\text{total}} = V_{\text{excitonic}} + V_{\text{CT}}. \tag{5.1}$$

The Coulombic or excitonic coupling was previously approximated as an interaction between transition dipoles in Chapter 2 (Eq. 2.1) and between sets of monopoles in Chapter 3 (Eq. 3.7). A more exact derivation of the coupling can be done in terms of two-electron integrals of occupied and virtual orbitals,

$$V_{\text{excitonic}} = \sum_{i,a,j,b} c_{i,a}^{(1)} c_{j,b}^{(2)} [2(\psi_i^{(1)}\psi_a^{(1)}|\psi_j^{(2)}\psi_b^{(2)}) - (\psi_i^{(1)}\psi_j^{(2)}|\psi_a^{(2)}\psi_b^{(1)})]. \tag{5.2}$$

where $\psi_i^{(1)}$ represents the orbital i in monomer 1, and $c_{i,a}^{(1)}$ is the CIS coefficient describing the excitation of a single electron from occupied MO i to virtual MO a. The first term in Eq. 5.2 is the Coulomb integral $(ia|jb) = \int dr_1 dr_2 \psi_i^*(r_1)\psi_a(r_1)r_{12}^{-1}$ $\times\psi_j^*(r_2)\psi_b(r_2)$, while $(ij|ab)$ is an exchange integral and is often negligible unless molecules exhibit a significant spatial overlap. The two-electron integrals can be calculated using time-dependent density functional theory (TDDFT) or configuration interaction singles (CIS) with the Tamn-Dancoff approximation (TDA).

The CT coupling is calculated following Eq. 1.6, which describes a CT-mediated energy-transfer process, as previously introduced. We calculate the energy gap $\Delta E_{\text{CT}-\text{FE}} = E_{\text{CT}} - E_{\text{FE}}$ through the bonding energies $\Delta E_{\text{CT}-\text{FE}} = U(0) - U_{\text{CT}}$. The local binding energy, $U(0)$, is taken here as a constant set to 0.7 eV [152], while the CT binding energy, U_{CT}, is calculated with Eq. 1.4. The electron/hole transfer integrals can be determined via DFT calculations.

5.3 Long and Short-Range Coupling in Squaraine Dimers

In this chapter, I present a combined theoretical and experimental effort to design programmable circuits that exhibit symmetry-breaking charge transfer—a phenomenon where a CT excited state forms with the electron and hole distributed across an identical chromophore pair. The platforms studied here were zwitterionic squaraine dimers in Duplex DNA. Renowned for their susceptibility to electron donating and accepting groups, squaraine chromophores exhibit strong absorption in the visible spectrum [140]. Phosphoramidite-modified squaraine dyes were scaffolded in the DNA via the phosphate groups of the DNA backbone (See Fig. 5-1A).

The purpose of this study was to showcase the design flexibility DNA scaffolding offers. To this end, the squaraine dimers were tethered to DNA in two primary methodologies: first, by hybridizing one strand containing two attached chromophores to its chromophore-absent counterpart; and second, by hybridizing two chromophore-containing strands. The resulting DNA structures contained a pair of *serial* and a pair of *parallel* dyes, respectively. Each pair of dimers was also separated by a variable number of nucleotide bases Δn, with n the number of base pairs separating the pair. Here, Δn was varied from 0 to 3 for the serial dimer (Fig. 5-1B), and from 0 to 2 for the parallel (Fig. 5-1C). Throughout these manipulations, consistent local DNA sequences were maintained, ensuring any resultant photophysical alterations stemmed from chromophore coupling variations and not DNA scaffold interactions.

The absorption spectrum was measured for the two dimer configurations and different nucleotide separations and is presented in Figures 5-1B and C for the serial and parallel dimers. The spectrum of a squaraine monomer scaffolded in DNA is also presented for comparison. The absorption spectrum of chromophore dimers typically contains two main vibronic bands, 0–0 (left) and 0–1 (right). A redistribution of these bands compared to the monomer is characteristic of H-type dimers. In fact, the redistribution of these vibronic bands, quantified by the ratio of their intensities, $\nu_{00}/\nu01$, is directly proportional to the intermolecular coupling strength. Notably, for both the serial and parallel configurations, the spectra evinced a pronounced vibronic band separation, indicative of strong intermolecular coupling—a phenomenon seemingly unaffected by nucleotide spacing variations. The band ratios were calculated by fitting the absorption spectra into a two-Gaussian model to obtain the relative band strengths [71]. The resulting experiment band ratios are plotted in Fig. 5-3A.

Although the absorption spectrum gives an overview of the total coupling strength, it doesn't precisely capture the interplay between excitonic and CT contributions in π-stacked chromophores, as seen in section 5.2. Grasping the intricacies of this interplay becomes imperative for deciphering the spectral distinctions between the serial and parallel configurations. Moreover, the spectra's apparent insensitivity to nucleotide spacing, contrary to the intuitive expectation of reduced interaction strength with increased chromophore separation, requires further exploration.

In the subsequent section, I introduce a computational approach designed to evaluate the excitonic and CT coupling strengths for chromophore pairs in DNA. This will help us understand the relationship between the experimental spectra and the underlying physics of chromophore interactions.

5.4 A Combined Molecular Dynamics and Quantum Mechanical Approach

In an effort to understand the interplay between excitonic and charge transfer interactions in chromophore aggregates and how they relate to DNA scaffolding patterns, we examined two DNA constructs: serial $\Delta 0$ and parallel $\Delta 0$. Our approach combined molecular dynamics (MD) simulations with quantum mechanical techniques to

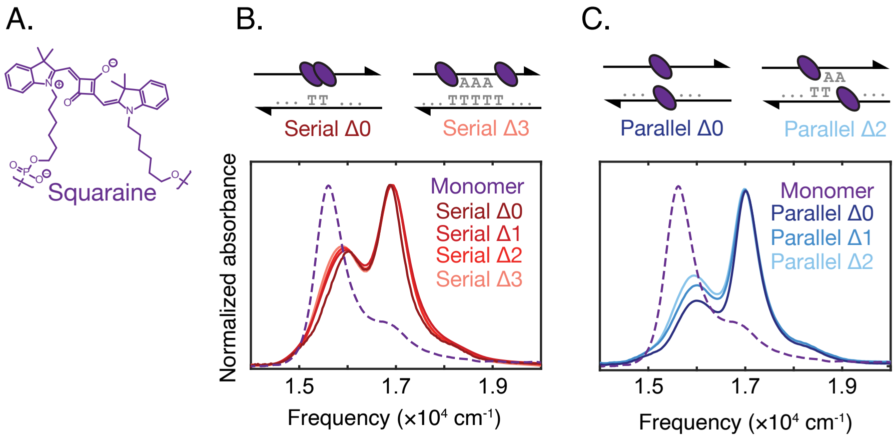

Figure 5-1: Squaraine dimers on DNA Duplex. (A) Chemical structure of phosphoramidite-modified squaraine. Schematic illustration (top) and absorbance spectrum (bottom) of the (B) serial and (C) parallel configurations defined in the text. Here, ΔX quantifies the number of nucleotides separating each dimer unit. For the Serial, the $\Delta 0$ and $\Delta 3$ configurations are illustrated, while Parallel we illustrate $\Delta 0$ and $\Delta 2$. Figure adapted from Ref. [71]

calculate both excitonic and charge transfer couplings in DNA-scaffolded dimers.

Ground-state MD simulations were performed in explicit solvent for a DNA fragment featuring squaraine dimers in either the serial or parallel $\Delta 0$ configuration. On the other hand, excited-state quantum mechanical calculations were performed on isolated dimer coordinates extracted from the MD simulations. Given that high-level quantum mechanical calculations do not converge for large molecular systems ($>$ 100 atoms), this combined strategy allows us to capture the effect of DNA-chromophore interactions arising from the different scaffolding patterns on the dimer electronic coupling. Snapshots from our MD trajectories are illustrated in Fig. 5-2B for the serial (top) and parallel (bottom) $\Delta 0$ configurations. The excitonic coupling was determined by explicitly calculating two-electron integrals between monomer transition dipoles obtained using time-dependent density functional theory (TDDFT) with the Tamn–Dancoff approximation (Eq. 5.2) [78, 152, 153]. Charge-transfer coupling was calculated from electron and hole transfer integrals via DFT calculations (Eq. 1.6). Computational details on the MD force field generation, MD simulations and excited-state electronic structure calculations are presented in the following sections.

Squaraine force field generation.

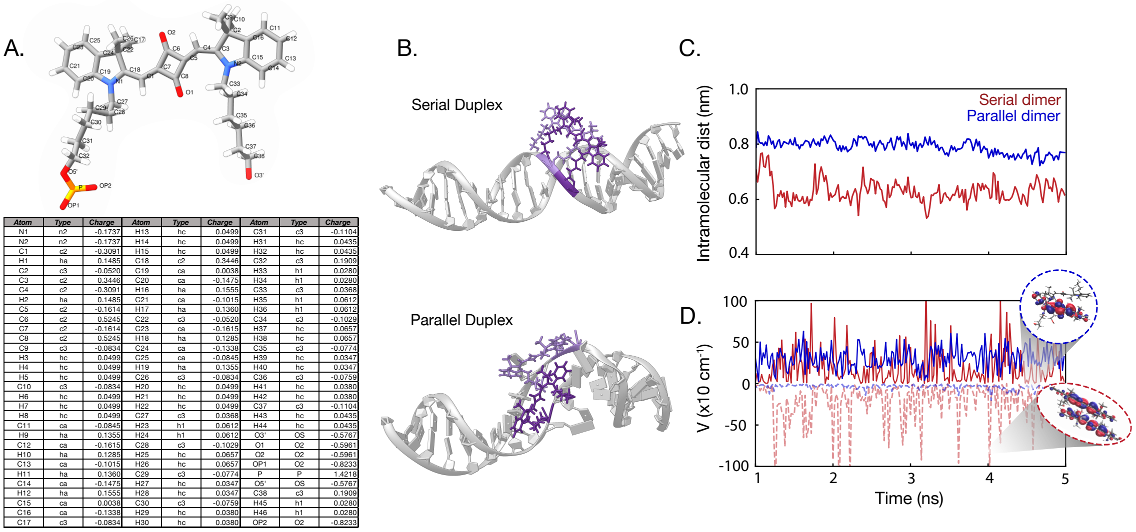

Atom	Type	Charge	Atom	Type	Charge	Atom	Type	Charge
N1	n2	-0.1737	H13	hc	0.0499	C31	c3	-0.1104
N2	n2	-0.1737	H14	hc	0.0499	H31	hc	0.0435
C1	c2	-0.3091	H15	hc	0.0499	H32	hc	0.0435
H1	ha	0.1485	C18	c2	0.3446	C32	c3	0.1909
C2	c3	-0.0520	C19	ca	0.0038	H33	h1	0.0280
C3	c2	0.3446	C20	ca	-0.1475	H34	h1	0.0280
C4	c2	-0.3091	H16	ha	0.1555	C33	c3	0.0368
H2	ha	0.1485	C21	ca	-0.1015	H35	h1	0.0612
C5	c2	-0.1614	H17	ha	0.1360	H36	h1	0.0612
C6	c2	0.5245	C22	c3	-0.0520	C34	c3	-0.1029
C7	c2	-0.1614	C23	ca	-0.1615	H37	hc	0.0657
C8	c2	0.5245	H18	ha	0.1285	H38	hc	0.0657
C9	c3	-0.0834	C24	ca	-0.1338	C35	c3	-0.0774
H3	hc	0.0499	C25	ca	-0.0845	H39	hc	0.0347
H4	hc	0.0499	H19	ha	0.1355	H40	hc	0.0347
H5	hc	0.0499	C26	c3	-0.0834	C36	c3	-0.0759
C10	c3	-0.0834	H20	hc	0.0499	H41	hc	0.0380
H6	hc	0.0499	H21	hc	0.0499	H42	hc	0.0380
H7	hc	0.0499	H22	hc	0.0499	C37	c3	-0.1104
H8	hc	0.0499	C27	c3	0.0368	H43	hc	0.0435
C11	ca	-0.0845	H23	h1	0.0612	H44	hc	0.0435
H9	ha	0.1355	H24	h1	0.0612	O3'	OS	-0.5767
C12	ca	-0.1615	C28	c3	-0.1029	O1	O2	-0.5961
H10	ha	0.1285	H25	hc	0.0657	O2	O2	-0.5961
C13	ca	-0.1015	H26	hc	0.0657	OP1	O2	-0.8233
H11	ha	0.1360	C29	c3	-0.0774	P	P	1.4218
C14	ca	-0.1475	H27	hc	0.0347	O5'	OS	-0.5767
H12	ha	0.1555	H28	hc	0.0347	C38	c3	0.1909
C15	ca	0.0038	C30	c3	-0.0759	H45	h1	0.0280
C16	ca	-0.1338	H29	hc	0.0380	H46	h1	0.0280
C17	c3	-0.0834	H30	hc	0.0380	OP2	O2	-0.8233

Figure 5-2: Combined molecular dynamics and quantum chemical approach. (A) Force field assignments for the phosphoramidite-modified squaraine molecule. Atom types and charges are listed at the bottom. (B) Snapshot of the equilibrated structures for the Serial Δ0 (top) and Parallel Δ0 (bottom) squaraine dimers scaffolded in DNA Duplex, that were simulated in this work. (C) Intradimer distance and (D) couplings as calculated for the serial (red) and parallel (blue) dimer trajectories generated. The excitonic and CT couplings are plotted in solid and dashed lines, respectively. A snapshot of the MO distribution at a configuration of minimum V_{CT} is also shown for both dimers in dashed-line circles.

Prior to the all-atom MD simulations, a force field (FF) was generated for the squaraine molecule and its hexyl linkers. The modified squaraine molecule was modeled using the Avogadro molecular editor (version 1.2.0) [7], and the geometry was optimized with the restricted Hartree-Fock (RHF) method and the 6-31G(d) basis set, as included in the Q-chem software [133]. The atomic point charges were generated with the AM1-BCC method [82] included in the Antechamber package [148]. The partial charges assigned to the phosphate group were chosen to resemble those found in the DNA backbone and the generalized Amber force field (GAFF) [149] was employed for all FF terms. The atom types and calculated charges are presented in Figure 5-2A, with the atom assignments indicated on the chemical structure.

All-atom molecular dynamics simulations.

The DNA-scaffolded dimer constructs studied in this chapter were prepared using the PyMol software [131], from the DNA duplex and squaraine optimized structures.

A B-form DNA duplex fragment with 21 base-pairs was modeled with the nucleic acid builder (NAB) from AmberTools [24]. Two DNA-squaraine complexes were constructed: a serial configuration, with each monomer replacing two consecutive bases, and a parallel configuration, with the monomers replacing a complementary base pair (Figure 5-2B).

All-atom molecular dynamics (MD) simulations were performed on the DNA-squaraine constructs using the software Amber18 [24] with the GAFF2 force field. The structures were solvated in TIP3P water molecules, using a distance of 12 Å with respect to the solvent box. Explicit Na^+ ions were added to neutralize the DNA, and Cl^- ions were added to set a concentration of 100 mM NaCl, mimicking experimental conditions. Periodic boundary conditions were applied to all MD simulations, and the SHAKE algorithm was used to constrain the H atoms to the equilibrium bond length. A 12 Å cutoff was used to calculate the Van der Waals energies, while The Particle Mesh Ewald (PME) method was employed to calculate full electrostatics. The simulations were carried out in an NPT ensemble using the Langevin thermostat for temperature control with a collision frequency of 5 ps^{-1}, and the Berendsen barostat for pressure control, with a reference pressure of 1 bar.

Minimization of the constrained system was carried out before the production simulation for 5000 steps. Then, the constrained system was slowly heated to 300 K for a total time of 20 ps and time-step 2 fs, and then left to equilibrate with constant temperature for 2 ns. The production dynamics were then generated at 300 K for a total time of 5 ns with a 2 fs time step, which is within the timescale where CT effects were detected in the experiment. The serial dimer simulations were performed on duplicate, while the parallel dimer coordinates were averaged over three trajectories for 5 ns each. The variation of the intramolecular distance was calculated as the center of mass distance for both types of dimers and averaged over the production replicates. The trajectories, shown in Figure 5-2C, were used as an indication of the stabilization of the dimer configurations.

Quantum mechanical calculations.

Charge-transfer coupling was calculated from electron and hole transfer integrals via

DFT calculations, according to Eq. 1.6) [152]. The coordinates of each squaraine molecule were extracted from the MD trajectories every 20 ps with the MDAnalysis package [110] (250 frames in total). Then, the phosphate groups in the squaraine linkers were replaced with hydrogen atoms, and DFT was performed with a 6-31G level of theory and implicit COSMO solvation using the PySCF package [141]. These results were employed to calculate V_{CT} as described in Section 5.2, while TDDFT/TDA was performed with a B3LYP functional to calculate $V_{\text{excitonic}}$. Other excited state properties needed to reproduce optical properties for squaraine were also calculated, namely, the excitation energy, transition dipole moment, and oscillator strength.

The variation of $V_{\text{excitonic}}$ and V_{CT} for the isolated monomer trajectories is shown in Fig. 5-2D. A snapshot of the serial and parallel dimer configurations at local minima points of V_{CT} are presented as insets in Fig. 5-2D, where the MO distributions were also calculated. Since the change in intermolecular distance remains fairly stable through the simulation (Fig. 5-2C), the variation in coupling likely comes from differences in the relative orientation of the monomers within a given range of intradimer separation.

5.5 Evaluating the Interplay between Excitonic and Charge Transfer Coupling.

Following the procedure detailed in the previous section, the excitonic and charge transfer coupling was calculated for the serial and parallel $\Delta 0$ dimer trajectories. The simulation resulted in long-range excitonic couplings, $V_{\text{excitonic}} = 207$ and $319\ \text{cm}^{-1}$, and short-range CT couplings, $V_{\text{CT}} = -199$ and $-45\ \text{cm}^{-1}$, for the serial and parallel $\Delta 0$ dimers, respectively. The 0–0/0–1 band ratio was calculated based on the average total coupling $V_{\text{excitonic}} + V_{\text{CT}}$ [71], and plotted against the experimental values in Fig. 5-3A. The total coupling strength for the parallel dimer is seen to be stronger than that of the parallel, which is consistent with the experimental measurements.

These differences in coupling can be explained by comparing the statistical distribution of the excitonic and CT coupling along the MD trajectories for the serial and parallel configurations (kernel density estimation (KDE) plots in Figure 5-3B and C, respectively). The KDE distributions show that while the excitonic coupling is on the same order of magnitude for both types of dimers, the CT coupling significantly is larger for the serial dimer. In fact, the sub-50 cm^{-1} CT coupling for the parallel configuration could be considered negligible if compared to the excitonic coupling, consistently in the 100 cm^{-1} order of magnitude. Thus, the excitonic coupling of the parallel $\Delta 0$ dimer can be adequately described using Kasha theory, which treats Coulombic interactions only, while a Hamiltonian describing the serial $\Delta 0$ dimer must include both Coulombic and CT contributions, *i.e.*, using the Hamiltonian in Eq. 1.3.

The magnitude of CT coupling in the serial dimer configuration also explains the differences in the 0–0/0–1 band ratio observed experimentally, despite both configurations sitting at similar intermolecular distances 5-2C. Based on the relative phase of the molecular orbitals for each monomer, we determined the charge-transfer coupling was negative, while the excitonic coupling was positive as expected for an H-type dimer. The opposite signs of the excitonic and charge-transfer couplings implies a destructive interference between these two contributions, which likely results in the larger total coupling for the parallel dimer observed in the absorption spectra.

The origin of the difference in CT coupling between the two dimers lies in their relative chromophore orientations. As shown in the insets of Fig. 5-2D, the serial dimer at a point of minimum V_{CT} adopts a π-stacked structure, while the chromophores in the parallel dimer are shifted by an angle. Sitting at a similar intermolecular distance, the "twisting" of the chromophores in the parallel dimer decreases the orbital overlap, compared to the serial's π-stacked configuration. On the other hand, horizontal displacement on the serial stacks will decrease the long-range electrostatic interactions while maintaining strong orbital overlap. It has been noted in previous studies with π-stacked aggregates that CT character is very sensitive to the relative orientation between chromophores (within the sub 5Å scale), and this behavior was observed here for squaraine dimers. We conclude that the parallel configuration selects for more excitonic and less charge-transfer character, whereas the serial configuration has near-equal couplings for both processes.

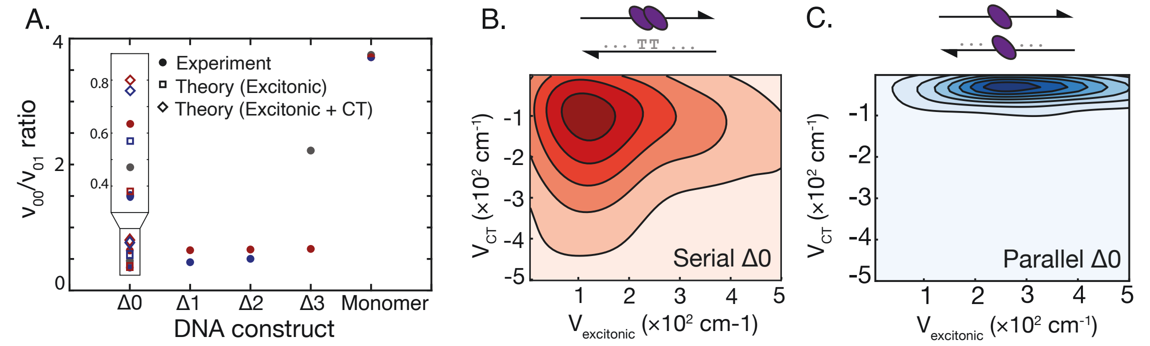

Figure 5-3: Excitonic and charge transfer coupling in squaraine dimers scaffolded in DNA. (A) Experimental molecular coupling as extracted from the vibronic peak ratio between the 0–0 and 0–1 bands ($\nu_{00}/\nu01$) in the absorption spectra, compared with the average theoretical values. Kernel density plot of the excitonic vs charge transfer coupling for the (B) serial (C) and parallel Δ0 dimers.

5.6 Intermolecular Interaction in Squaraine Dimers

The observed differences in the absorption spectra between serial and dimer configurations are attributed to variations in the balance between excitonic and charge-transfer couplings. However, this interplay cannot explain why the absorption band ratio seems to be unaffected by the imposed nucleotide spacing.

In addition to the short-range CT coupling, closely spaced chromophores experience attractive molecular forces. In particular, the electron polarizability of zwitterionic chromophores enhances their tendency for charge separation. In this section, we will further explore squaraine dimer interactions beyond charge transfer and examine their effect on DNA scaffolding patterns.

Destabilization of DNA double-chain.

We postulate that the constancy of the ν_{00}/ν_{01} band ratio with respect to nucleotide spacing originates from potent molecular forces within the chromophore pair, strong enough to induce conformational changes in the DNA double-strand structure.

Indeed, the absorption bad ratio observed in the parallel dimer also supports this theory. DNA Duplex's structure naturally pushes the bound dimers to angle outwards from the backbone, preventing steric interference between the sizable squaraine molecules (approximately ∼15 Å in diameter) and backbone atoms (Fig. 5-4A). Given the DNA double helix's 20 Å diameter, such an arrangement results in a significant interchromophore gap, leading to negligible coupling, as depicted in Figures 5-4D and E. Spectroscopic observations contradict this initial design since parallel dimers exhibit pronounced coupling —more than the serial $\Delta 0$ dimer which allows for intermolecular separations below approximately 7 Å, given a DNA base-pair distance of 3.4 Å. This initial design is not supported by spectroscopical observations, as parallel dimers show strong coupling, even more so than the serial $\Delta 0$ dimer, which allows for intermolecular separations below ~ 7Å given DNA base-pair distance is 3.4 Å. Hence, the coupling strength seen in the parallel dimer can only arise from DNA conformational changes allowing shorter inter-chromophore distances without steric interference with backbone atoms.

Considering the disparity between DNA equilibration timescales and CT effect detection timescales, we initiated the MD simulation in a high-energy structure, expecting the DNA to transition to its genuine equilibrium configuration within feasible computational timeframes. We probed configurations where monomers were positioned closer, anticipating the intradimer interaction would offset unfavorable DNA steric interactions. For instance, one initial condition positioned the molecules within the DNA's major grooves (Figure 5-4B). However, as depicted in Fig. 5-4E, this setup only slightly reduces the intramolecular dimer gap to the DNA's diameter, still resulting in negligible coupling.

Based on the arguments above, the only plausible configuration where the parallel $\Delta 0$ dimer would be separated by less than the DNA diameter would be if located inside the DNA backbone. In a double-chain structure, this configuration is extremely unstable and will lead to one of two energetic pathways: the restoration of the DNA structure with the chromophores being pushed back out of the backbone, or the breaking of DNA base-pair hydrogen bonds in order to accommodate the dimer. Initializing our MD simulations in this high-energy configuration led to the second equilibrium structure, as shown in Fig. 5-4C. This simulated trajectory yielded monomer-to-monomer distances closely resembling the serial dimer, with $V_{\text{excitonic}}$ aligning with experimental observations (Figures 5-4D and E). It is essential to recognize that both outward and inward configurations represent local energy minima of the chromophore-DNA structure, with the dimer's local environment and experimental conditions potentially guiding the system towards one of these configurations. Under the conditions studied here, the equilibrium configuration aligns with that of Fig 5-4C,corroborating experimental data.

To validate that squaraine dimer intermolecular interactions can enforce these DNA conformational shifts, we conducted umbrella sampling calculations on two squaraine dyes solvated in water to quantify their interaction strength.

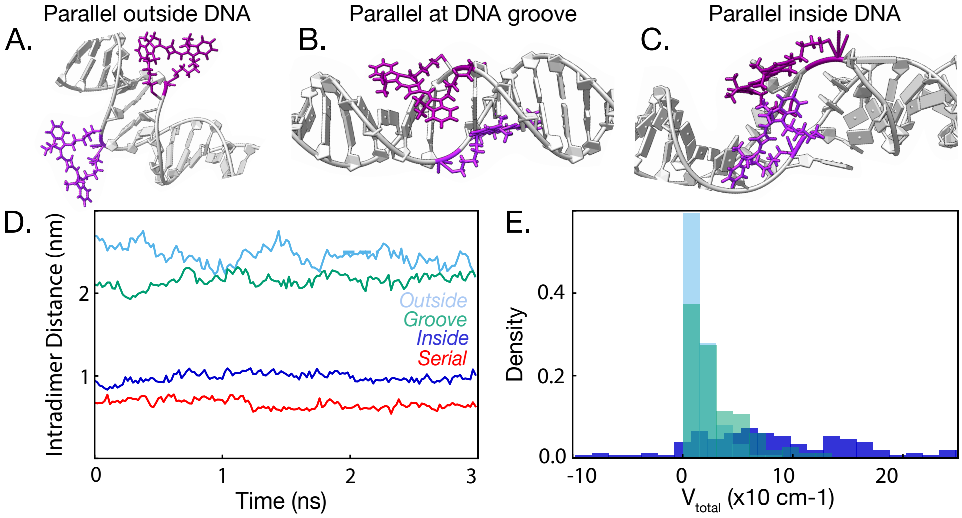

Figure 5-4: Intradimer interactions drive structural changes in DNA scaffold. (A) Molecular snapshots of the starting dimer-DNA scaffold structures tested to replicate spectroscopical observations. (B) Intradimer distances along the molecular dynamics trajectories when starting for the structures above, compared to the serial dimer. (C) Histogram with the total coupling distributions for each one of the starting structures.

Umbrella sampling calculation on isolated dimer.

The described rearrangement of the DNA duplex can only manifest if the squaraine monomer's intermolecular force is robust enough to break the hydrogen bonds connecting the base pairs. Specifically, squaraine aggregation-induced stabilization should surpass the destabilization caused by separating complementary base pairs.

We attempt to test the feasibility of the initial configuration chosen for the parallel $\Delta 0$ dimer by comparing the intermolecular forces of squaraine aggregation, with the DNA hydrogen bonding free energy, which is typically more dominant than base π-stacking energy [60]. If these values are comparable, we contend that the proposed structure (Figure 5-4A) is energetically feasible. WTo this end, we employed umbrella sampling (US) calculations on the isolated squaraine dimer to determine the potential energy surface (PES) associated with the dimer disaggregation.

Initially, we extracted the squaraine dimer's coordinates from the parallel Δ0 DNA-squaraine starting structure shown in Figure 5-2B after performing MD minimization. MD simulations were carried out in the isolated dimer solvated in TI3P explicit water, using the Amber18 software and the same FF from Fig. 5-2A. Following the protocol outlined in Ref. [144], a restrained minimization of the initial structure was performed for 5000 steps each, followed by 5000 steps of unrestrained minimization for the entire system, both with a 12Å cutoff. This was followed by an NVT heating of the solvent to 300 K, for 20 ps. Then, an NPT equilibration of the entire system was carried out by gradually reducing the imposed harmonic constrain on the system on 4 steps, with 30 ps each: from 50 to 10, 5 and 0 kcal $\text{mol}^{-1}\text{Å}^{-2}$. Finally, umbrella sampling was employed for the free energy calculation of the final equilibrated structure [126]. To construct the potential mean field (PMF) for squaraine aggregation, the dimer was constrained on a biased potential across a range of intramolecular separations with a harmonic restrain of 100 kcal $\text{mol}^{-1}\text{Å}^{-2}$. Here, the intramolecular distance was defined as the separation between the C7 atoms on each squaraine molecule, identified as the closest to the center of mass of the molecule. A total of 90 windows were constructed by varying the center of the biased potential from 3 to 12 Å, every 0.1 Å. For each window, a 2000-step minimization, 40 ps NPT equilibration, and 100 ps NPT production were simulated, with biased coordinates recorded every 4 ps of the production run (a total of 2500 recorded per window). Then, the WHAM algorithm [94], as implemented by Alan Grossfield [69], was employed to process the biased coordinates with a converged tolerance of 0.00001, and the free energy of aggregation was calculated from the obtained PMF (Fig. 5-5A). The WHAM result was tested for accuracy by manually calculating the PMF from each of the biased distributions, for each window, confirming the convergence of the code.

The potential energy surface for the dimer revealed an intermolecular interaction energy of $\Delta G\ = -4.6$ kcal mol^{-1} which is lower than the guanine-cytosine hydrogen bond strength ($\Delta G = -5.5$ kcal mol^{-1}) and slightly higher than the adenine-thymine hydrogen bond strength ($\Delta G = -4.5$ kcal mol^{-1}) under similar conditions [144, 60]. This suggests that the free-energy of intradimer interactions is sufficient to potentially disrupt the stability of base-pair interactions of DNA.

The stability of the proposed conformation in Fig. 5-4A is far too complex to be explained through mere base-pairing hydrogen bond strengths, as the placing of the dimer inside the duplex triggers a reconfiguration of all the adjacent nucleotide pairs, with varying stability outcomes, some becoming more stable than others. Our analysis suggests that intradimer forces are pivotal in shaping the spatial layout of strongly-coupled dimers

However, we believe our analysis highlights the critical role intradimer forces play in driving the spatial layout of strongly-coupled dimers. These results, in conjunction with insights from charge-transfer coupling effects, attempt to explain the complex interplay between long and short-range intradimer interaction in the strong coupling limit.

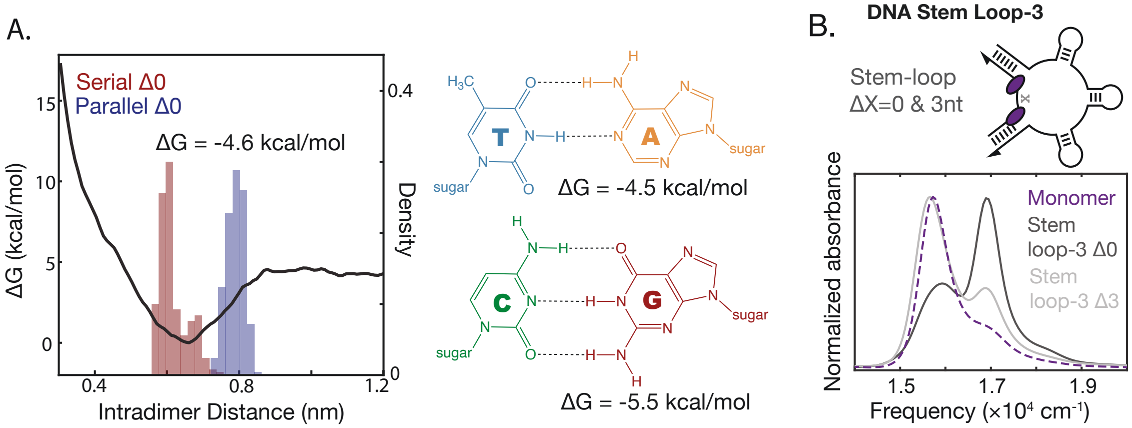

Figure 5-5: Quantifying interactions between squaraine monomers. (A) Calculated interaction potential energy surface for squaraine separation (black line) and distribution of squaraine dimer interchromophore distance for serial and parallel dimers as derived from the molecular dynamics simulations. The intermolecular interaction energy ΔG is included for reference and compared with those for the DNA base pairs under similar conditions. (B) Stem loop constructs synthesized experimentally and corresponding absorption spectra, with squaraines separated by 0 or 3 nucleotides ($\Delta 0$ or $\Delta 3$, respectively).

To further clarify the interactions within stacked chromophores at the strong-coupling limit that led to the observed pattern of coupling strengths, an alternative DNA structure was designed. The Stem Loop-3 construct (Fig. 5-5 was synthesized by pairing chromophore-containing serial strands with a Δn separation and complementary strands incorporating three loops. This DNA structure was built as a way to impose mechanical constraints in the DNA, hindering its structural reorganization and making interactions between squaraine pairs less favorable. This design choice is validated by the absorption spectra of the stem loop-3 DNA, which exhibited a reduced vibronic band ratio as the Δ nucleotide separation increased. Notably, at a separation of $\Delta 3$, the absorption spectra mirrored that of a monomer.

This chapter underscores the potential of DNA scaffolds in manipulating the photochemistry of strongly-coupled squaraine chromophores. Our exploration delved deep into the dynamics of interactions among closely-aligned chromophore pairs, focusing on the delicate balance between excitonic and charge-transfer interactions. It was demonstrated that chromophores can also exhibit attractive molecular forces that can potentially reshape the scaffold's architecture. In designing DNA-chromophore nanomaterials, it is imperative to consider all intermolecular interactions. This encompasses both charge transfer and molecular electrostatics, the latter influenced by the selected scaffolding pattern and also the inherent properties of the molecular chromophores.

Chapter 6

Relating Dimer Geometry with Optical Properties

6.1 Introduction

DNA nanotechnology offers exciting avenues for modulating photophysical properties via molecular design. In previous chapters, we delved into mathematical models and computational techniques to understand how circuit geometry affects interchromophore interactions. We saw that even a fundamental DNA architecture, like the double helix, affords great design adaptability. In particular, by positioning dimers on the same or opposing strands of a DNA duplex, we can tune exciton photophysical pathways [71]. DNA origami programmable structures can provide us with a broader design spectrum for exciton control compared to DNA duplexes, but a more profound grasp of the structure-property relationship in DNA nanostructures is still needed [72, 71].

Central to excitonic circuit design is mastery over exciton product states. An exciton may delocalize between chromophores or transform into free charge particles. The character of intermolecular interactions delineates the photophysical pathways available to an exciton. Electrostatic (or excitonic) interactions, for instance, facilitate electron transfer, while short-range interactions steer charge separation pathways [155]. As we learned in the previous chapter, varying geometries and DNA-scaffolding patterns can promote distinct interaction types. Yet, designing structures explicitly for specific product states remains a challenging task [155, 100].

This chapter aims to get a deeper understanding of the relationship between DNA, dimer geometries and exciton product states. I spotlight a system featuring Perylene diimides (PDIs) chromophore dimers scaffolded in DNA. PDIs are a class of dyes that can access a variety of product states, including symmetry-breaking CT and singlet fission [97, 100, 132, 155] Dimer configurations of these dyes have been reported to form excimers [100, 91]. Stemming from a superposition of Frenkel and CT exciton states, these product states are prevalent in the short-range domain [59]. Through DNA scaffolding, we aim to regulate excimer formation and exciton delocalization. To this end, we introduce a DNA origami structure and examine its influence on dye molecule positioning relative to the Duplex DNA explored in Chapter 5. DNA-origami constructs not only amplify our design space but also enable the scaffolding of higher chromophore counts, which is essential for designing extended circuits and enhancing signals through multiple pair repetitions [105].

In the following sections, I will analyze spectroscopical measurements provided by our experimental collaborators on PDI dimers scaffolded on DNA Duplex and a DNA origami structure. I will employ a similar combined MD and quantum mechanical approach to that used in the previous chapter. My focus will be on the characteristic geometries that will be imparted by the different DNA architectures and their implications for charge transfer and excimer formation in PDI dimers.

6.2 Studying Charge-Transfer State Formation in PDI dimers

A programmable DNA platform was employed by our collaborators to scaffold the PDI dimers. PDIs were attached to DNA through the backbone's phosphate groups and modified for increased solubility and to prevent dye aggregation. High-throughput synthesis methods were employed to produce the Duplex-DNA assemblies, including a structure with a PDI dimer in opposite strands (Opp-duplex), and a series of dimers in the same strand with increasing base-pair separation ([0,1,3,5]nt-duplex). These structures are illustrated in Fig. 6-1A.

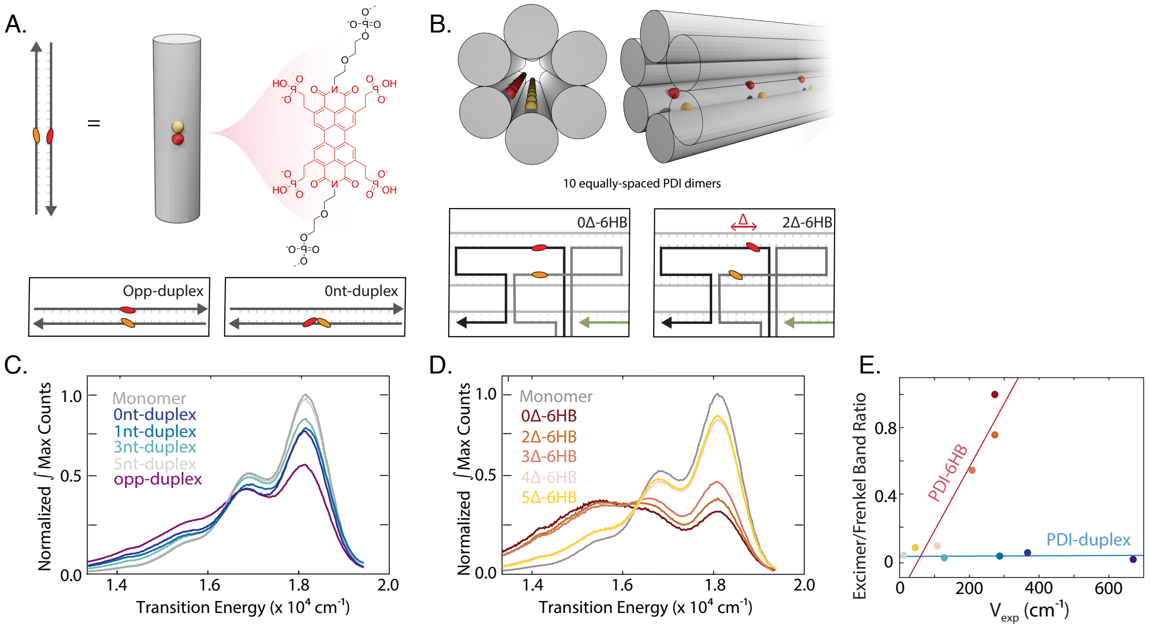

Figure 6-1: PDI dimers in DNA origami. (A) A dimer of modified PDI molecules (chromophore in red, linker groups in black) is attached to a DNA Duplex (here represented as a cylinder). Dimers are synthesized in parallel and serial configurations with no base-pair separation (labeled Opp-duplex and 0nt-duplex, respectively). (B) Illustration of the DNA-origami architecture made from a six-helix bundle (6HB). Each 6HB DNA contains 10 repeated units of the PDI dimer. The dimer is attached in the cavity in parallel, and with a separation of Δ base pairs. The 6HB-0Δ and 2Δ are shown at the bottom. (C) Emission spectra as measured for the Opp and the serial 0-5nt dimers. (D) Spectra for the 0-5Δ 6HB structures. The emission for the corresponding monomers is included in both cases for comparison. (E) Excimer/Frenkel band ratio plotted against the experimental coupling strength, as extracted from the emission and absorption spectra, respectively.

Although a similar strategy was employed to produce PDI-duplex aggregates to that used in the previous chapter for squaraine dimers, the dimer did not show strong interactions impeding the spatial separation of the dyes through base-pair insertion. The ability to separate chromophore units through nucleotide insertions adds to the programmability of the DNA scaffolds.

Besides double-stranded DNA, a higher-order DNA origami structure was also studied. A six-helix bundle (6HB) DNA architecture was chosen as a stable and robust platform that allows for the integration of multiple units of chromophore dimers. The ability to attach a large number of dyes is pivotal for the design of circuits that mimic Nature's machines, which can be composed of hundreds of precisely placed chromophore units [32, 130]. DNA-6HB structures were produced containing 10 repeated units of PDI dimers with varying separation ([0,2,3,4,5]Δ-6HB, see Fig. 6-1B). The separation between repeated units was large enough to guarantee no interaction between dimers.

The goal was that 6HB DNA-origami structures will induce CT and excimer formation in PDI dimers. Attaching the dimer in the inner cavity of the 6HB structure ($\sim$2 nm in diameter) should restrict dyes to the short-range coupling regime, facilitating the formation of a CT state. In order to test this hypothesis, the PDI-6HB and Duplex structures were studied with a combination of spectroscopical and computational methods. We sought to establish a difference in the nature of the coupling between the two DNA architectures and recognize the spatial patterns imposed by each one of these structures.

The absorption and emission spectra were measured by our collaborators for each one of the 6HB and Duplex structures (0–5 Δ-6HB, 0–5 nt-duplex and Opp-duplex), and their corresponding monomers. The emission spectra of the 6HB structures exhibit the characteristic band broadening of excimer states (Fig. 6-1C), which was not present in the Duplex constructs (Fig. 6-1C). Excimers are often dubbed self-trapped states ... the emission spectra indicate the formation of excimers in the 6HB 0–3Δ dimers. To further compare the photophysical properties of these two DNA structures, the Excimer/Frenkel band ratio was extracted from the measured emission bands and plotted against the coupling strength, as calculated from the ν_{00}/ν_{00} absorption band ratio. The Excimer/Frenkel ratio indicates the formation of excimers in the PDI-6HB, which increases for smaller nucleotide separations and chromophore interaction strength. On the other hand, Duplex PDIs present negligible excimer populations, although decreasing dimer separation leads to larger increments in coupling strength compared to the 6HB dimers. Stronger coupling in the Duplex constructs is an indication of either shorter chromophore separations or stronger and destructively interfering CT-mediated interactions, as seen in Chapter 5.

Further understanding of the complex interplay between short and long-range interactions in PDI dimers requires computational modeling. In the next section, I describe the simulation of the DNA constructs aimed to uncover the structural differences of the 6HB and Duplex constructs and how they relate to their observed optical properties.

6.3 Computational Methods

To devise the interplay between charge-transfer and excitonic coupling in PDI dimers on different DNA scaffolds, we carried out simulations in selected 6HB and Duplex constructs: The 0 and 2 Δ-6HB, and the 0nt and Opp-duplex dimers. Larger separations in 6HB dimers display negligible coupling strengths according to the absorption spectra and, therefore, were not analyzed further. A combined MD and quantum mechanical strategy akin to that in Sec 5.4 was employed. Additional details are presented next.

Molecular simulations.

All-atom MD simulations were carried out by our collaborators in the two 6HB and the two Duplex constructs. The force field for the PDI molecule with the linker attachments was parameterized following a similar strategy to that of the previous chapter. The modified PDI-linker molecules, however, required a fragmentation approach given the size of the system [66]. The molecule was fragmented into three separate residues, with each of these capped with appropriate chemical groups matching the charges present in the original bonds. Each residue was parametrized separately using the GAFF and with the atomic charges calculated via RESP fit.

The B-form of DNA was employed for the duplex structure, and built using the nucleic acid builder (nab) as implemented in AmberTools21 [25], while the 6HB DNA origami structure was generated using caDNAno2 [49]. The geometry-optimized PDIs were scaffolded manually on the corresponding positions for the Duplex and 6HB structures. For the large PDI-6HB origami, simulations were performed using short 42-

bp sections containing a single PDI pair—in contrast to the 10 repetitions implemented experimentally—to reduce computational cost. The simulated constructs for the 0Δ and 2Δ-6HB are presented in Fig. 6-2A and B, while the 0nt and Opp-duplexes are shown in Fig. 6-2C and D.

Molecular simulations were carried out in explicit TIP3P solvent, with $MgCl_2$ added to neutralize the system and to reflect experimental conditions (12 mM $MgCl_2$). A truncated octahedron with 10 Å cutoff distance was used to solvate the duplexes, while a cuboid box with 10 Å distance to the sides perpendicular to the rod axis and 0 Å along the 6HB axis was employed for the 6HB structures. We also set periodic boundary conditions, such that the solvation box would mimic the length and rigidity of the DNA rod prepared experimentally.

The all-atom MD simulations were performed in Amber16, using The OL15 FF for the DNA residues and GAFF for the PDI residues. Each DNA-dimer system was initially minimized in two steps: first with constraints placed on the dyes and DNA ((500 kcal mol^{-1} $Å^{-2}$), and then unrestrained, each for 5000 steps. This was followed by an equilibration from 0 to 300 k with weakly position restrains (10 kcal mol^{-1} $Å^{-2}$) for 20 ps and an unconstrained equilibration in a NPT ensemble at 300 K and 1 bar for 200 ps. Finally, production runs were performed for each system in a NPT ensemble at 300 K and 1 bar for 100 ns in triplicate. A time step of 2 fs was used for all MD simulations.

Quantum mechanical calculations.

We evaluate the nature of chromophore interactions in the 6HB and Duplex constructs by using the expanded CT Hamiltonian introduced in Sec. 5.2.

The excitonic coupling is calculated from the two-electron integrals in Eq. 5.2. On the other hand, we characterize CT interactions via DFT calculations using the Frontier Molecular Orbital (FMO) approach[142]. We start by describing the transfer of a single electron and hole between the donor (D) and acceptor (A) molecules.

Respectively,

$$\begin{aligned} D^{-}A &\longrightarrow DA^{-} \\ D^{+}A &\longrightarrow DA^{+}. \end{aligned} \tag{6.1}$$

We integrate between the initial and final states in 6.1 to get the corresponding CT integrals, t_e and t_h:

$$\begin{aligned} t_e &\equiv \langle D^{-}A|\hat{h}|DA^{-}\rangle = \langle \varphi^{D}_{\mathrm{LUMO}}|\hat{h}|\varphi^{A}_{\mathrm{LUMO}}\rangle \\ t_h &\equiv \langle D^{+}A|\hat{h}|DA^{+}\rangle = \langle \varphi^{D}_{\mathrm{HOMO}}|\hat{h}|\varphi^{A}_{\mathrm{HOMO}}\rangle. \end{aligned} \tag{6.2}$$

Where $\hat{h}$ is the Kohn-Sham operator for the DA dimer. We have also defined the charge-localized dimer states in terms of monomer HOMO and LUMO orbitals $\varphi^{i}_{\mathrm{HOMO[LUMO]}}$, with $i = D, A$. Because the HOMOs and LUMOS of separate molecules are not guaranteed to be orthonormal, we apply a Löwdin symmetry transformation to the integrals in 6.2,

$$\tilde{t}_{e[h]} = \frac{t_{e[h]} + \frac{1}{2}(\varepsilon^{D}_{e[h]} + \varepsilon^{A}_{e[h]})S_{e[h]}}{1 - S_{e[h]}} \tag{6.3}$$

where $\varepsilon^{D}_{e} = \langle \varphi^{D}_{\mathrm{LUMO}}|\hat{h}|\varphi^{D}_{\mathrm{LUMO}}\rangle$ is the site energy for the LUMO of monomer D, and $S_{e[h]}$ is the spatial overlap between the LUMOs[HOMOs] of D and A. We can then calculate the CT coupling using Eq. 1.6, where The CT-FE energy difference is calculated from the binding energies as in the previous chapter, $\Delta E_{\mathrm{CT-FE}} = U(0) - U_{\mathrm{CT}}$.

The coordinates of each PDI dimer were extracted from the MD trajectories every 20 ps for the last 2 ps for each trajectory (a total of 100 frames per dimer configuration). The MD Analysis tool [67, 110] was employed to extract the coordinates for the PDI and two linkers separately. In order to perform the quantum mechanical calculations the phosphate ends were capped with hydrogen. The alkyl chains on the linkers were kept in the capped structure to maintain the properties of the molecules as much as possible without the need for prohibitively expensive quantum mechanical calculations.

Furthermore, to avoid minimizing the PDI monomers at each step of the simulation and to conserve the distinct molecular configuration resulting from the DNA scaffolding,

Table 6.1: Calculated average coupling values from combined QM-MM simulations.

Sample	$V_{\text{excitonic}}$/ cm^{-1}	V_{CT}/ cm^{-1}	V_{total} / cm^{-1}
0Δ-6HB	554.30	-147.95	406.35
2Δ-6HB	598.93	-49.68	549.25
0nt-duplex	779.97	-53.83	726.14
opp-duplex	660.25	-43.05	617.20

the capping H was placed in the coordinates of the linker group to be replaced, with the bond length adjusted accordingly (*e.g.*, d[C-H]=1.09Å and d[O-H]=0.97Å.

DFT was performed for the separate PDI monomers of each dimer configuration, at the cc-pVDZ level of theory and implicit COSMO solvation using PySCF [141]. The excitonic coupling, $V_{\text{excitonic}}$, was calculated according to equation 5.2, where TDDFT/TDA was performed with a B3LYP functional to calculate the Coulomb and exchange integrals corresponding to the first excited state. On the other hand, the CT coupling V_{CT} was calculated with equation 1.6. The Löwdin symmetry transform (Eq. 6.3) was employed to calculate the electron and hole transfer integrals of the DA dimer, as implemented in the Q-chem software [133]. The CT coupling was set to destructively interfere with the excitonic coupling in all cases to match the total coupling observed in the experiments.

Figure 6-2A and B show the evolution of $V_{\text{excitonic}}$ and V_{CT} for 0Δ and 2Δ-6HB across the MD trajectory, and Fig. 6-2C-D shows the results for the duplex trajectories. Calculations for the 3Δ-6HB showed negligible coupling and results are omitted here. The average coupling values for all structures are presented in Table 6.1.

6.4 Differences in Molecular Coupling Explained by Geometrical Features

Our calculations show a strong CT character in the 0Δ-6HB dimer and weak for the 2Δ and the duplexes. Furthermore, the excitonic coupling seems to be larger for the duplexes. Due to excitonic-CT destructive interference, the total coupling is also stronger in the 0nt and Opp-duplex, which reproduces the patterns extracted from

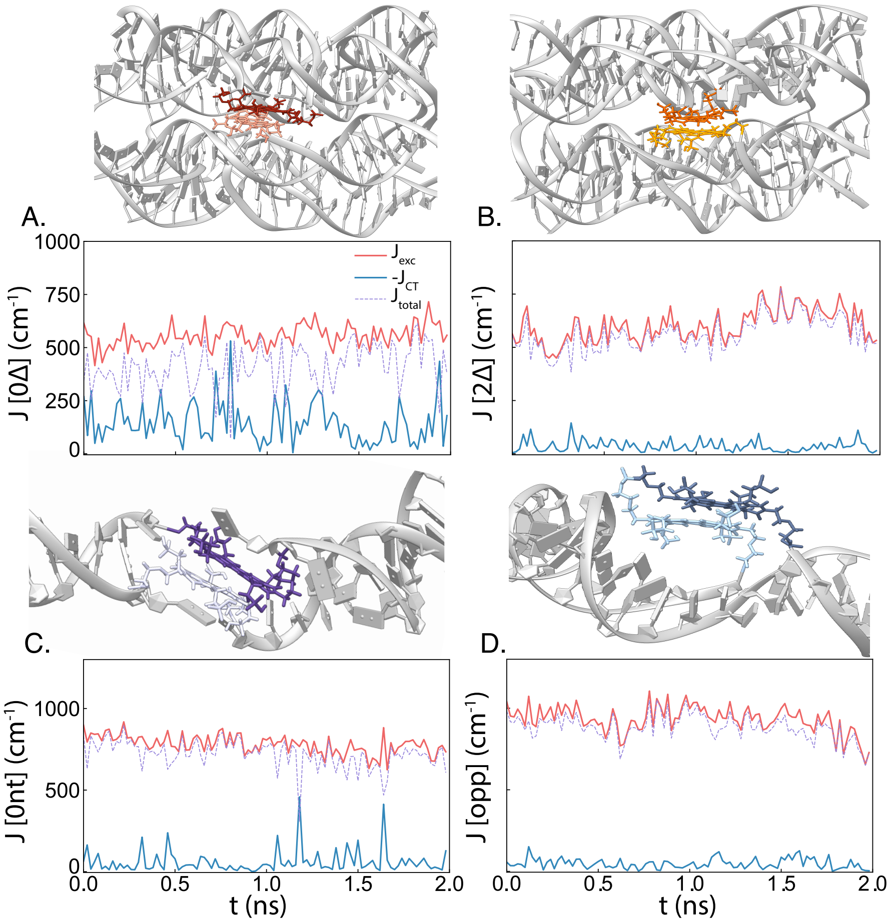

Figure 6-2: Results from molecular simulations on the PDI dimer constructs. Snapshot of simulated structures for the 6HB DNA-origami and calculated coupling for the last 2 ns of simulation for a (A) Δ0 and (B) Δ2 separation. Simulated structure and calculated coupling for the Duplex (C) 0nt (serial with no separation) and (D) Opp (parallel with no separation).

the absorption spectra. The CT character in the PDI-6HB agrees with the reported Excimer/Frenkel ratio as well. Some differences with the experimental coupling are remarked, namely, the Opp-duplex should exhibit the strongest coupling, while in our computational results, it was the 0nt construct. Stronger interactions for the Opp dimer should either arise from shorter interchromophore distances that were not captured on the MD trajectories or from a strong and destructively interacting CT coupling in the 0nt structure, also not captured in our simulations. The CT character of the Δ2-6HB is also not captured in our simulations, likely due to insufficient sampling.

In order to understand the interaction patterns of PDI dimers and how they relate to the DNA scaffold as seen in our simulations and experimental measurements, we now investigate the dimer geometries and how they relate to these observations. In our analysis, we will only focus on the 0Δ-6HB, 0nt-duplex and Opp-duplex constructs, presuming the 2Δ-6HB structure should have similar patterns to the 0Δ. For the last 2 ns of each dimer MD trajectory, the center of mass distance and angular displacement between PDI molecules were calculated for the same simulation frames in Fig. 6-2. The angular offset can be defined by considering a vector spanning the two opposite N atoms in the PDI ring, roughly aligning with the dipole moment vector. The displacement is calculated as the angle between the N-N vectors in the PDI dimer.

We noticed significant variations between the distributions of angles and distances of the studied constructs (6-3). In terms of separation, the duplexes and 0Δ-6HB dimers presented predominant short π-stacking distances between $\sim$ 4 and 6Å, typical of aggregated PDIs [23]. The distribution of the origami 0Δ-6HB was particularly narrow within that range, while that of the 0nt and Opp-duplexes show different populations. In each case, the population with less frequency corresponds to one of the three MD trajectories deviating from the average behavior. We also recognize different patterns in the angle offset. In particular, the duplex dimers showed relatively small rotational offsets, of 37 ± 6 and 17 ± 5 respectively, reflecting a nearly parallel alignment. On the other hand, the 0Δ-6HB construct was offset by about 60 . The large offset in origami dimers can be attributed to the attachment of PDIs in two neighboring helices, compared to the same helices in duplexes. Added to the rigidity of the 6HB structure, this leads to the imposing of spatial constraints on the PDI dimer that hinders it from reaching a π-stacked geometry. The rigidness of 6HB dimer configuration may also lead to the more homogeneous distribution observed.

Based on the calculated total coupling values, we also identified the PDI structures that most closely resemble experimentally observed properties. Specifically, matching the strength of the coupling with respect to the V_{exp} observed in the absorption spectra. We note that the total coupling measured is a result of an average observation of both monomer and dimer subpopulations present in the experiment at different degrees,

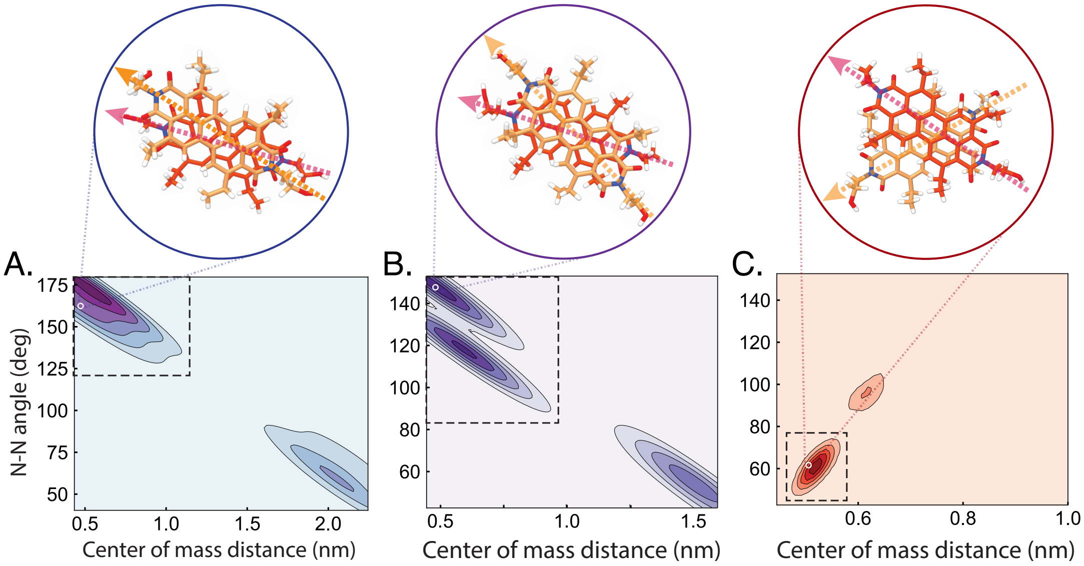

Figure 6-3: Geometrical patterns induced by DNA scaffolding. Density plot for the center of mass distance vs relative angle between PDI molecules, as extracted from the molecular dynamics simulations, for the (A) 0nt-duplex (B) Opp-duplex and (C) 0Δ-6HB dimers. Dimer configurations where the DFT-calculated coupling more closely matches experimental values are circled in white. These configurations are also illustrated on the top insets. The boxed areas indicate the populations that are both most frequent and closer to experimental values.

so an exact match between theory and experiment is not possible without careful consideration of monomer and dimer ratios. Therefore, we only determine the structure that we expect to be predominant according to the experimental observations. These dimer configurations are indicated with a white circle in the distribution plots of Fig. 6-3, and are illustrated as insets. The experimental configurations show rotational offsets of 62.2° and 31.1°for 0Δ-6HB and Opp-duplex, respectively.

To determine whether there is a relation between the structural patterns and the intermolecular coupling, we calculate the distribution of V_{exc} and V_{exc} for the population closest to the experiment configuration (boxed area of Fig. 6-3). Histograms displaying the coupling for the 0nt, Opp and 0Δ-6HB are shown in Fig. 6-4, with the total V_{T} as red dashed overlay. We can see that the coupling distributions correlate very closely with the geometry distribution, with the bimodality of the Opp-duplex geometries also present in the couplings. This is an indication that the observed interactions are a direct consequence of geometrical patterns in the dimer constructs and that these patterns are also related to different choices of DNA scaffolds and attachment points. Notably, the CT distribution in the duplexes sits narrowly around 0, while 0Δ showcases a significant number of configurations with V_{CT} between 0 and -1000 cm^{-1}. A stronger and destructively interfering CT coupling also leads to an overall decrease in the total interaction, as evident in a lower V_{exp} and seen for squaraine dimers in the previous chapter.

We also note the excitonic coupling is slightly larger for the duplexes, especially for one of the populations in the Opp-Duplex dimer. This strongly-coupled population contains the configurations that most closely match our experimental results. The short intermolecular distances and π-stacked configurations observed in the duplexes would lead to stronger electrostatic interactions.

Because the center-of-mass distance is comparable on all three constructs, we trace the variations in coupling to the N-N rotational offset. Previous studies have associated large rotational offsets in PDI dimers with an increase in CT character and excimer emission. Specifically, a conical intersection was predicted at an angle of ~60°, between the symmetry-allowed (upper) Frank-Condon state and the symmetry-forbidden (lower) state from which excimers decay [56]. This observation corresponds to the increase in the calculated CT in the heavily-rotated 6HB dimer, and the broadening of the emission spectra seen experimentally.

To corroborate there exists such a correlation between the NN-angle and the increase in CT and excimer character, we calculated V_{exc} and V_{CT} for a pair of geometry-optimized PDIs. We constrained simulations to a 4.0 Å center-of-mass distance and varied the NN rotational angle (Fig. 6-4D). The NN angle was screened from 0 (parallel dyes) to 90° (orthogonal dyes) and the resulting coupling is shown in Fig. 6-4E. As expected, the excitonic coupling decreases monotonically from a maximum at 0° to a minimum at 90°. Parallel dyes are known to have stronger electrostatic interactions as transition dipole moment vectors are aligned, and weaker or null interactions when the dipole vectors become orthogonal (Eq. 2.1).

The CT coupling, while also decreasing with rotational offset, presented a non-monotonic decrease. The resulting V_{CT} was highly sensitive to the molecular packing geometry, as it relies on molecular orbital overlap between neighboring molecules. A maximum of V_{CT} is seen at 0° when PDIs are aligned, as parallel π-stacking leads to near-perfect MO overlap, and falls to zero when PDIs are orthogonal and MO overlap is minimized. The CT coupling also decreases consistently up to an angle of ∼30°, but then increases again to a local maximum at ∼65°. This local maximum coincides with a slight alignment of the aromatic rings.

The changes in V_{exc} and V_{CT} with displacement angle coincide with patterns of geometry and coupling observed in the simulated PDI-DNA constructs. For visualization purposes, the distribution of NN-angles for the 0nt-duplex, Opp-duplex and 0Δ-6HB is also displayed in Fig. 6-4E. We can see that the 0Δ-6HB angle distribution is roughly centered around the local maxima of the CT coupling, which further confirms the increase in CT character and excimer populations seen in our simulations and the experiment On the other hand, 0nt distribution sits around small angles of rotation, which translates to a stronger V_{exc} and slight CT coupling, while the Opp-duplex sits almost exactly on the local minimum of V_{CT}. This matches the observation of neither of the duplexes presenting significant excimer emission. Furthermore, the fact that the 0nt-duplex dimer configurations exhibit slightly stronger CT than the Opp-duplexes, could be the origin of the reduced total coupling for the 0nt, if the short and long-range interactions are destructively interfering as proposed before. We can also theorize that the reason behind the excimer emission on the 0Δ-6HB lies in the comparable strengths of V_{exc} and V_{exc} at the local maxima of ∼65°, which could possibly facilitate Frenkel and CT exciton mixing.

Overall, in this chapter we were able to identify patterns in the excitonic and charge-transfer couplings of PDI dimers scaffolded in different DNA structures, and associate them to geometrical features imposed by local spatial constrains of the DNA scaffolds. In particular, 6HB origami structures can be employed to program charge-transfer character in chromophore dimers. The rigidity of the 6HB imposes a significant rotational offset in the chromophore pair with high fidelity. This programmability could be used to induce excimer formation or SBCT states in chromophore aggregates. Importantly, by understanding the correlation between DNA structure, local dimer geometry and chromophore interactions we could design materials with programmable photophysics with accuracy only comparable to Nature's biosconstructs.

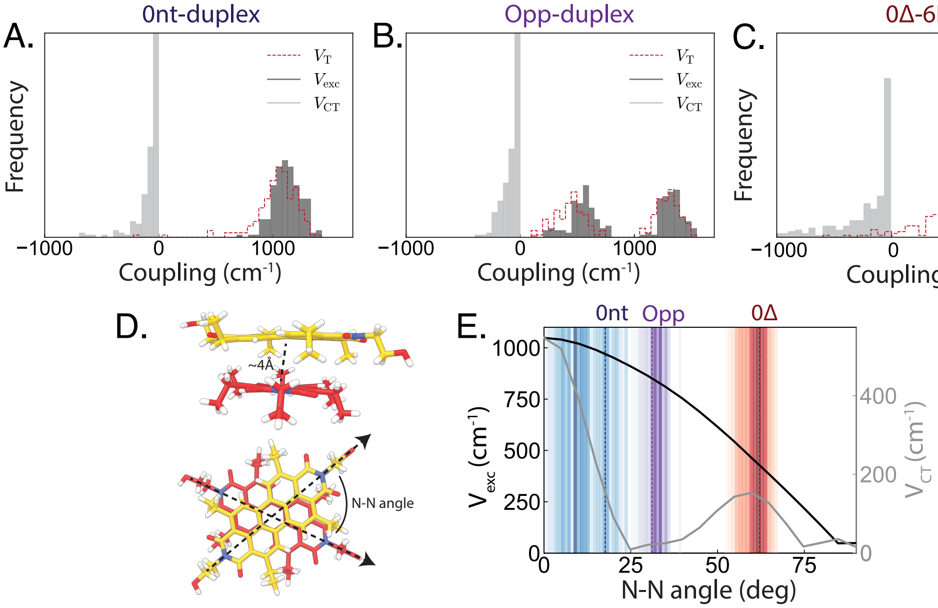

Figure 6-4: Relationship between imposed scaffold geometry and interchromophore coupling. Histograms for the excitonic and charge-transfer coupling calculated for the boxed configurations in Fig.6-3 for the (A) 0nt-duplex (B) Opp-duplex and (C) 0Δ-6HB dimers. The total coupling ($V_{\mathrm{exc}} + V_{\mathrm{CT}}$) is shown in red dashed lines. (D) The coupling is calculated for different N-N rotation angles for a PDI dimer fixed at a center of mass distance of 4 Å. (E) The couplings V_{exc} and V_{CT} are calculated from 0 to 90° angles.

Chapter 7

A Computational Strategy for the Design of Exciton Circuits with Programmable Properties

7.1 Introduction

In the two previous chapters, we learn that DNA scaffolding can control the photophysics of chromophore aggregates. The defining features of these properties originate from the interplay between short and long-range chromophore interactions For instance, long-range interactions regulate exciton delocalization and transfer amidst neighboring chromophores, whereas short-range interactions promote exciton evolution into charge-separated states. Long-range, or excitonic coupling, is largely influenced by electrostatic forces and thus depends on the distance and alignment of transition dipoles. In contrast, short-range CT interactions, emerging from the overlap of neighboring molecular orbitals, are particularly sensitive to even minor shifts in chromophore orientation [79].

Nature, as we have seen, has honed this mechanism over time. Plants efficiently control the spatial arrangement of chromophores within a sub-Å range, ensuring optimized exciton transport and charge separation across extensive molecular networks

[130]. This remarkable precision is attributed to the meticulous structure of protein scaffolds in the light-harvesting complexes. Attempting to emulate such precision with DNA nanostructures is undeniably challenging.

Our previous discussions underscored the potential of DNA architectures in directing exciton transport and evolution within chromophore circuits. In Chapter 5 we discerned how varied attachment paradigms can encode CT characteristics in squaraine dimers and, in Chapter 6, demonstrated how DNA origami structures can enhance our selectivity for CT coupling and mixed CT/Frenkel states. Different architectural choices lead to unique geometric features within chromophore dimers, which in turn influence the nature of the interactions observed. For a truly programmable excitonic platform, it is imperative to identify and fabricate the specific chromophore-DNA configurations that yield the desired photophysics.

Thus far, our approach has relied on experimental data on already tested dimer constructs which we then analyze via computational simulations. However, there are practical limitations to the number of DNA-dye structures that can be synthesized and characterized experimentally, even with state-of-the-art high-throughput techniques [40, 104]. Given these constraints, leveraging our accumulated knowledge to craft an efficient computational methodology seems to be the logical next step. This approach would guide experimental efforts towards the most promising structures, likely having the desired excitonic properties.

In this chapter, I present a high-throughput computational framework aimed at screening chromophore scaffold configurations with specific optoelectronic properties. This software will allow for the evaluation of a plethora of configurations, by harnessing the strengths of both MD and quantum mechanics as in previous chapters. However, it distinguishes itself by navigating the configuration space more efficiently, leveraging approximations and automation. We will initially focus on Cy3 dimers scaffolded in DNA Duplexes, a system with ample computational and experimental documentation, fitting as the first application of our software [41, 93, 72, 73].

Although several methods have employed quantum mechanical/molecular mechanical (QM/MM) approaches to examine the electronic properties of disordered systems

[109, 118, 119, 135], and there are a number of packages for both MD and excited state calculations in organic molecules [26, 141, 133], to our knowledge, none of these techniques provide a cohesive bridge between the classical and quantum components. Our software seeks to provide this integration, which is crucial for a comprehensive exploration of all potential dimer configurations within DNA structures. We have simplified the MD simulation to capture only the dimers' local environment and extract patterns of geometries across all samples. By correlating these patterns with changes in interchromophore coupling, as previously discussed in Chapter 6, we can identify DNA-chromophore constructs with the desired properties on a broader scale.

The following section will introduce our strategy for geometry screening using a QM/MM approach. Next, I will provide a detailed walkthrough of our algorithm, followed by a practical application on a subset of Cy3 dimers embedded in DNA duplexes.

7.2 Workflow for the High-throughput Screening of Excitons in DNA Structures

Molecular dynamics and excited-state electronic structure can be employed to capture the dynamics of excitons in molecular nanostructures. In particular, the statistical mechanics of the system are investigated using ground-state MD simulations, whereas exciton interactions are deciphered using quantum mechanical calculations. This methodology has been successful in the analysis of free chromophores in solution[77, 79, 132] and in the context of interacting chromophores with fixed orientations [28].

Notably, MD simulations become computationally demanding for extensive molecular systems, such as DNA scaffolds [71, 72]. To provide perspective, simulating DNA constructs comprising 22 to 30 base pairs can extend from a few weeks to several months, contingent on the simulation setup. Consequently, our methodology has predominantly focused on the computational examination of previously characterized DNA constructs. This approach constrains our exploration to a limited subset of

DNA structures and configurations, hindering a comprehensive exploration of the configurational space. Moreover, constraints on the number of replicates, coupled with poor statistics and energy sampling, have occasionally led to discrepancies with experimental results. These discrepancies often manifest due to simulations not converging to the energy minimum conformation [72] or resulting in the prediction of local minima configurations (Chapter 6).

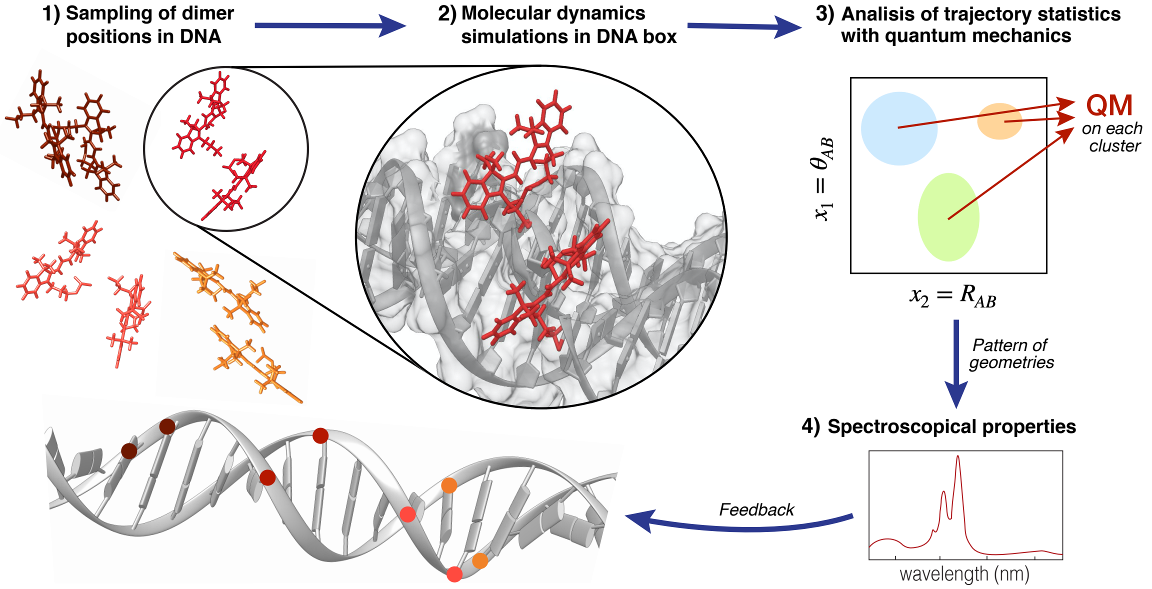

Figure 7-1: Methodology for the screening of dimers in DNA nanostructures.

To navigate these challenges, and with the aim of employing theoretical simulations as a roadmap to guide experiments, we designed a high-throughput computational workflow for the investigation of exciton dynamics in DNA-scaffolded chromophore circuits (Fig. 7-1). This comprehensive workflow encompasses four general steps:

1. Sampling of chromophore dimer positions within a full-length DNA construct.
2. Conducting MD simulations of these samples in a truncated DNA scaffold environment.
3. Employing quantum mechanics to analyze trajectory statistics.
4. Undertaking synthesis and spectroscopic characterization of promising candidates.

This protocol harnesses approximations and automation to efficiently simulate numerous dimer configurations within a selected DNA structure and chromophore. The remainder of this section will briefly describe the steps we follow to implement an efficient search in the chemical and structural space of both chromophores and DNA scaffolds. Computational details of our package, built in a Python environment, are presented in the next section.

0) Force field preparation

Before initiating the sampling process, we develop a force field for the dye, drawing parallels to strategies deployed in previous chapters but with enhanced automation. This refines the procedure, accommodating a broader chemical space of dye molecules and linker combinations. Our strategy consists of building the dye and linker FF separately, starting from a geometry-optimized structure for each where we have capped them with a chemical group mirroring the charge of the other entity. This modular approach (illustrated in Figure 7-2A) facilitates the simulation of larger dye molecules, especially since the calculation of partial charges restricts the system size to about 70-80 atoms—even with semi-empirical methods. Additionally, this automated process enables us to experiment with diverse dye and linker combinations, thereby expanding the available chemical space.

Notably, this process assumes that chromophore atoms and bonds primarily adhere to standard conventions, aligning with the generalized Amber Force Field (GAFF) [149]. Non-standard atom types and bonds, although infrequently reported in DNA origami circuit literature [149], would necessitate manual tweaks in the dye force field.

1) Sampling of dimers in DNA.

Having defined the FF for the dye/linker molecule, we aim to comprehensively sample potential attachment points for a homodimer of the modified dye. Our workflow caters to dyes with dual attachment points, implying that they bind to the DNA backbone at two successive nucleotides via individual linker groups. Finding all possible ways to place a doubly attached dye in a DNA scaffold with n nucleotides (assuming all nucleotides are viable for linker attachment) results in a total of ${}^{n-1}C_2$ possible configurations. Placing a second dye now adds ${}^{n-1}C_2 \times {}^{(n-2)-1} C_2$ more

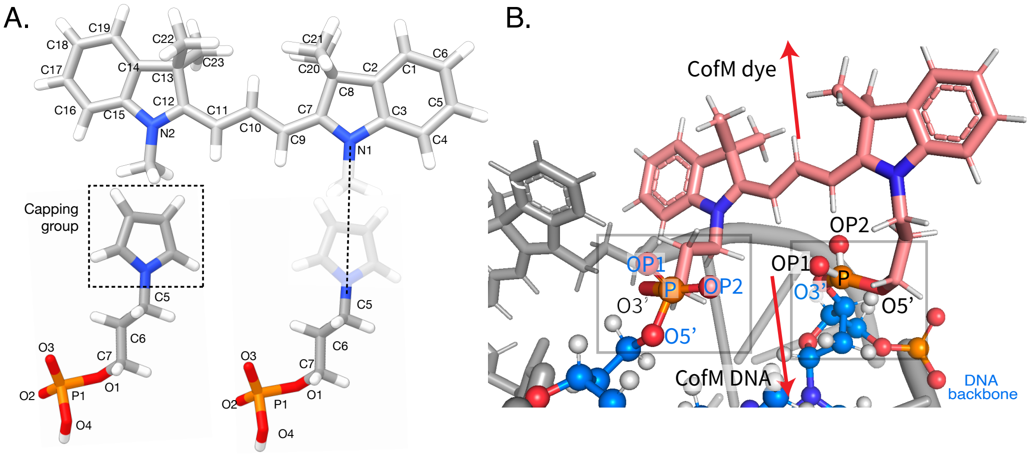

Figure 7-2: Preparation of the force field and DNA attachment of a Cy3 dye. (A) Dye and linker force fields are prepared separately and the molecules merged in a subsequent step. (B) The dye is attached to the DNA backbone via phosphate links. An anti-parallel alignment of the backbone and dye center of mass is enforced to reduce the possibility of steric clashes.

configurations, which for a 40-nucleotide DNA duplex strand results in up to 493,506 potential combinations. Simulating all of these combinations, even with approximated methodologies, is unfeasible. However, not all of these pairs will lead to significant exciton transfer, as pairs separated by more than 4 nucleotides usually display monomer-like photophysics.[72]. By focusing on dye pairs separated by less than a certain intermolecular distance, we can filter out inconsequential configurations, narrowing down the number of necessary simulations to around 100 for a 40-nucleotide duplex.

Dyes bind to the DNA through the backbone's phosphate groups (Fig. 7-2B). For every pair combination, our software places the dye at the designated attachment, aligning the linker's and backbone's phosphate coordinates. To prevent steric clashes between the dye and local DNA nucleotides, we align their corresponding centers of mass in an anti-parallel manner. This process is automated, in contrast to our prior methodology (Chapters 5-6) where this was done manually aided by molecular visualization software. This approach ensures the dimer-DNA configurations are optimal starting points for the subsequent MD simulations.

2) Molecular dynamics simulations.

Further optimizations are essential to feasibly simulate an extensive set of dimer-DNA configurations. For instance, statistics of DNA scaffolded constructs are primarily influenced by their local environment, so including residues distant from the dimer will contribute minimally to the results. Our strategy extracts a predetermined box surrounding the dimer for simulation, eliminating the need to simulate the entire DNA structure. Meanwhile, the effect of the omitted DNA structure is approximated using weak harmonic constraints on the terminal residues of the box. Placing these constraints is essential to maintaining the robustness of the long DNA strand as needed to ensure structural stability when attaching the dimer.

The generated samples from the previous step serve as starting structures for our MD simulations. These simulations are uniformly prepared using AmberTools23 [26], with molecules solvated in explicit TIP3P water. A consistent set of MD parameters is applied to all simulations. Due to the large number of samples, which complicates individual monitoring of each MD trajectory, simulations are executed for a fixed duration, long enough to ensure the equilibrium of the dimer within the compact DNA box.

3) Quantum mechanical analysis.

Upon completion, the equilibrated MD production trajectories are extracted for further analysis. Using geometric features, a clustering process identifies similarities among the samples. As outlined in Sec.6.4, we aim to find a correlation between chromophore orientation and intermolecular coupling. We categorize dimer samples based on geometric characteristics, such as the center of mass distance and rotational offset (Fig. 6-3).

Classification of the MD data is done with principal component analysis (PCA) [85, 123], followed by k-means clustering [92, 102] (Fig. 7-1). This results in the identification of structurally similar groups, which are then verified via quantum mechanical calculations to determine excitonic and charge-transfer coupling (Equations 5.2 and 1.6, respectively). PCA clustering parameters, such as the number of clusters or principal components, can be adjusted to ensure that most configurations within a cluster possess similar exciton properties.

By tracing the samples back to their associated scaffolding patterns, we can identify candidates matching specific coupling properties. These dimer-DNA structures can be experimentally validated to either support our theoretical predictions or provide insights for refining our methodology.

7.3 Computational Package

We now describe the implementation of the workflow in Fig. 7-1. The software is implemented as a Python3 package integrated with Amber and AmberTools23 [26]. Steps 0), 1), 2) and 3) in the previous section are implemented as four stand-alone modules that prepare all necessary input files for simulating the dimer-DNA samples and analyzing the resulting trajectories. The process, detailed as an information flow diagram in 7-3, starts with the preparation of the force field (*step 0*) by the `FF` module, which takes the optimized geometries of the dye and linker in PDB format. Then, the sampling (*step 1*) is done with the `MD` module, which takes the output from `FF` and a PDB of the DNA scaffold. For each sample generated, the `MD` module also prepares and initializes the MD simulations in Amber (*step 2*). For the final step, the `QM` module takes the trajectories generated in the previous step and carries out the analysis and electronic structure calculations (*step 3*). A fourth module `commons`, contains auxiliary functions for geometry operations and quantum mechanical calculations, which are employed by the main three modules. The remainder of this section will summarize the function of each module.

i) The `commons` module.

This module contains two submodules with functions shared by the other three modules. The submodule `geom_utils` contains functions that carry out a variety of operations in molecules, as well as facilitates the import of PDB files. Molecules and trajectories are imported using the MDAnalysis package [67, 110]. On the other hand, `coupling_utils` handles all excited-state electronic structure calculations, which includes calculating the excitonic and CT coupling. These calculations are performed with the aid of the PySCF package [141].

ii) The `FF` module.

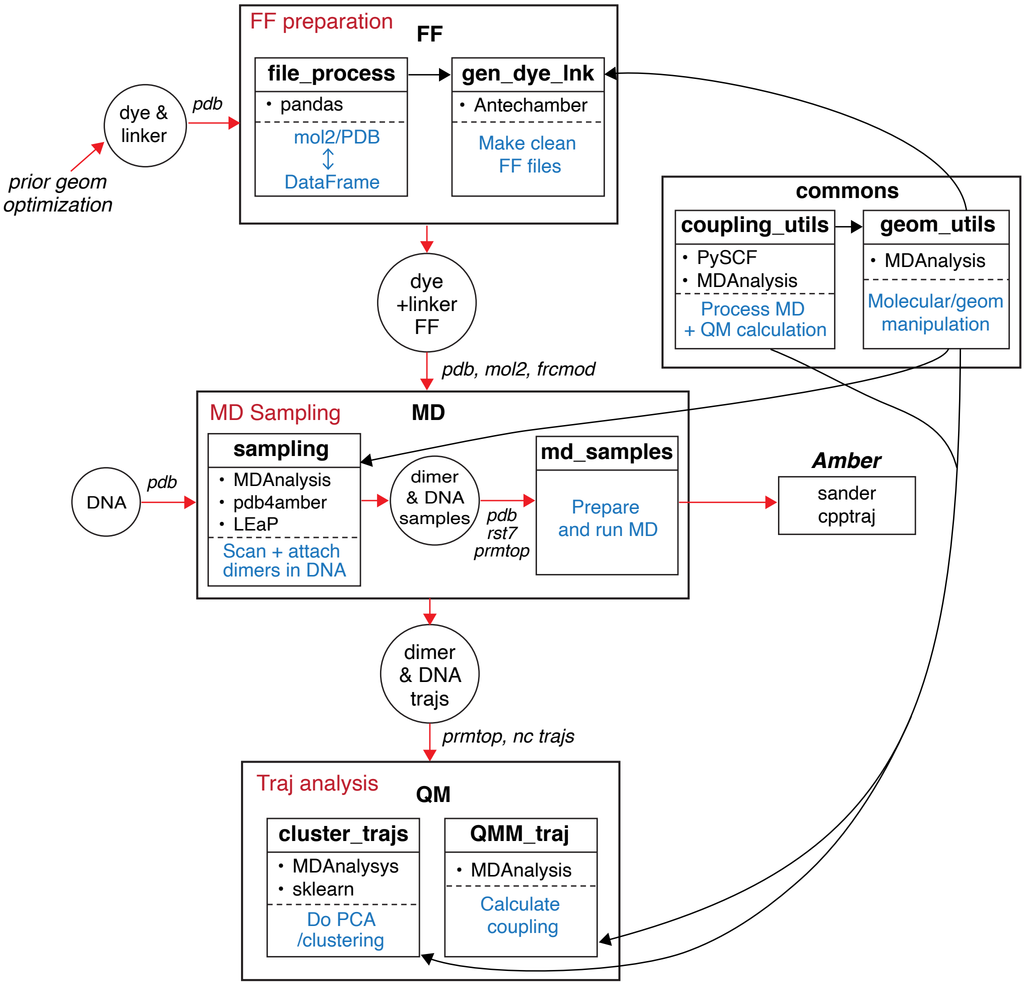

Figure 7-3: Flow of information in our screening software package. Python Modules are represented with large squares, while sub-modules are smaller rectangles within a module. Circles represent data (input/output) with the file type indicated outside of the circle in italics. Red arrows indicate the direction of the workflow, while black arrows indicate package dependency. The workflow starts from the top, with the molecular (PDB) files for the geometry-optimized linker and dye.

The first step in Fig 7-1 is building the force field for the dye and the linker, separately. This step is carried out by the `FF` module, taking the optimized geometries of the two fragments—capped with appropriate chemical groups— in PDB format. The outcome of this step is to generate output files for the dye-linker FF that can be interpreted by Amber.

To begin, we pre-process the dye and linker PDB input geometries for subsequent steps. Specifically, each atom is assigned a unique name, as required for building a FF.

Then, the main step for the FF preparation is calculating the atomic charges. For efficiency, this is done with the am1-bcc semi-empirical method [82], as implemented in Amber's Antechamber [148]. The output, a *mol2* FF file, also contains information about atom types, according to the generalized Amber FF (GAFF) [149]. For this fragment-based approach, the cap groups are necessary to ensure charge neutrality, with the caps matching the charge of the counterpart fragment. However, these caps need to be eliminated from the final FF of the dye+linker molecule. This module will also modify the *mol2* files, eliminating the surplus atoms while making sure the charge is maintained. Finally, the module will output the modified *mol2* files for the linker an atom, a joined PDB file for the dye+linker molecule, and a parameter modification file, *frcmod*. The latter contains modified force field parameters which are generated automatically by AmberTools [26]. Note at this step that for molecules with non-standard atoms and bonds, the *frcmod* file needs to be manually modified by the user.

Within this module, the submodule `file_process` contains auxiliary functions for reading, modifying and writing PDB and *mol2* by storing the data in pandas DataFrames [106]. On the other hand, the `gen_dye_lnk` submodule contains functions that support the process described above. The joined PDB file is generated by the `commons/geom_utils` auxiliary module. The fragments are aligned such as the centers of mass are anti-parallel to decrease steric constrains.

iii) The `MD` module.

This module takes the output from the previous step, namely, the force-field *mol2* and *frcmod* files, and the joined PDB for the dye and linker molecule, along with a PDB for the DNA-scaffold. With these four as an input, the module samples dimers from the dye+linker modified molecule along the given DNA scaffold structure, and initializes MD simulations for each one of the generated samples.

The sampling of dimers in DNA is carried out by the `sampling` submodule. This submodule will 1) Read and process the monomer and dye PDB files, 2) sample all possible pairs that can be attached in the DNA based on a pre-defined intermolecular distance, and 3) for each valid pair place the dimer in position and generate a PDB and AMBER LEaP input file of the dimer within a DNA box. Potential attachment points, i, are defined using the P atom coordinates across the DNA, and dimers are defined by (i, j) pairs, where $i-1$, i and j, $j+1$ define the attachment points of each doubly-linked dye. Then, a KDTree algorithm, as implemented in SciPy [12, 145], is employed to determine all possible nearest neighbor pairs (i, j) within the maximum distance defined for a valid pair. Adjacent dimers (*i.e.,* 0nt) are defined by (i, i) pairs.

For each valid pair, we then define a DNA box that will allow us to approximately describe the steric interactions we need to take into account in the alignment process of the dimer in the duplex. A separate box is defined around each monomer, centered around the midpoint between the attachment points, and with a pre-defined box length. Each monomer is aligned such that the P atom in each linker overlaps with the P atom in the DNA binding site, and the center of mass of the dye is antiparallel to that of the DNA box.

Linkers attach to the DNA through the phosphate -PO_3 group, which is included in the linker FF to ensure consistency of charge distribution between a dye-linker in solution and attached to DNA. Because each P atom can only bond to 4 oxygen atoms at a time, after bonding to the dye, the bond with the adjacent nucleotide is broken. A molecule with two symmetric attachments, such as Cy3, will bond with two adjacent PO3 DNA groups, breaking two bonds: P-O5' and O3'-P (As labeled in Fig. 7-2). As a result, the nucleotide supported by these bonds is solvated. To avoid having an incomplete DNA residue, which will lead to problems with AMBER, we assign the phosphate on the O3' side to be in the dye residue, while having the phosphate on the O5' side belong to the adjacent residue (as labeled in Fig 7-2). Following this process will result in a standard PDB file that should be recognized by the standard GAFF and the OL15 DNA FF.

In the last step, we save the dimer sample by defining a second DNA box around the dyes. The program will make sure there are no incomplete residues left in the box and transform the edge residues into terminal nucleotides for FF consistency. The dimer is then merged with the DNA into a single PDB file. The *mol2* and *frcmod* FF files from the previous module are also modified, as during the sample generation some atoms were changed.

Finally, to generate the input files that Amber requires to initialize the MD simulations, the `sampling` module integrates with LEaP [26] to produce these files from the PDBs. LEaP will take the FF files for the dye and linker, and the sample PDB to generate parameter *prmtop* and coordinate *rst7* files for the system solvated in explicit TIP3P water, with Na^+ ions added for charge neutrality. Prior to executing, we also clean the PDB file with pdb4amber (as implemented in AmberTools23), define the atoms that will take part in the dimer-DNA bonds, and generate input files for the LEaP program.

The `md_samples` takes the output from `sampling` to initialize the MD simulations. A similar procedure to that described in [72] is followed, with the all-atom MD simulations performed in Amber, using The OL15 FF for the DNA residues and GAFF for the dimer residues. First, the solvent and ions are minimized for a total of 4000 steps, and then the entire system is minimized for another 4000 steps. This is followed by a slow equilibration of the system from 0 to 300 K, with weak 10 kcal mol^{-1} $Å^{-2}$ restraints imposed on the DNA, for a total of 20 ps. A second minimization of the system in an NPT 300 K ensemble is followed for an additional 100 ps, with weaker restraints imposed (5 kcal mol^{-1} $Å^{-2}$). Finally, production runs in an NPT ensemble are carried out until equilibrium. To mimic the effect of the long DNA structure, in the reduced-sized box we include in each sample, we apply weak 3 kcal mol^{-1} $Å^{-2}$ constraints on the terminal nucleotides of each sample throughout the simulations. Doing so avoids the destabilization of the short DNA-box strand. All simulations were carried out employing the parameters of Chapter 5 and Ref. [72], with a 10 Å cutoff to calculate the Van der Waals energies. The input files for each sample and MD step where prepared with the `md_samples` submodule, which also executed the runs within Amber's sander program [26].

iv) The `QM` module.

After completion, the MD trajectories for all of the samples are imported into the Python environment using MDAnalysis [110], which takes the parameter *prmtop* and trajectory *nc* files as inputs. Because we are interested in the statistics of the chromophore-chromophore interaction, we extract the coordinates of the dimer from these trajectories for further analysis. To extract the chromophore geometries, we break the O-PO_3 bond on each linker. Then, the remaining O3' and O5' atoms in the linker are capped with H's to ensure the molecule's stability for the subsequent quantum mechanical calculations. We choose not to keep the phosphate groups for further analysis because they complicate simulation convergence.

Based on the extracted trajectories, we calculate a set of geometrical features that could potentially encode the complex interactions between the chromophore molecules. These features are calculated for the last 200 ps by the auxiliary module `geom_utils` and stored in a pandas DataFrame [106]. We then perform PCA in the generated features, reducing the number of components to those needed to preserve at least 80% of the variance. Then, starting from these principal components, we employ the k-means clustering algorithm to find similarities in the data. The number of clusters is optimally defined using the inflection point or "elbow" after which the score converges with respect to the number of clusters [128]. The representative structure for each cluster is then calculated as the structure closer to the cluster center. Both data extraction and clustering are performed by the `cluster_traj` submodule.

For each representative structure, quantum mechanical calculations are performed to calculate the excitonic and charge transfer coupling according to Equations 5.2 and 1.6, respectively. These operations are performed by the `QMM_traj` submodule, using auxiliary functions from the `coupling_utils` module. We follow the same process outlined in 6.3. The `coupling_utils` module calculates V_{exc} via TDDFT/TDA as implemented in PySCF [141], while the electron/hole integrals in V_{CT} are calculated with the Löwdin symmetry transform (Eq. 6.3), as implemented in the Q-chem software [133]. For the transfer integrals, the `QMM_traj` submodule prepares the input files required by Q-chem.

7.4 Results

We apply our workflow to screen Cy3 dimer configurations within DNA duplexes. The FF was prepared for the dye and linker pair in Fig. 7-2. These two fragments were capped with groups sharing a chemical similarity to their complementary fragment near the bond. A PDB file was prepared for a Cy3-modified dye with two copies of the linker, which allows the dye to be scaffolded in the DNA at two adjacent attachment points. A DNA duplex with 21 complementary base pairs was chosen as the scaffolding. Dimer positions were sampled within a limit 18.5 Å distance between attachment points, which was determined to render dimer configurations with non-negligible interaction. Because sampling occurs before MD equilibration, It is advisable to choose a distance that covers configurations initially positioned at large binding distances but that could later equilibrate into dimers with significant interaction. The resulting dimer samples were simulated along with all the DNA residues fitting inside a pair of 20 Å-length boxes centered around the two attachment points. From a total of 311 valid samples within the pre-defined distance, we selected 80 for further analysis and simulation.

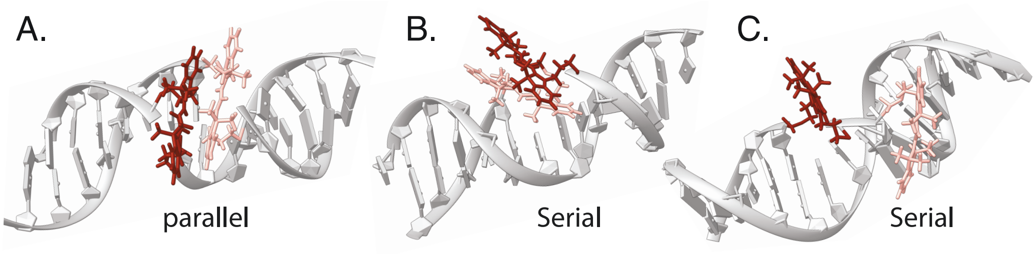

Figure 7-4: Examples of a Cy3 dimer sampled in DNA duplex. Equilibrated molecular structures for a (A) Parallel 3nt (B) Serial 0nt and (C) Serial 1nt samples.

Molecular dynamics simulations are prepared and initialized on Amber20 [25]. Figure 7-4 shows a few of the samples generated for Cy3 in DNA Duplex, after all the MD steps are performed and the trajectories are equilibrated. The structures for a parallel 3nt, serial 0nt and serial 1nt dimer are shown (Fig. 7-4A-C respectively). From the simulated trajectories, we prepared the following set of four features: Center of mass intermolecular distance, rotational offset along the long axis, and displacement along the short and long axis. The selection was made based on the features that have been previously observed to have a strong effect on short-range chromophore interactions (Chapter 6 and Ref. [78]).

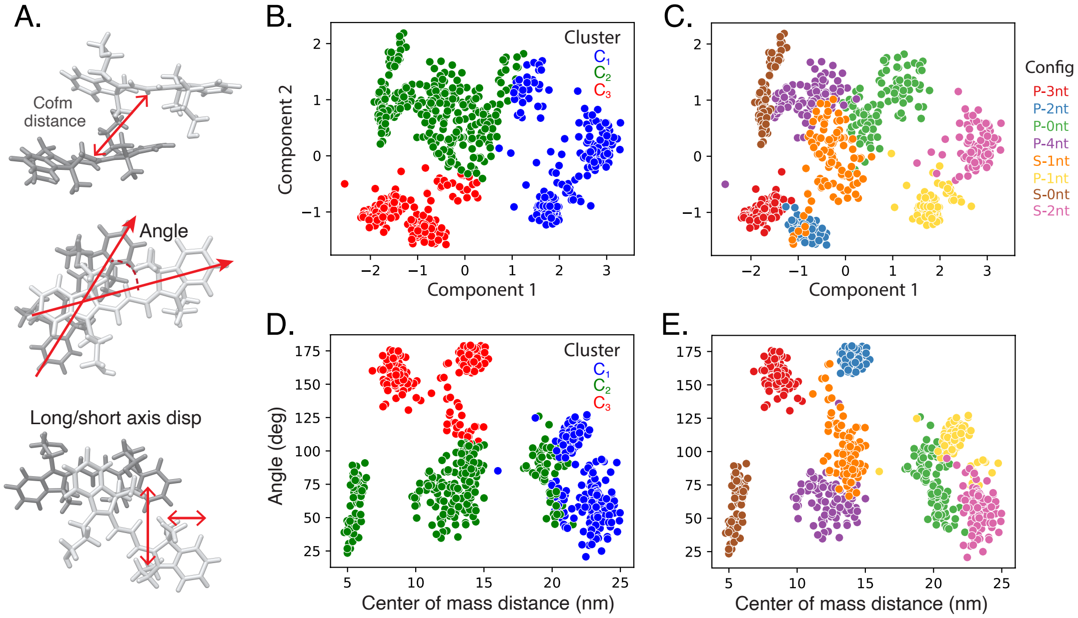

Figure 7-5: PCA and clustering of Cy3 dimer geometry. (A) Dimer geometry is characterized using the center of mass distance, the angle between the molecules' long-axis vectors, and the long and short-axis displacements. PCA is employed for dimensionality reduction of the geometrical data, followed by K-means clustering to separate the data by spatial similarity. Scatter plots presenting the data in the two principal components, colored by (B) cluster and (C) DNA attachment type. Scatter plots for the features contributing the most to the two principal components: the rotation angle and center of mass distance, colored by (D) cluster and (E) attachment type.

The last 200 ps of simulation for each one of the samples is selected for subsequent cluster analysis. Figure 7-5B presents the result of PCA followed by k-means clustering on a total of 8 samples—each with a different scaffolding pattern—using the four geometrical features described above. The number of principal components and number of clusters were set to their optimal values, as described in the previous section. We see that from the eight configurations, the data is classified into three clusters each sharing similar spatial properties. The clusters are also traced back to the different attachment configurations and colored correspondingly in the PCA-clustering data (Fig. 7-5C). We see that most configurations belong entirely to a single cluster, with the exception of samples that are probably not fully equilibrated. This is the case, for example, of the serial- 1nt and 2nt (S-1nt and S-2nt) and the parallel-1nt (P-1nt) configurations. These configurations likely favor reorganization within the DNA base-pair interactions to decrease inter-chromophore distance, as previously observed with squaraine dimers [72], resulting in slower equilibration of the dimer-DNA system. Another interesting observation is the similarity of the S-0nt and P-4nt dimers, which comprise the C_2 cluster, along with S-1nt. At 4nt separation, after a full turn of the DNA double-strand, two parallel dyes will be placed along the same line, resulting in a similar configuration to a S-0nt dimer. After equilibration, both of these dimers seem to have driven similar conformational changes in the DNA scaffolding, therefore sharing similar spatial features. The other clusters, C_1 and C_3, seem to be composed of similar scaffolded structures. The C_1, by dimers with little apparent interaction (S-2nt, P-1nt and part of P-0nt), and C_2 by two parallel dimers with similar nt separation.

Next, we analyze the features that contribute the most to the principal components in Fig. 7-5D and E. As expected from the results of the previous chapter, these are the center of mass distance and the rotational offset. Figure 7-5 shows a scatter plot of the data with respect to these two features. The result is expected, as the intermolecular distance and rotation angle were previously observed to have the strongest effect in the coupling between PDI dyes (Sec. 6.4. We see very similar patterns of classification for the different attachments, especially for cluster C_1. Some separation is observed between the two parallel dimers P-3nt and 2-nt in cluster C_3. For these dimers, significant similarity is observed in the short and long-axis displacement, even though the dimer separation is different. This observation highlights the necessity of utilizing multiple features along with dimensionality reduction. This is because the spatial interactions of dimers cannot always be explained solely in terms of intermolecular distance and rotational offset, as was previously attempted in Sec. 6.4.

For each one of the clusters, we now need to confirm that the data was not only classified in terms of spatial correlation but that these configurations also share a connection in terms of photophysics. To this end, a representative structure for each one of these clusters is selected as the dimer closest to the center of the cluster. These representative configurations are, in order, parallel-1nt, parallel-4nt and serial-1nt. The calculated excitonic and CT coupling are to be compared between these structures to note differences in the calculated values characterizing each spatial group. Similarly, these values must be compared with those calculated for other dimer samples within the same cluster, in order to determine whether the classification procedure was adequate. Disagreement between these values would indicate the need to tweak the PCA-clustering procedure. In the case of Fig. 7-5, this will most likely point to the number of clusters chosen, as significant variations can be observed among samples of the same cluster.

7.5 Future Directions

In this chapter, we have outlined a systematic workflow for the evaluation and characterization of dimer configurations within DNA scaffolds. In particular, we applied our methodology to sample Cy3 dimers in a DNA Duplex. A total of 8 unique configurations were simulated and classified by their geometric characteristics.

Nevertheless, the results depicted in Fig. 7-5 represent merely a subset of the extensive collection of Cy3 dimer samples generated throughout this study. While these initial findings elucidate some correlation between various types of attachments, they fall short of delivering a comprehensive understanding of how DNA scaffolding influences dimer configurations. Specifically, we have presented only a single instance of each attachment type, with the possibility that some may not have achieved the global minima conformation by the end of the molecular dynamics simulations. Addressing this, further exploration involving multiple iterations of identical attachment types, originating from random initial conditions, may enhance the diversity of sampled trajectories without a proportional increase in simulation time. Currently, simulations are ongoing for the remaining 72 dimer samples, with the anticipation of refining our understanding of their dynamic behavior.

At the moment of writing this chapter, a complete quantum mechanical analysis of the samples is also in progress. This analysis is poised to shed light on the impact that DNA scaffolding has on the photophysical properties of chromophore dimers, especially concerning their exciton and charge-transfer (CT) interactions. Significantly, this investigation is expected to pinpoint configurations with optimal properties for further experimental validation.

Looking ahead, we aim to expand the application of our methodology to a broader range of dye and DNA scaffold combinations. Our workflow's inherent adaptability positions it well for generalization to diverse systems, opening avenues for the investigation of novel materials with programmable excitonic behaviors. Additionally, the versatility of our force field design permits the exploration of alternative dye and linker arrangements In conjunction with AI-driven searches within the chemical space, it could potentially be employed for the identification of prime photoactive molecules tailored to specific applications.

Overall, the combination of high-throughput computational approaches and refined experimental techniques is poised to be instrumental in the future advancement of materials science, paving the way for breakthroughs in fields such as light-harvesting, electronics, and quantum computing.

Appendix A

Bounds on the Complexity of a Realizable Unitary Operation

Although Eq. 2.1 provides the geometric constraints for representing a given unitary operation as an excitonic circuit, it is not guaranteed that these can be physically satisfied. For example, it is possible that the number of constraints exceeds the number of degrees of freedom within the geometric design space. In this subsection we enumerate the degrees of freedom available to systems of multiple molecules and thus establish fundamental bounds on the complexity of operation that can be represented by a circuit with a given number of dye molecules.

In order to implement an $N-$dimensional unitary transformation in the single excitation manifold a set of N dyes is required. The diagonal matrix elements of $\hat{U}_{\text{target}}$ impose $N-1$ constrains on the Hamiltonian, after accounting for invariance under the total phase change. These can be satisfied using the $N-1$ relative energy degrees of freedom, ϵ_i. This leaves $N(N-1)$ off-diagonal matrix elements that must be satisfied. However, the logarithm of unitary transformations must be anti-Hermitian, indicating that the lower triangle of the matrix can be inferred from the upper triangle, leaving $\frac{1}{2}N(N-1)$ independent constrains. The freedom of choosing τ introduces a free choice of scaling, which removes one additional constraint.

These constraints must be satisfied by tuning the geometric degrees of freedom of the dye assembly. Each of the N dyes introduces three degrees of freedom corresponding to the dye positions, resulting in $3N$ degrees of freedom. Each of the N excitations also gives three degrees of freedom corresponding to the orientation of their transition dipole moment, which gives an additional $3N$. However, invariance under center of mass translation and total rotation removes a total of 5 of these degrees of freedom. Overall, such a dye assembly provides sufficient flexibility to realize an $N-$dimensional transformation if,

$$6N - 4 \geq \frac{1}{2}N(N-1). \tag{A.1}$$

Clearly A.1 is satisfied for all $N \lesssim 12$ leaving at least three excess degrees of freedom. These excess degrees of freedom indicate the effective dimensionality of the *manifold* of possible dye configurations that implement a given transformation. As we will discuss later, this extra flexibility can be used to optimize the performance of the system in the presence of environmental noise and to construct systems that enable straightforward experimental initialization and measurement.

This analysis bounds the complexity of transformations that can, in principle, be realized in excitonic systems. However, it assumes a freedom in selecting the positioning, energies and transition dipole moments of the dyes that does not exist in practical applications. Realistically, any given scaffolding approach may have restrictions on dye placement and may only be compatible with a restricted subset of dyes. These practical constraints make the added flexibility of the excess degrees of freedom essential as they can be used to design around the limitations of a given experimental approach. In the remainder of this paper we will show that, at least for simple transformations, the required constraints leave a great deal of flexibility in implementation.

Appendix B

Additional Details on the Simulation of Excitonic Circuits in Model and Atomistic Environments

B.1 Population Dynamics of Excitonic Circuits in Model Environments

The population dynamics of all four dyes comprising the idealized circuits in Section 3.4, for each step in the serial approach, are shown in Figure B-1. Note that the first step is identical for both versions of the algorithm (*i.e.,* $\hat{\mathcal{H}}_1$), and therefore here the resulting populations are only shown once. On the other hand, the third step population dynamics are shown for both circuits, to illustrate the effect of the difference in initial states, even though both circuits evolve with $\hat{\mathcal{H}}_3$. The second step for the constant version is not shown, as the identity oracle operation has no effect on the exciton populations.

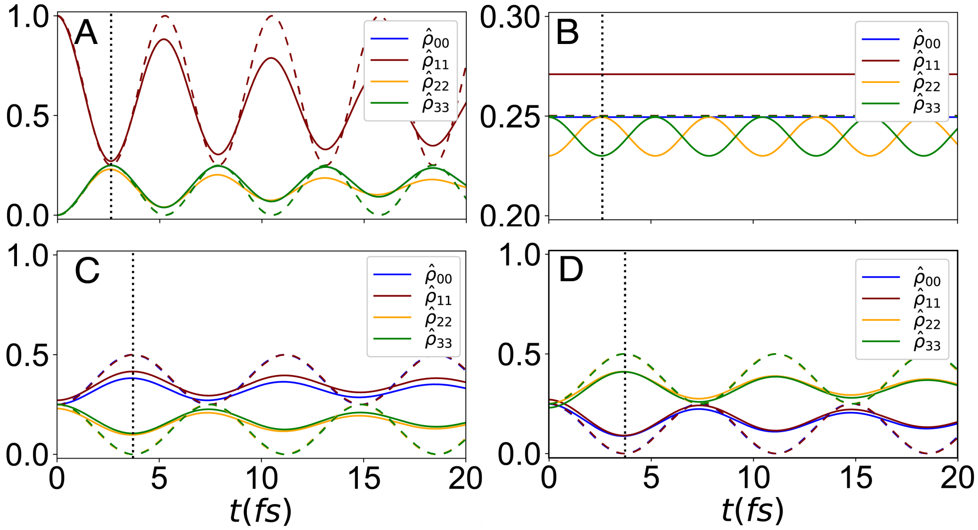

Figure B-1: Time-evolution of the populations of the D-J algorithm with a model environment (extension of Fig. 3-2). Populations of all four dyes in each excitonic circuit are shown for the (A) first, (B) second and (C) third steps of the balanced version of the D-J algorithm. The third step corresponding to the constant version of the D-J algorithm is depicted in (D).

B.2 Methodology for the QM/MM Simulation of Cyanine Excitonic Circuits.

All-atom Molecular Dynamics Simulations for Cy3 and Cy5 Constructs. The molecular simulations in this paper followed a similar methodology as that described by Ref. [72] Prior to performing the all-atom molecular simulations over the Cy3-Cy5 constructs, a force field was generated for both the Cy3 and Cy5 monomers. The structures for Cy3-oxypropyl and Cy5-oxypropyl were built using the Avogadro software (version 1.2.0), [7] and the geometry was optimized with the restricted Hartree-Fock (RHF) method and the 6-31G(d) basis set, as included in the Q-chem software [133]. The atomic point charges were generated with a Restrained Electrostatic Potential (RESP) fit also using Q-Chem, and the generalized Amber force field (GAFF) [149] was employed for all force field terms.

The optimized spatial parameters obtained from the genetic algorithm code were used to build the Cy3-Cy5 constructs with the MDAnalysis software [110, 108], using the equilibrium geometries. All-atom Molecular Dynamics (MD) simulations were performed on these cyanine systems using the software Amber18 [24] with the GAFF2 force field [149]. The structures were solvated in TIP3P water molecules, and a distance of 10Å with respect to the solvent box. Explicit Cl^- ions were added to neutralize the cyanine molecules. Periodic boundary conditions were applied to all MD simulations, and the SHAKE algorithm was applied to constrain the H atoms to their equilibrium bond length. A 12Å cutoff was used to calculate the Van der Waals energies, while The Particle Mesh Ewald (PME) method was employed to calculate full electrostatics. The simulations were carried out in an NPT ensemble using the Langevin thermostat for temperature control with a collision frequency of 2 ps^-1, and the Berendsen barostat for pressure control, with a reference pressure of 1 bar. Prior to the production simulation, a minimization was carried out over the constrained system during 5000 steps. Then, the constrained system was allowed to equilibrate while it was slowly heated to 300 K, for a total time of 10 ps and time-step 1 fs, which was followed by a second equilibration for 5 ps at constant temperature. The production dynamics were then generated at 300 K during a total of 6 ps. A smaller time-step of 0.1 fs was used during this step to carefully simulate the short-time dynamics of interest.

Excited State Quantum Mechanical Calculations.

The geometries for the CY3-CY5 constructs, corresponding to $\hat{\mathcal{H}}_1$ and $\hat{\mathcal{H}}_3$, were sampled from the MD trajectories every 4 fs. For each time frame, the coordinate data for the cyanine molecules was extracted using the MDAnalysis package [110], and the singlet excited state energies were calculated for each individual molecule using PySCF with the TDDFT 6-31G/B3LYP level of theory [141].

B.3 Determination of Bath Fluctuations Effects on the Cy3-Cy5 Circuits

Fitting the Energy-gap Correlation Function into a Functional Form.

The parameters employed to fit the correlation function, $C(t)$, into the functional

Table B.1: Fitting parameters for the Cy3(A) dye in the excitonic circuit realizing $\hat{\mathcal{H}}_1$.

Exponential	$a_i[10^{-5}eV]$	$\tau_{c,i}[fs]$	
1	2.000	18.22	
2	0.089	16.88	
Damped	$\tilde{a}_i[10^{-5}eV]$	$\tilde{\tau}_{c,i}[fs]$	$2\pi/\tilde{\omega}_i[fs]$
1	1.000	157.9	21.49
2	4.525	152.7	58.45
3	0.501	1079	20.35
4	5.983	87.60	17.74
5	3.354	41.01	15.84
6	3.875	15.79	12.41

Table B.2: Fitting parameters for the Cy5(B) dye in the excitonic circuit realizing $\hat{\mathcal{H}}_1$.

Exponential	$a_i[10^{-5}eV]$	$\tau_{c,i}[fs]$	
1	3.128	19.18	
2	38.71	98.27	
Damped	$\tilde{a}_i[10^{-5}eV]$	$\tilde{\tau}_{c,i}[fs]$	$2\pi/\tilde{\omega}_i[fs]$
1	1.276	117.7	21.60
2	7.805	117.2	82.54
3	1.340	3500	19.98
4	7.253	57.26	16.83
5	10.577	13.27	13.64
6	2.306	1489	17.67

form in Eq. 3.14 are presented in tables B.1 to B.4, for the $\hat{\mathcal{H}}_1$ excitonic circuit. The resulting fit is compared with the numerically calculated correlation in Figure B-2. Note the fit is not exact due to the small number of parameters employed, however, the fit is appropriate to understand the behavior of the different correlation curves.

Analysis of the Fluctuations of the Torsional Angles in Cyanine Circuits.

Variations in the dephasing time between the different cyanine molecules in the circuits can be explained in terms of the confirmations these molecules acquire as a function of time. We analyze the torsional angles θ and ϕ for the Cy3 and Cy5 molecules (Fig. B-3A) to reveal the origin of the strike differences observed in the effect of bath fluctuations. The change of these torsional angles as a function of time reveals a conformational shift on the Cy5(B) dye involving one of the heterodimer rings. On the other hand, the other three molecules do not exhibit significant variation in their

Table B.3: Fitting parameters for the Cy3(C) dye in the excitonic circuit realizing $\hat{\mathcal{H}}_1$.

Exponential	$a_i[10^{-5}eV]$	$\tau_{c,i}[fs]$	
1	6.520	0.290	
2	19.10	37.18	
Damped	$\tilde{a}_i[10^{-5}eV]$	$\tilde{\tau}_{c,i}[fs]$	$2\pi/\tilde{\omega}_i[fs]$
1	1.000	1000	20.48
2	0.000	525.2	60.97
3	0.995	2600	22.07
4	8.849	20.00	15.06
5	9.192	71.99	17.81
6	1.065	17800	17.95

Table B.4: Fitting parameters for the Cy5(D) dye in the excitonic circuit realizing $\hat{\mathcal{H}}_1$.

Exponential	$a_i[10^{-5}eV]$	$\tau_{c,i}[fs]$	
1	70.00	10.00	
2	70.00	43.33	
Damped	$\tilde{a}_i[10^{-5}eV]$	$\tilde{\tau}_{c,i}[fs]$	$2\pi/\tilde{\omega}_i[fs]$
1	28.24	2000	514.7
2	28.59	2000	171.9
3	3.451	2480	67.99
4	5.755	2392	17.57
5	2.059	2450	27.17
6	4.053	2000	26.31

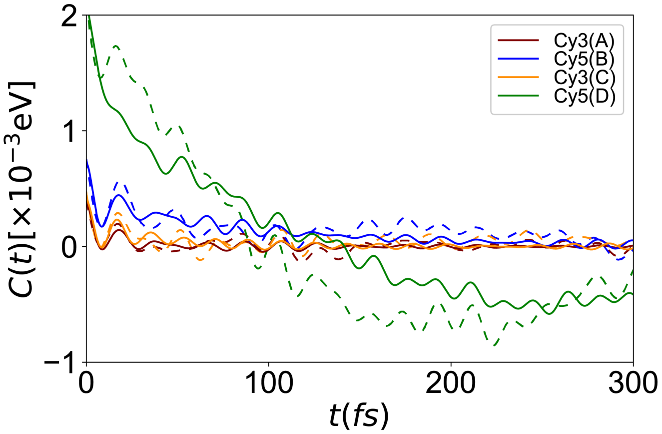

Figure B-2: Correlation function for $\hat{\mathcal{H}}_1$ fitted to a double exponential with damped oscillations functional form, as described in the main text. The dashed lines show the time evolution of $C(t)$ as calculated numerically from the data set for ε_{01}.

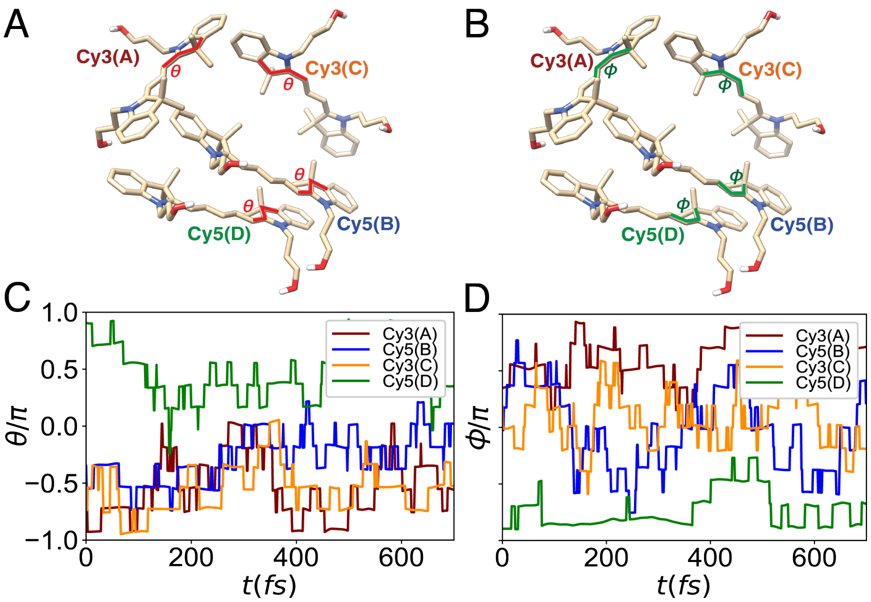

Figure B-3: Fluctuations on the relative geometries of the Cyanine molecules for the $\hat{\mathcal{H}}_1$ circuit. The time evolution of two torsional angles is evaluated, θ and ϕ. The angles are indicated in (A) and (B), respectively, while the evolution of these for a space of 700 fs is shown in (C) and (D).

structure that could indicate a conformational change. Structural reorganization resulting from the thermal bath in Cy5(B) may be responsible for the unexpectedly short dephasing time.

Spectral Density via Numerical Integration of the Correlation Function. The spectral density was first calculated through a numerical integration of the correlation function via Eq. 3.13. The resulting noisy spectra are shown in Figure B-4 for both circuits studied in this manuscript. The intricate nature of the spectra most likely is due to the lack of sampling data, with $C(t)$ not decaying completely to zero over the time range where $J(\omega)$ was evaluated. However, we can note that, generally, the same molecules share similar peaks, although with varying amplitudes that directly depend on the magnitude of the bath fluctuations for each dye. In particular Cy5(B) in circuit $\hat{\mathcal{H}}_1$ shows a large amplitude frequency mode around 600cm^{-}1. This peak probably corresponds to the vibrational mode on the heterocycle ring and confirms our hypothesis of a conformational change modifying the spectroscopic properties of this dye. As described in the main text, the standard description of the spectral density in Eq. 3.13 often fails to characterize high-frequency vibrational modes, and this region of the spectra is more accurately described with a harmonic approximation of $J(\omega)$.

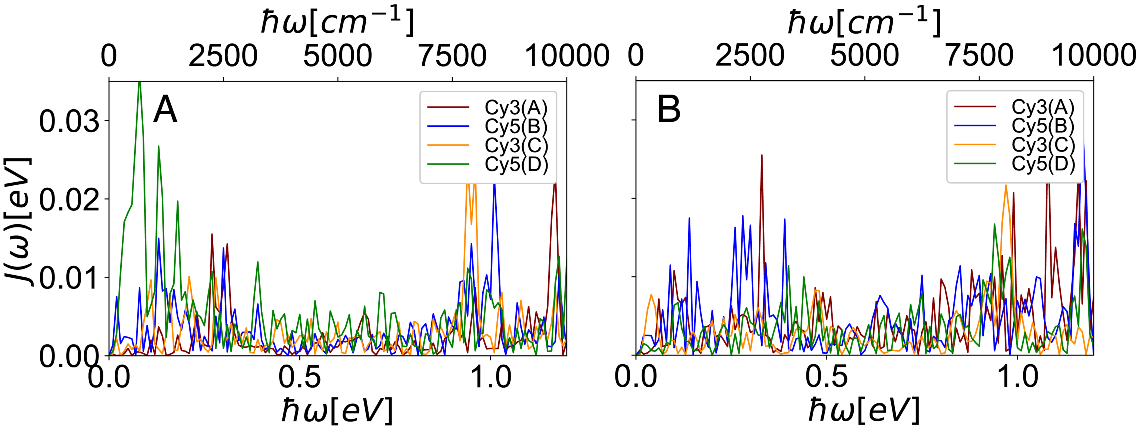

Figure B-4: Spectral density, $J(\omega)$ evaluated from the numerical integration of $C(t)$ as in Eq. 3.13, for the circuits evolving as $\hat{\mathcal{H}}_1$ and $\hat{\mathcal{H}}_3$, respectively.

Fitting the Numerical Spectral Density.

Assuming the correlation function, $C(t)$, takes a double exponentially decaying functional form we have,

$$C(t) = a_1 e^{-t/\tau_{c,1}} + a_2 e^{-t/\tau_{c,2}}, \tag{B.1}$$

which is derived by setting $\tilde{a}_i = 0$ in Eq 3.14. The corresponding spectral density is derived in the main text (Eq. 3.15), and the numerical spectra in Figure B-4 are fitted to this functional form. The fitting parameters are listed in Table B.5, while the fitted $J(\omega)$ is shown in the main text for both cases.

Table B.5: Fitting parameters for the spectral density.

$\hat{\mathcal{H}}_1$ Dye	$a_1[10^{-5}eV]$	$a_2[10^{-5}eV]$	$\tau_{c,1}[fs]$	$\tau_{c,2}[fs]$
Cy3(A)	65.96	65.83	2.513	2.512
Cy5(B)	9581	99.31	2.214	2.215
Cy3(C)	8626	95.71	2.200	2.200
Cy5(D)	140.9	3587	10.00	0.035
$\hat{\mathcal{H}}_3$ Dye	$a_1[10^{-5}eV]$	$a_2[10^{-5}eV]$	$\tau_{c,1}[fs]$	$\tau_{c,2}[fs]$
Cy3(A)	159.2	159.2	1.997	1.997
Cy5(B)	185.4	182.8	1.930	1.930
Cy3(C)	125.5	125.5	1.721	1.722
Cy5(D)	154.7	150.3	1.779	1.779

Appendix C

Mathematical Derivations on the Dynamics of Dimer Systems with Complex-valued Coupling

C.1 Derivation of the Wavefunction Coefficients for the ***Circular*** and ***Linear*** Dimer System

In the Frenkel exciton model, The wavefunction for the dimer with a *linear* and $D_{N\mathrm{h}}$ *circular* dyes, excited through circularly polarized light, can be represented with four electronic states, [11]

$$\begin{aligned}|\Psi(t)\rangle =&C_g(t)|g\rangle e^{-iE_gt/\hbar}\\ &+C_e(t)|e\rangle e^{-iE_et/\hbar}\\ &+C_+(t)|+\rangle e^{-iE_+t/\hbar}\\ &+C_-(t)|-\rangle e^{-iE_-t/\hbar},\end{aligned} \tag{C.1}$$

where $C_i(t)$ and E_i are the wavevector coefficients and transition energies for the exciton state $|i\rangle$, with $i = g, e, +$ and $-$, representing the ground state $|g\rangle \equiv |gg\rangle$, an exciton located on the *linear* molecule, $|e\rangle \equiv |eg\rangle$, and the exciton located in the $\pi_\pm$

MO of the *circular* molecule, $|+\rangle \equiv |g+\rangle$ and $|-\rangle \equiv |g-\rangle$, respectively,

When the wavefunction above is perturbed by a circularly-polarized laser field $\varepsilon_{\pm}(t)$, its time evolution can be described under the dipole approximation using the time-dependent Schrödinger equation (Eq. 4.7. The right/left circularly polarized pulse (RCP/LCP) is described in terms of its cartesian components by Eq. 4.8

with field amplitude ε_0, carrier frequency ω, phase η, shape function $s(t)$ and unit vectors e_x and e_y along the x- and y-axes. The time-dependant dynamics of the coefficients $C_i(t)$ can be derived by combining 4.7 with the time-independent Schrödinger expression, $H_{el}|\Psi_i\rangle = E_i|\Psi_i\rangle$,

$$i\hbar\dot{C}_j(t) = -\varepsilon_{\pm}(t)\sum_i C_i(t)\langle\psi_j|\hat{\mu}|\psi_i\rangle e^{-i\omega_{ij}t}. \tag{C.2}$$

Expanding for $i = g, e, +$ and $-$,

$$i\hbar\dot{\mathbf{C}}(t) = -\varepsilon_{\pm}(t)\begin{pmatrix} 0 & \langle g|\mu|e\rangle e^{-i\omega_L t} & \langle g|\mu|+\rangle e^{-i\omega_C t} & \langle g|\mu|-\rangle e^{-i\omega_C t} \\ \langle e|\mu|g\rangle e^{i\omega_L t} & 0 & 0 & 0 \\ \langle +|\mu|g\rangle e^{i\omega_C t} & 0 & 0 & 0 \\ \langle -|\mu|g\rangle e^{i\omega_C t} & 0 & 0 & 0 \end{pmatrix}\mathbf{C}(t), \tag{C.3}$$

where $\omega_L = (E_e - E_g)/\hbar$ and $\omega_C = (E_{\pm} - E_g)/\hbar$ are the excitation energies for the *linear* and *circular* molecules, and we have taken the ground state to be the reference energy, $E_g = 0$. Note the dipole is non-zero only for the ground to excited state transitions. The effect of the laser field, with frequency ω_C, on the *linear* excitation can be calculated by expanding the dipole vector in terms of its Cartesian components, $\langle g|\mu|e\rangle = |\mu_L|\cos\theta\hat{x} + |\mu_L|\sin\theta\hat{y}$,

$$\begin{aligned} -\langle g|\mu|e\rangle e^{-i\omega_L t}.\varepsilon_{\pm}(t) &= -\varepsilon_0 s(t)|\mu_L|e^{-i\omega_L t}\cos(\theta)\cos(\omega_C t) \pm \sin(\theta)\sin(\omega_C t) \\ &= -\varepsilon_0 s(t)|\mu_L|e^{-i\omega_L t}\cos(\theta \mp \omega_C t) \end{aligned} \tag{C.4}$$

where we have used the trigonometrical identities for $\sin\alpha\sin\beta$ and $\cos\alpha\cos\beta$. For the *circular* exciton, the pulse with resonant frequency ω_C will interact with the x

and y components of the complex excitations, as previously described in 4.1). For example, for an RCP field, we obtain the following expressions,

$$-\langle g|\mu|+\rangle e^{-i\omega_C t}.\varepsilon_{\pm}(t) = -\varepsilon_0 s(t)\mu_C \tag{C.5a}$$

$$-\langle g|\mu|-\rangle e^{-i\omega_C t}.\varepsilon_{\pm}(t) = -\varepsilon_0 s(t)\mu_C e^{-2i\omega_C t}, \tag{C.5b}$$

where we have used the fact that $\mu_C = \frac{1}{\sqrt{2}}\langle g|\mu|x\rangle = \frac{1}{\sqrt{2}}\langle g|\mu|y\rangle$. Using the Rotating Wave Approximation (RWA) ($e^{\pm 2\omega} \approx 0$) we finally arrive to an expression for the wavefunction coefficients when an RCP pulse with frequency ω_C is applied,

$$\dot{\mathbf{C}}(t) = \frac{i}{\hbar}\varepsilon_0 s(t) \times \begin{pmatrix} |\mu_L|\cos(\theta-\omega_C t)C_e(t)e^{-i\omega_L t} + \mu_C C_+(t) \\ |\mu_L|\cos(\theta-\omega_C t)C_g(t)e^{i\omega_L t} \\ \mu_C C_g(t) \\ 0 \end{pmatrix}. \tag{C.6}$$

C.2 Derivation of the Wavefunction Coefficients when the *Circular* Molecule is Misaligned with the Axis of Light Propagation

In Section C.1 we derived the coefficients describing the evolution of the dimer wavefunction, when the xy plane of the molecule is aligned to be orthogonal to the z axis of propagation of the incident *circular* pulse. However, the above assumes a highly precise spectroscopical setup of the system that may not be achievable in practice. In fact, in a realistic system, one may have an ensemble of dimer configurations, where some conserve the desired geometry, and some deviate from the intended configuration. While the effect of deviations in the linear dimer is encoded in the angle θ (see Eq. 4.4), all our previous assumptions do not account for deviations in the *circular* pulse alignment with respect to the pulse.

For a highly-symmetric molecule, we are interested in the effect of deviations with respect to the plane orthogonal to the propagation of the light z. Rotations within this plane have no effect on the population of complex excitations. The symmetry $\mu_x = \mu_y$ allows one to arbitrarily choose the frame of reference of the molecule to one where the dipole components are aligned with the components of the light in that xy plane. Therefore, we account for the deviation of the plane with respect to the light propagation axis, z, by defining an angle ϕ, which quantifies the angle between the rotated transition dipole moment vector and its projection in the molecular plane. The components of the rotated vector, $\vec{\mu}'$, can be described in terms of the angle ϕ and the vector in the original plane, $\vec{\mu}$,

$$\vec{\mu}'_x = \vec{\mu}_x \cos\phi - \vec{\mu}_y \sin\phi \tag{C.7a}$$

$$\vec{\mu}'_y = \vec{\mu}_x \sin\phi + \vec{\mu}_y \cos\phi \tag{C.7b}$$

Given that the xy frame of reference on a D_{Nh} molecule can rotate with respect to the z axis, here $\vec{\mu}'_{x(y)}$ describes an arbitrary vector in the rotated molecular plane, such that the angle of rotation is minimum. Using the definition above for the transformed dipole moment of the *circular* molecule, we can evaluate the wavefunction for the *circular*-*linear* dimer excited through circular polarization, following Eq. C.1: $|\Psi(t)\rangle = C_g(t)|g\rangle e^{-iE_g t/\hbar} + C_e(t)|e\rangle e^{-iE_e t/\hbar} + C_x(t)|+\rangle e^{-iE_+ t/\hbar} + C_y(t)|-\rangle e^{-iE_- t/\hbar}$. Employing a similar process as that described in Sec. C.1, we can derive the matrix elements for the time-dependent wavefunction coefficients, when the dipole vector is rotated by ϕ. While the effect of the light perturbation on the *linear* molecule should not be affected by the orientation of the *circular* molecule, we update the electric field perturbation in the degenerate states $|\pm\rangle$ by employing the new definition for the dipole in Eq. C.5a,

$$\begin{aligned}\langle g|\mu|\pm\rangle e^{-i\omega_C t}.\varepsilon_\pm(t) &= \frac{1}{\sqrt{2}}\left(\langle g|\mu|x\rangle \pm i\langle g|\mu|y\rangle\right) e^{-i\omega_C t}.\varepsilon_\pm(t)\\ &= \frac{1}{\sqrt{2}}\left(\mu_{Cx}(\cos\phi \pm i\sin\phi) + i\mu_{Cy}(\pm\cos\phi + i\sin\phi)\right) e^{-i\omega_C t}.\varepsilon_\pm(t).\end{aligned} \tag{C.8}$$

Expanding the terms above, we can solve the matrix elements for the states $|+\rangle$ and

$|-\rangle$, after applying a RCP, ε_+,

$$\begin{aligned} -\langle g|\mu|+\rangle e^{-i\omega_C t}.\varepsilon_+(t) &= -\varepsilon_0 s(t)\mu_C e^{i\phi}[\cos(\omega_C t) + i\sin(\omega_C t)][\cos(\omega_C t) - i\sin(\omega_C t)] \\ &= -\varepsilon_0 s(t)\mu_C e^{i\phi}, \end{aligned} \tag{C.9a}$$

$$\begin{aligned} -\langle g|\mu|-\rangle e^{-i\omega_C t}.\varepsilon_+(t) &= -\varepsilon_0 s(t)\mu_C e^{-i\phi}[\cos(\omega_C t) - i\sin(\omega_C t)][\cos(\omega_C t) - i\sin(\omega_C t)] \\ &= -\varepsilon_0 s(t)\mu_C e^{-i\phi} e^{-2i\omega_C t} \approx 0. \end{aligned} \tag{C.9b}$$

Where we have used the RWA, such that $e^{-2i\omega_C t} \approx 0$. Replacing the above matrix elements in the righ-hand side of Eq. C.3, we can derive the time-dependent wavefunction coefficients for this system,

$$\dot{C}_j(t) = \frac{i}{\hbar}\varepsilon_0 s(t) \begin{pmatrix} |\mu_L|\cos(\theta - \omega_C t)C_e(t)e^{-i\omega_L t} + \mu_C e^{i\phi}C_+(t) \\ |\mu_L|\cos(\theta - \omega_C t)C_g(t)e^{i\omega_L t} \\ \mu_C e^{-i\phi}C_g(t) \\ 0 \end{pmatrix}. \tag{C.10}$$

Thus, the $\mathbf{C}\dot{(}t)$ coefficients are identical to those derived for the perfectly aligned system, with the rotation angle ϕ merely acting as a global phase in the evolution of the $|\pm\rangle$ wavefunction, $C_+(t)$.

Bibliography

[1] Victor Acosta and Philip Hemmer. “Nitrogen-vacancy centers: Physics and applications”. In: *MRS Bulletin* 38.2 (2013), pp. 127–130.

[2] Y. Aharonov and D. Bohm. “Significance of electromagnetic potentials in the quantum theory”. In: *Physical Review* 115.3 (Aug. 1959), pp. 485–491. ISSN: 0031899X.

[3] Marco Anderlini et al. “Controlled exchange interaction between pairs of neutral atoms in an optical lattice”. In: *Nature* 448.7152 (July 2007), pp. 452–456. ISSN: 0028-0836.

[4] John E Anthony. “The larger acenes: versatile organic semiconductors”. In: *Angewandte Chemie International Edition* 47.3 (2008), pp. 452–483.

[5] Alexander Aster et al. “Singlet Fission in a Flexible Bichromophore with Structural and Dynamic Control”. In: *Journal of the American Chemical Society* 143 (2021), pp. 2361–2371.

[6] Alexander Aster et al. “Tuning symmetry breaking charge separation in perylene bichromophores by conformational control”. In: *Chemical science* 10.45 (2019), pp. 10629–10639.

[7] Avogadro Chemistry. *Avogadro*. Version 1.2. June 15, 2016.

[8] German Barcenas et al. “First-principles studies of substituent effects on squaraine dyes”. In: *RSC Advances* 11.31 (2021), pp. 19029–19040.

[9] Christopher J Bardeen. “The structure and dynamics of molecular excitons”. In: *Annual review of physical chemistry* 65 (2014), pp. 127–148.

[10] Ingo Barth and Jörn Manz. “Electric ring currents in atomic orbitals and magnetic fields induced by short intense circularly polarized π laser pulses”. In: *Physical Review A - Atomic, Molecular, and Optical Physics* 75.1 (2007). ISSN: 10502947.

[11] Ingo Barth et al. “Unidirectional electronic ring current driven by a few cycle circularly polarized laser pulse: Quantum model simulations for Mg-porphyrin”. In: *Journal of the American Chemical Society* 128.21 (2006), pp. 7043–7049. ISSN: 00027863.

[12] Jon Louis Bentley. “Multidimensional binary search trees used for associative searching”. In: *Communications of the ACM* 18.9 (1975), pp. 509–517.

[13] Jeremy M Berg, John L Tymoczko, and Lubert Stryer. *Primary Structure: Amino Acids Are Linked by Peptide Bonds to Form Polypeptide Chains*. 5th. New York: W H Freeman, 2002.

[14] Eric R Bittner. "Frenkel exciton model of ultrafast excited state dynamics in AT DNA double helices". In: *Journal of Photochemistry and Photobiology A: Chemistry* 190.2-3 (2007), pp. 328–334.

[15] Karl Blum. *Density matrix theory and applications; 3rd ed.* Springer Series on Atomic Optical and Plasma Physics. Berlin: Springer, 2012.

[16] M. F. Borunda et al. "Aharonov-Casher and spin Hall effects in mesoscopic ring structures with strong spin-orbit interaction". In: *Physical Review B - Condensed Matter and Materials Physics* 78.24 (Dec. 2008), p. 245315. ISSN: 10980121.

[17] Étienne Boulais et al. "Programmed coherent coupling in a synthetic DNA-based excitonic circuit". In: *Nature Materials* 17 (2018), pp. 159–166.

[18] Jean Luc Brédas, Edward H. Sargent, and Gregory D. Scholes. "Photovoltaic concepts inspired by coherence effects in photosynthetic systems". In: *Nature Materials 2017 16:1* 16.1 (Dec. 2016), pp. 35–44. ISSN: 1476-4660.

[19] Heinz Peter Breuer and Francesco Petruccione. *The Theory of Open Quantum Systems*. Vol. 1. Oxford University Press, Nov. 2007, pp. 1–656. ISBN: 9780191706349.

[20] L. V. Butov. "Excitonic devices". In: *Superlattices and Microstructures* 108 (Aug. 2017), pp. 2–26. ISSN: 0749-6036.

[21] Brittany L Cannon et al. "Coherent exciton delocalization in a two-state DNA-templated dye aggregate system". In: *The Journal of Physical Chemistry A* 121.37 (2017), pp. 6905–6916.

[22] Jianshu Cao and Robert J. Silbey. "Optimization of exciton trapping in energy transfer processes". In: *Journal of Physical Chemistry A* 113.50 (Dec. 2009), pp. 13825–13838. ISSN: 10895639.

[23] Raanan Carmieli et al. "Excited State, Charge Transfer, and Spin Dynamics in DNA Hairpin Conjugates with Perylenediimide Hairpin Linkers". In: *The Journal of Physical Chemistry A* 113.16 (2009), pp. 4691–4700.

[24] D.A. Case et al. *AMBER 2018*. University of California, San Francisco, 2018.

[25] David A Case et al. *Amber 2021*. University of California, San Francisco, 2021.

[26] David A Case et al. "AmberTools". In: *Journal of Chemical Information and Modeling* 63 (2023), pp. 6183–6191.

[27] Maria A. Castellanos, Amro Dodin, and Adam P. Willard. "On the design of molecular excitonic circuits for quantum computing: The universal quantum gates". In: *Phys.Chem. Chem. Phys.* 22.5 (Feb. 2020), pp. 3048–3057. ISSN: 14639076.

[28] Maria A. Castellanos and Adam P. Willard. “Designing excitonic circuits for the Deutsch-Jozsa algorithm: mitigating fidelity loss by merging gate operations”. In: *Physical Chemistry Chemical Physics* 23.28 (July 2021), pp. 15196–15208. ISSN: 14639076.

[29] Carlos Ernesto Castro et al. “A primer to scaffolded DNA origami”. In: *Nature Materials* 8.3 (2011), p. 221.

[30] Jane C Chang. “Monopole effects on electronic excitation interactions between large molecules. I. Application to energy transfer in chlorophylls”. In: *J. Chem. Phys* 67 (1977), p. 3901.

[31] Xing-Yan Chen and Zhang-qi Yin. “Universal quantum gates between nitrogen-vacancy centers in a levitated nanodiamond”. In: *Phys. Rev. A* 99 (2 Feb. 2019), p. 022319.

[32] Aurélia Chenu and Gregory D. Scholes. “Coherence in energy transfer and photosynthesis”. In: *Annual Review of Physical Chemistry* 66 (Apr. 2015), pp. 69–96. ISSN: 15451593.

[33] Minhaeng Cho. *Two-dimensional optical spectroscopy.* CRC Press, 2009, p. 378. ISBN: 1420084305.

[34] Isaac L Chuang et al. “Experimental realization of a quantum algorithm”. In: *Nature* 393.6681 (1998), pp. 143–146.

[35] J. I. Cirac and P. Zoller. “Quantum Computations with Cold Trapped Ions”. In: *Phys. Rev. Lett.* 74 (20 May 1995), pp. 4091–4094.

[36] R. Cleve et al. “Quantum algorithms revisited”. In: *Proc. R. Soc. Lond. A* 454.1969 (Jan. 1998), pp. 339–354. ISSN: 1364-5021.

[37] Edward Collett. *Field guide to polarization.* Spie Bellingham, WA, 2005.

[38] Elisabetta Collini and Gregory D. Scholes. “Coherent intrachain energy migration in a conjugated polymer at room temperature”. In: *Science* 323.5912 (Jan. 2009), pp. 369–373. ISSN: 00368075.

[39] Rita E Cook et al. “Excimer formation and symmetry-breaking charge transfer in cofacial perylene dimers”. In: *The Journal of Physical Chemistry A* 121.8 (2017), pp. 1607–1615.

[40] Paul D Cunningham et al. “Förster Resonance Energy Transfer in Linear DNA Multifluorophore Photonic Wires: Comparing Dual versus Split Rail Building Block Designs (Advanced Optical Materials 21/2021)”. In: *Advanced Optical Materials* 9.21 (2021), p. 2170084.

[41] Paul D Cunningham et al. “Optical properties of vibronically coupled Cy3 dimers on DNA scaffolds”. In: *The Journal of Physical Chemistry B* 122.19 (2018), pp. 5020–5029.

[42] Ana Damjanović et al. “Excitons in a photosynthetic light-harvesting system: a combined molecular dynamics, quantum chemistry, and polaron model study”. In: *Physical Review E* 65.3 (2002), p. 031919.

[43] A S Davydov. "THE THEORY OF MOLECULAR EXCITONS". In: *Soviet Physics Uspekhi* 7.2 (Feb. 1964), pp. 145–178. ISSN: 0038-5670.

[44] D. Deutsch and R. Jozsa. "Rapid Solution of Problems by Quantum Computation". In: *Proc. R. Soc. Lond. A* 439.1907 (Dec. 1992), pp. 553–558. ISSN: 1364-5021.

[45] David Deutsch et al. "Quantum Privacy Amplification and the Security of Quantum Cryptography over Noisy Channels". In: *Phys. Rev. Lett.* 77 (13 Sept. 1996), pp. 2818–2821.

[46] Leonardo DiCarlo et al. "Demonstration of two-qubit algorithms with a superconducting quantum processor". In: *Nature* 460.7252 (2009), pp. 240–244.

[47] Christos D Dimitrakopoulos and Debra J Mascaro. "Organic thin-film transistors: A review of recent advances". In: *IBM Journal of research and development* 45.1 (2001), pp. 11–27.

[48] David P. DiVincenzo. "The Physical Implementation of Quantum Computation". In: *Fortschritte der Physik* 48.9-11 (2000), pp. 771–783.

[49] Shawn M. Douglas et al. "Rapid prototyping of 3D DNA-origami shapes with caDNAno". In: *Nucleic Acids Research* 37.15 (2009), pp. 5001–5006.

[50] Palash K Dutta et al. "DNA-directed artificial light-harvesting antenna". In: *Journal of the American Chemical Society* 133.31 (2011), pp. 11985–11993.

[51] "Electronic Delocalization, Vibrational Dynamics, and Energy Transfer in Organic Chromophores". In: *Journal of Physical Chemistry Letters* 8.13 (July 2017), pp. 3020–3031. ISSN: 19487185.

[52] Georg Engelhardt and Jianshu Cao. "Tuning the Aharonov-Bohm effect with dephasing in nonequilibrium transport". In: *Physical Review B* 99.7 (2019), pp. 1–12.

[53] Annemarie L. Exarhos et al. "Magnetic-field-dependent quantum emission in hexagonal boron nitride at room temperature". In: *Nature Communications* 10.1 (Dec. 2019), p. 222. ISSN: 2041-1723.

[54] Ardavan Farahvash et al. "Machine learning Frenkel Hamiltonian parameters to accelerate simulations of exciton dynamics". In: *J. Chem. Phys.* 153.7 (Aug. 2020), p. 074111. ISSN: 10897690.

[55] Richard P Feynman, Albert R Hibbs, and Daniel F Styer. *Quantum mechanics and path integrals*. Courier Corporation, 2010.

[56] Reinhold F. Fink et al. "Exciton Trapping in π-Conjugated Materials: A Quantum-Chemistry-Based Protocol Applied to Perylene Bisimide Dye Aggregates". In: *Journal of the American Chemical Society* 130.39 (2008), pp. 12858–12859.

[57] Fulvio Flamini, Nicolò Spagnolo, and Fabio Sciarrino. "Photonic quantum information processing: a review". In: *Reports on Progress in Physics* 82.1 (Jan. 2019), p. 016001. ISSN: 0034-4885.

[58] Stephen R Forrest. "The path to ubiquitous and low-cost organic electronic appliances on plastic". In: *nature* 428.6986 (2004), pp. 911–918.

[59] Th Förster. "Excimers". In: *Angewandte Chemie International Edition in English* 8.5 (1969), pp. 333–343.

[60] "Free energy calculations of watson-crick base pairing in aqueous solution". In: *Journal of the American Chemical Society* 121.41 (Oct. 1999), pp. 9503–9508. ISSN: 00027863.

[61] Jacov Frenkel. "On the transformation of light into heat in solids. I". In: *Physical Review* 37.1 (1931), p. 17.

[62] Nicolai Friis et al. "Observation of Entangled States of a Fully Controlled 20-Qubit System". In: *Physical Review X* 8.2 (Apr. 2018), p. 021012. ISSN: 2160-3308.

[63] A. Gaita-Ariño et al. "Molecular spins for quantum computation". In: *Nature Chemistry* 11.4 (Apr. 2019), pp. 301–309. ISSN: 1755-4330.

[64] Florian Garo and Robert Häner. "A DNA-based light-harvesting antenna". In: *Angewandte Chemie International Edition* 51.4 (2012), pp. 916–919.

[65] Neil Gershenfeld and Isaac L. Chuang. "Quantum Computing with Molecules". In: *Scientific American* 278.6 (June 1998), pp. 66–71. ISSN: 0036-8733.

[66] Jeffrey Gorman et al. "Deoxyribonucleic Acid Encoded and Size-Defined π-Stacking of Perylene Diimides". In: *Journal of the American Chemical Society* 144.1 (2022), pp. 368–376.

[67] Richard J. Gowers et al. "MDAnalysis: A Python Package for the Rapid Analysis of Molecular Dynamics Simulations". In: *Proceedings of the 15th Python in Science Conference.* 2016, pp. 98–105.

[68] Boris Grbić et al. "Aharonov–Bohm oscillations in p-type GaAs quantum rings". In: *Physica E: Low-dimensional Systems and Nanostructures* 40.5 (Mar. 2008), pp. 1273–1275. ISSN: 1386-9477. eprint: `0711.0489`.

[69] Alan Grossfield. *WHAM: The Weighted Histogram Analysis Method.* Version 2.0.11.

[70] Stephan Guide et al. "Implemention of the Deutsch-Jozsa algorithm on an ion-trap quantum computer". In: *Nature* 421.6918 (Jan. 2003), pp. 48–50. ISSN: 00280836.

[71] Stephanie M Hart et al. "Activating charge-transfer state formation in strongly-coupled dimers using DNA scaffolds". In: *Chemical Science* 13.44 (2022), pp. 13020–13031.

[72] Stephanie M Hart et al. "Engineering couplings for exciton transport using synthetic DNA scaffolds". In: *Chem* 7 (2021), pp. 752–773.

[73] Stephanie M Hart et al. "Identification of nonradiative decay pathways in Cy3". In: *The Journal of Physical Chemistry Letters* 11.13 (2020), pp. 5000–5007.

[74] Stephanie M Hart et al. "Tuning Optical Absorption and Emission Using Strongly Coupled Dimers in Programmable DNA Scaffolds". In: *The Journal of Physical Chemistry Letters* 13 (2022), pp. 1863–1871.

[75] Dugan Hayes, Graham B. Griffin, and Gregory S. Engel. "Engineering coherence among excited states in synthetic heterodimer systems". In: *Science* 340.6139 (June 2013), pp. 1431–1434. ISSN: 10959203.

[76] Elisa A. Hemmig et al. "Programming Light-Harvesting Efficiency Using DNA Origami". In: *Nano Lett.* 16.4 (Apr. 2016), pp. 2369–2374. ISSN: 15306992.

[77] Nicholas J Hestand and Frank C Spano. "Expanded theory of H-and J-molecular aggregates: the effects of vibronic coupling and intermolecular charge transfer". In: *Chemical reviews* 118.15 (2018), pp. 7069–7163.

[78] Nicholas J Hestand and Frank C Spano. "Interference between Coulombic and CT-mediated couplings in molecular aggregates: H-to J-aggregate transformation in perylene-based π-stacks". In: *The Journal of chemical physics* 143.24 (2015), p. 244707.

[79] Nicholas J Hestand et al. "Exciton mobility control through sub- A packing modifications in molecular crystals". In: *PHYSICAL REVIEW B* 91 (2015), p. 195315.

[80] Fan Hong et al. "DNA origami: scaffolds for creating higher order structures". In: *Chemical reviews* 117.20 (2017), pp. 12584–12640.

[81] Akihito Ishizaki et al. "Quantum coherence and its interplay with protein environments in photosynthetic electronic energy transfer". In: *Phys. Chem. Chem. Phys.* 12.27 (July 2010), pp. 7319–7337. ISSN: 14639076.

[82] Araz Jakalian, David B. Jack, and Christopher I. Bayly. "Fast, efficient generation of high-quality atomic charges. AM1-BCC model: II. Parameterization and validation". In: *Journal of computational chemistry* 23.16 (2002), pp. 1623–1641. ISSN: 0192-8651.

[83] Elizabeth A. Jares-Erijman and Thomas M. Jovin. "FRET imaging". In: *Nature Biotechnology 2003 21:11* 21.11 (Oct. 2003), pp. 1387–1395. ISSN: 1546-1696.

[84] Elizabeth A. Jares-Erijman and Thomas M. Jovin. "Imaging molecular interactions in living cells by FRET microscopy". In: *Current opinion in chemical biology* 10.5 (Oct. 2006), pp. 409–416. ISSN: 1367-5931.

[85] Ian T Jolliffe and Jorge Cadima. "Principal component analysis: a review and recent developments". In: *Philosophical transactions of the royal society A: Mathematical, Physical and Engineering Sciences* 374.2065 (2016), p. 20150202.

[86] Manabu Kanno et al. "Laser-polarization effects on coherent vibronic excitation of molecules with quasi-degenerate electronic states". In: *The Journal of Physical Chemistry A* 116.46 (2012), pp. 11260–11272.

[87] Michael Kasha. "Energy transfer mechanisms and the molecular exciton model for molecular aggregates". In: *Radiation research* 20.1 (1963), pp. 55–70.

[88] Michael Kasha, Henry R Rawls, and M Ashraf El-Bayoumi. “The exciton model in molecular spectroscopy”. In: *Pure and applied Chemistry* 11 (1965), pp. 371–392.

[89] Christina Kaufmann et al. “Discrete π-stacks of perylene bisimide dyes within folda-dimers: insight into long-and short-range exciton coupling”. In: *Journal of the American Chemical Society* 140.31 (2018), pp. 9986–9995.

[90] Phillip R Kaye, Raymond Laflamme, and Michele Mosca. *An introduction to Quantum Computing*. 1st. New York: Oxford University Press, 2007.

[91] Woojae Kim et al. “Solvent-modulated charge-transfer resonance enhancement in the excimer state of a bay-substituted perylene bisimide cyclophane”. In: *The journal of physical chemistry letters* 10.8 (2019), pp. 1919–1927.

[92] Trupti M Kodinariya, Prashant R Makwana, et al. “Review on determining number of Cluster in K-Means Clustering”. In: *International Journal* 1.6 (2013), pp. 90–95.

[93] Loni Kringle et al. “Temperature-dependent conformations of exciton-coupled Cy3 dimers in double-stranded DNA”. In: *The Journal of Chemical Physics* 148.8 (Feb. 2018), p. 085101. ISSN: 0021-9606.

[94] Shankar Kumar et al. “THE weighted histogram analysis method for free-energy calculations on biomolecules. I. The method”. In: *Journal of Computational Chemistry* 13.8 (1992), pp. 1011–1021. ISSN: 1096987X.

[95] J. A. Labastide et al. “Directional charge separation in isolated organic semiconductor crystalline nanowires”. In: *Nature Communications* 7.1 (Feb. 2016), pp. 1–7. ISSN: 20411723.

[96] T. D. Ladd et al. “Quantum computers”. In: *Nature* 464 (Mar. 2010), pp. 45–53.

[97] Aaron K. Le, Jon A. Bender, and Sean T. Roberts. “Slow Singlet Fission Observed in a Polycrystalline Perylenediimide Thin Film”. In: *Journal of Physical Chemistry Letters* 7.23 (2016), pp. 4922–4928.

[98] Chee Kong Lee, Liang Shi, and Adam P Willard. “Modeling the Influence of Correlated Molecular Disorder on the Dynamics of Excitons in Organic Molecular Semiconductors”. In: *The Journal of Physical Chemistry C* 123.1 (2019), pp. 306–314.

[99] Marcia Levitus and Suman Ranjit. “Cyanine dyes in biophysical research: the photophysics of polymethine fluorescent dyes in biomolecular environments”. In: *Quarterly reviews of biophysics* 44.1 (2011), pp. 123–151.

[100] Chenjian Lin et al. “Accelerating symmetry-breaking charge separation in a perylenediimide trimer through a vibronically coherent dimer intermediate”. In: *Nature Chemistry* (Apr. 2022). ISSN: 1755-4330.

[101] Daniel Loss and David P. DiVincenzo. “Quantum computation with quantum dots”. In: *Phys. Rev. A* 57 (1 Jan. 1998), pp. 120–126.

[102] James MacQueen et al. "Some methods for classification and analysis of multivariate observations". In: *Proceedings of the fifth Berkeley symposium on mathematical statistics and probability*. Vol. 1. 14. Oakland, CA, USA. 1967, pp. 281–297.

[103] Maria Ilaria Mallus et al. "Relation between Dephasing Time and Energy Gap Fluctuations in Biomolecular Systems". In: *J. Phys. Chem. Lett* 7 (2016).

[104] Divita Mathur et al. "Can a DNA origami structure constrain the position and orientation of an attached dye molecule?" In: *The Journal of Physical Chemistry C* (2020).

[105] Divita Mathur et al. "Understanding forster resonance energy transfer in the sheet regime with DNA brick-based dye networks". In: *ACS nano* 15.10 (2021), pp. 16452–16468.

[106] Wes McKinney et al. "Data structures for statistical computing in python". In: *Proceedings of the 9th Python in Science Conference*. Vol. 445. Austin, TX. 2010, pp. 51–56.

[107] Eion G McRae and Michael Kasha. "Enhancement of phosphorescence ability upon aggregation of dye molecules". In: *The Journal of Chemical Physics* 28.4 (1958), pp. 721–722.

[108] "MDAnalysis: A Python Package for the Rapid Analysis of Molecular Dynamics Simulations". In: *Proceedings of the 15th Python in Science Conference*. SciPy, 2016, pp. 98–105.

[109] Ian P Mercer, Ian R Gould, and David R Klug. "A quantum mechanical/molecular mechanical approach to relaxation dynamics: Calculation of the optical properties of solvated bacteriochlorophyll-a". In: *The Journal of Physical Chemistry B* 103.36 (1999), pp. 7720–7727.

[110] Naveen Michaud-Agrawal et al. "MDAnalysis: a toolkit for the analysis of molecular dynamics simulations". In: *Journal of computational chemistry* 32.10 (2011), pp. 2319–2327.

[111] Oleksandr V. Mikhnenko, Paul W.M. Blom, and Thuc Quyen Nguyen. "Exciton diffusion in organic semiconductors". In: *Energy and Environmental Science* 8.7 (2015), pp. 1867–1888. ISSN: 17545706.

[112] C. Monroe et al. "Programmable quantum simulations of spin systems with trapped ions". In: *Rev. Mod. Phys.* 93 (2 Apr. 2021), p. 025001.

[113] Andrés Montoya-Castillo, Timothy C Berkelbach, and David R Reichman. "Extending the applicability of Redfield theories into highly non-Markovian regimes". In: *J. Chem. Phys.* 143 (2015), p. 194108.

[114] Shaul Mukamel. *Principles of Nonlinear Optical Spectroscopy*. New York: Oxford University Press, 1995, p. 543. ISBN: 0195092783.

[115] Bálint Náfrádi et al. "Room temperature manipulation of long lifetime spins in metallic-like carbon nanospheres". In: *Nature Communications* 7.1 (Nov. 2016), p. 12232. ISSN: 2041-1723.

[116] Michael A Nielsen and Isaac L Chuang. *Quantum Computation and Quantum Information: 10th Anniversary Edition.* Cambridge; New York: Cambridge University Press, Jan. 2011.

[117] Jeremy L O'Brien. "Optical quantum computing." In: *Science (New York, N.Y.)* 318.5856 (Dec. 2007), pp. 1567–70. ISSN: 1095-9203.

[118] Carsten Olbrich and Ulrich Kleinekathöfer. "Time-dependent atomistic view on the electronic relaxation in light-harvesting system II". In: *J. Phys. Chem. B* 114.38 (2010), pp. 12427–12437. ISSN: 15205207.

[119] Carsten Olbrich et al. "From atomistic modeling to excitation transfer and two-dimensional spectra of the FMO light-harvesting complex". In: *The Journal of Physical Chemistry B* 115.26 (2011), pp. 8609–8621.

[120] Carsten Olbrich et al. "Theory and Simulation of the Environmental Effects on FMO Electronic Transitions". In: *J. Phys. Chem. Lett* 2 (2011), pp. 1771–1776.

[121] Jonathan Olson et al. "Quantum information and computation for chemistry". In: *arXiv preprint arXiv:1706.05413* (2017).

[122] Oksana Ostroverkhova. *Organic Optoelectronic Materials: Mechanisms and Applications.* Nov. 2016.

[123] Karl Pearson. "LIII. On lines and planes of closest fit to systems of points in space". In: *The London, Edinburgh, and Dublin philosophical magazine and journal of science* 2.11 (1901), pp. 559–572.

[124] Andrew H. Proppe et al. "Bioinspiration in light harvesting and catalysis". In: *Nature Reviews Materials* 5 (2020), pp. 828–846.

[125] E. Romero, V.I. Novoderezhkin, and R. van Grondelle. "Quantum design of photosynthesis for bio-inspired solar-energy conversion". In: *Nature* 543 (2017), pp. 355–365.

[126] Benoıt Roux. "The calculation of the potential of mean force using computer simulations". In: *Computer Physics Communications* 91.1 (Sept. 1995), pp. 275–282.

[127] Palas Roy et al. "Ultrafast Excimer Formation and Solvent Controlled Symmetry Breaking Charge Separation in the Excitonically Coupled Subphthalocyanine Dimer". In: *Angewandte Chemie International Edition* 60.19 (2021), pp. 10568–10572.

[128] Ville Satopaa et al. "Finding a" kneedle" in a haystack: Detecting knee points in system behavior". In: *2011 31st international conference on distributed computing systems workshops.* IEEE. 2011, pp. 166–171.

[129] Gregory D Scholes. "Long-range resonance energy transfer in molecular systems". In: *Annual review of physical chemistry* 54.1 (2003), pp. 57–87.

[130] Gregory D Scholes et al. "Lessons from nature about solar light harvesting". In: *Nature Chemistry* 3.10 (2011), p. 763.

[131] LLC Schrödinger. “The PyMOL Molecular Graphics System, Version 1.8”. Nov. 2015.

[132] Ebin Sebastian and Mahesh Hariharan. “Null Exciton-Coupled Chromophoric Dimer Exhibits Symmetry-Breaking Charge Separation”. In: *Journal of the American Chemical Society* 143 (2021), pp. 13769–13781.

[133] Yihan Shao et al. “Advances in molecular quantum chemistry contained in the Q-Chem 4 program package”. In: *Molecular Physics* 113.2 (2015), pp. 184–215.

[134] Liang Shi and Adam P Willard. “Modeling the effects of molecular disorder on the properties of Frenkel excitons in organic molecular semiconductors”. In: *The Journal of Chemical Physics* 149.9 (2018), p. 94110.

[135] Sangwoo Shim et al. “Atomistic study of the long-lived quantum coherences in the Fenna-Matthews-Olson complex”. In: *Biophysical journal* 102.3 (2012), pp. 649–660.

[136] Robert Silbey and Robert A Harris. “Variational calculation of the dynamics of a two level system interacting with a bath”. In: *The Journal of chemical physics* 80.6 (1984), pp. 2615–2617.

[137] Stephanie Simmons, Hua Wu, and John J.L. Morton. “Controlling and exploiting phases in multi-spin systems using electron spin resonance and nuclear magnetic resonance”. In: *Philosophical Transactions of the Royal Society A: Mathematical, Physical and Engineering Sciences* 370.1976 (Oct. 2012), pp. 4794–4809. ISSN: 1364503X.

[138] Ho-Jin Son et al. “Light-harvesting and ultrafast energy migration in porphyrin-based metal–organic frameworks”. In: *Journal of the American Chemical Society* 135.2 (2013), pp. 862–869.

[139] Frank C. Spano. “EXCITONS IN CONJUGATED OLIGOMER AGGREGATES, FILMS, AND CRYSTALS”. In: *Annual Review of Physical Chemistry* 57.1 (May 2006), pp. 217–243. ISSN: 0066-426X.

[140] Sivaramapanicker Sreejith et al. “Squaraine dyes: a mine of molecular materials”. In: *Journal of Materials Chemistry* 18.3 (2008), pp. 264–274.

[141] Qiming Sun et al. “PySCF: the Python-based simulations of chemistry framework”. In: *WIREs Computational Molecular Science* 8.1 (2018), e1340.

[142] Edward F. Valeev et al. “Effect of Electronic Polarization on Charge-Transport Parameters in Molecular Organic Semiconductors”. In: *Journal of the American Chemical Society* 128.30 (Aug. 2006), pp. 9882–9886.

[143] Stéphanie Valleau, Alexander Eisfeld, and Alán Aspuru-Guzik. “On the alternatives for bath correlators and spectral densities from mixed quantum-classical simulations”. In: *The Journal of Chemical Physics* 137.22 (2012).

[144] Franck AP Vendeix, Antonio M Munoz, and Paul F Agris. “Free energy calculation of modified base-pair formation in explicit solvent: A predictive model”. In: *RNA* 15.12 (2009), pp. 2278–2287.

[145] Pauli Virtanen et al. “SciPy 1.0: Fundamental Algorithms for Scientific Computing in Python”. In: *Nature Methods* 17 (2020), pp. 261–272.

[146] Eike-Christian Wamhoff et al. “Programming structured DNA assemblies to probe biophysical processes”. In: *Annual Review of Biophysics* 48 (2019), pp. 395–419.

[147] Hui Wang et al. “Insights into the excitonic processes in polymeric photocatalysts”. In: *Chem. Sci.* 8.5 (2017), pp. 4087–4092.

[148] Junmei Wang et al. “Automatic atom type and bond type perception in molecular mechanical calculations”. In: *Journal of Molecular Graphics and Modelling* 25.2 (2006), pp. 247–260. ISSN: 1093-3263.

[149] Junmei Wang et al. “Development and testing of a general Amber force field”. In: *Journal of Computational Chemistry* 25.9 (2004), pp. 1157–1174. ISSN: 01928651.

[150] G Wendin. “Quantum information processing with superconducting circuits: a review”. In: *Reports on Progress in Physics* 80.10 (Oct. 2017), p. 106001. ISSN: 0034-4885.

[151] Jianlan Wu et al. “Efficient energy transfer in light-harvesting systems: Quantum-classical comparison, flux network, and robustness analysis”. In: *Journal of Chemical Physics* 137.17 (Nov. 2012), p. 174111. ISSN: 00219606. eprint: `1109.5769`.

[152] H Yamagata et al. “HJ-Aggregate Behavior of Crystalline 7,8,15,16-Tetraazaterrylene: Introducing a New Design Paradigm for Organic Materials”. In: *J. Phys. Chem. C* 118 (2014), pp. 28842–28854.

[153] H Yamagata et al. “The nature of singlet excitons in oligoacene molecular crystals”. In: *J. Chem. Phys.* 134.20 (2011), p. 204703. ISSN: 00219606.

[154] Pei Yun Yang and Jianshu Cao. “Steady-State Analysis of Light-Harvesting Energy Transfer Driven by Incoherent Light: From Dimers to Networks”. In: *Journal of Physical Chemistry Letters* 11.17 (Sept. 2020), pp. 7204–7211. ISSN: 19487185. eprint: `2007.10825`.

[155] Ryan M Young and Michael R Wasielewski. “Mixed electronic states in molecular dimers: Connecting singlet fission, excimer formation, and symmetry-breaking charge transfer”. In: *Accounts of Chemical Research* 53 (2020), pp. 1957–1968.

[156] Joel Yuen-Zhou et al. “Topologically protected excitons in porphyrin thin films”. In: *Nature materials* 13.11 (2014), pp. 1026–1032.